Seismic isolation of buildings for vertical earthquake excitations

A thesis

submitted in fulfilment

of the requirements for the degree

of

Doctor of Philosophy in Engineering

at

The University of Waikato

by

Fatemeh (Elena) Eskandary-Malayery

THE UNIVERSITY OF
WAIKATO
Te Whare Wānanga o Waikato

2022

Abstract

This thesis concerns a seismic isolation mechanism for vertical component of earthquake. The vertical component of earthquake can be stronger and more destructive than the horizontal component in near-fault areas, for instance, Christchurch earthquake in New Zealand in 2011 or Bam earthquake in Iran in 2003. Therefore, this needs to be considered in designing and retrofitting structures to reduce damage to buildings and human lives. This thesis develops a numerical and experimental model of the seismic isolation based on quasi-zero-stiffness-system (QZSS) and high-static-low-dynamic-stiffness-system (HSLDSS) concepts. The results suggest the HSLDSS considered could be a practical solution for decreasing the response of the system to the vertical component of earthquake.

Analytical and numerical models of a HSLDSS and a QZSS are developed. The behaviour of the mechanism subjected to static loading as well as time harmonic excitation is investigated. The harmonic balance method and the direct numerical integration method are employed to solve the equations of motion for the system. In addition, the effect of each design parameter is studied when the structure is subjected to static and harmonic excitation loadings. The impact of uncertainties in the payload as well as mistuning in the system are addressed. It is seen that the QZSS is very sensitive to any changes in payload or mistuning, while HSLDSS is unaffected by slight changes to load or initial geometry. In addition, the effects of linear and nonlinear friction elements in the model are investigated. It is seen that friction decreases the performance of the system and needs to be minimised. The response of the HSLDSS mechanism subjected to 23 near-fault earthquake ground motions is presented and discussed. Moreover, the mechanism design variables (initial geometry, static loading, stiffness of the springs) which minimise the peak acceleration, RMS response, and peak displacement are investigated. The behaviour of the linear, QZSS and HSLDSS are compared to show which case is more efficient. Although QZSS is the most effective, it is sensitive to any changes in the payload and mistuning. On the other hand, HSLDSS is less sensitive to those changes while retaining good performance and reducing the peak and RMS acceleration significantly.

The experimental results are presented, the measurements taken compared to the numerical results and show good agreement. The results show significant reduction in peak and RMS acceleration for most input signals. However, for Chichi earthquake, the reverse is true. This is explained by the frequency content of the signal which has high power in the frequency range below 1 Hz. The friction force is estimated from three techniques: measurement from static tests, measurement from harmonic excitation and from the least squared error between numerical and experimental results. Among these three, the last method is found to give good agreement between numerical and experimental results for all earthquake inputs.

The developed mechanism is shown to be efficient in isolating structures with one support subjected to earthquake inputs. It reduces the force transmission from the base to structures during earthquakes.

Acknowledgements

I would like to thank the following people who have helped me undertake this research:

My supervisors, Prof. Sinniah Ilanko, Prof. Brian Mace (Department of Mechanical Engineering, University of Auckland), and Dr Yusuke Mochida, for their consistent guidance and feedback throughout this project.

The financial support provided by the Ministry of Business and Innovation and Employment (New Zealand) through the Smart Ideas scheme (Project No: UOWX1801, 'Omnidirectional earthquake isolation system') is gratefully acknowledged.

Dr. Kēpa Morgan (Pou Hautū, Mahi Maioro Professionals Ltd) and Alan Park (CEO, Robinson Seismic Ltd.) for their suggestions regarding the experimental model.

Francesco Pellicano (Department of Engineering Enzo Ferrari, University of Modena and Reggio Emilia, Italy) for verifying preliminary results through their software.

Sarath Pathirana (Technologist, Dynamics and Control Laboratory, University of Auckland) for his technical assistance, equipment setting up training and detailed design of a modified rig.

Thanks also to my partner, Marc Chaigneau, for his patience and encouragement.

And to my mother, who set me off on the road to this PhD a long time ago.

Table of Contents

List of Figures

List of Tables

Nomenclature

l	Length of inclined bars
m	Mass of the system
k_h	Horizontal spring stiffness
$k_{h,QZS}$	Horizontal spring stiffness of QZSS
k_v	Vertical spring stiffness
k_e	Equivalent stiffness of mechanism
$\hat{k}_e$	Dimensionless equivalent stiffness of mechanism
$\hat{k}_{e\_QZS}$	Dimensionless equivalent stiffness of mechanism of QZSS
λ	Horizontal/vertical spring stiffness ratio
λ_{QZS}	Horizontal/vertical spring stiffness ratio of QZSS
β	HSLDSS/QZSS horizontal spring stiffness ratio
c	Viscous damping coefficient
ξ	Damping ratio
ω	Excitation frequency
ω_n	Natural frequency of a linear system
ω_{n_QZS}	Frequency of the mechanism
Ω	ω/ω_n frequency ratio
U	Dimensionless base excitation amplitude
θ	Angle of the inclined bars with horizontal axis
θ_0	Angle of the inclined bars with horizontal axis in unloaded position
θ_s	Angle of the inclined bars with horizontal axis in static equilibrium position
F	Force applied on the mass
$\hat{F}$	Dimensionless force applied on the mass
F_i	Force in inclined bars
F_v	Force in the vertical spring
F_h	Force in the horizontal springs
$\hat{F}_h$	Dimensionless force in the horizontal springs
b	Horizontal projected length of each arm
b_0	Horizontal projected length of each arm in unloaded position

x	Vertical upward displacement of mass from the unloaded initial state
x_s	Static displacement of mass at the equilibrium position
X	Vertical upward displacement of mass from the static equilibrium position
$\hat{X}$	Dimensionless vertical upward displacement of mass from the static equilibrium position
y	Vertical absolute displacement of mass with respect to the base from the unloaded initial state
Y	Vertical absolute displacement of mass with respect to the base from the static equilibrium position
Y'	Vertical relative displacement of mass with respect to the base from the static equilibrium position
$\hat{Y}'$	Dimensionless vertical relative displacement of mass with respect to the base from the static equilibrium position
z	Displacement of the base excitation
Z	Dimensionless displacement of the base excitation
f_{dv}	Maximum friction force in vertical direction
f_{dh}	Maximum friction force in horizontal direction
v_d	Velocity tolerances
η_v	f_{dv}/mg ratio
η_h	f_{dh}/mg ratio
f_{tr}	Maximum nondimensional force amplification
CE	Cumulative energy

Chapter 1.

Introduction

1.1 Overview

Some parts of the world are prone to earthquakes, which can cause death or injury and destruction of buildings and other infrastructure. Although the horizontal component of earthquakes is larger in some areas, in other places, especially near faults, the vertical motion plays a significant role in causing the collapse of structures. For instance, the Bam earthquake of 26 December 2003 (Moment Magnitude (Mw) of 6.5) occurred in the city of Bam in the southeast of Iran [1]. That earthquake demolished the city of Bam. The greatest vertical acceleration of this earthquake was 1.1 times gravity, which is considered as a severe vertical acceleration, and caused a disaster in this city of 100,000 population. The number of victims was declared officially to be more than 26,000 and more than 30,000 people were injured. Moreover, a historical monument of Arg-e-Bam, which was over 2000 years old, was mostly destroyed by this earthquake. Another example is the Christchurch earthquake with moment magnitude of 6.2, which struck on 22 February 2011 in Christchurch (New Zealand's second largest city with a population of 377,000) [2]. The impact of the Christchurch earthquake, with a high vertical ground acceleration of 0.8 times gravity in the city centre (and 2.2 times gravity in the epicentre, Heathcote valley station), was massive for this city, among which there were 181 fatalities and the collapse of some central city buildings including office buildings and iconic heritage structures. Total repairs have been estimated to have cost NZ$15-20 billion, making the Christchurch earthquake the most expensive in New Zealand's history.

In 1991, Niazi and Bozorgnia showed that the ratio of 2/3 for vertical-to-horizontal peak acceleration ratio V/H for designing structures is not safe in near-fault areas [3]. This ratio is generally higher in near-field than far-field, higher in low period than in high period range and higher on soil rather than on rock base [4]. In the short-period part of the spectrum (less than 0.2 sec), the vertical response may exceed the horizontal one as well (V/H ratio is presented as 1.5 and 0.9 for a distance shorter than 3 km and 20 km, respectively). Therefore, the vertical component of an earthquake in a near-fault location is equally or more important than the horizontal component. For higher periods (more than 3s), however, the V/H ratio is usually around 0.5 or less which does not need to be considered in earthquake the design of an earthquake-resisting building. Papazoglou & Elnashai [5] indicated that a V/H ratio which exceeds 1.7 causes damage to structural elements. Based on evidences, the damage was due to the increase in axial compression forces in the columns and shear walls. In addition, fluctuation in the forces led to flexural or shear failures in those members. Moreover, the vertical component of the earthquake can cause damage to non-structural elements as well [6; 7]. According to New Zealand Standard 1170.5 [8], the structures located at the distance less than 20 km from a major fault, should be designed for the vertical component of earthquake as well as the horizontal component.

Therefore, retrofitting buildings and designing new structures for isolation from both horizontal and vertical components of earthquakes is necessary in near-fault areas to improve building safety and reduce the risk to people's lives. Numerous studies have been conducted to introduce different devices to control horizontal vibrations of earthquake either passively or actively. Although there have been only a few studies that address protection against vertical excitation,

this topic has become of more interest in recent years. In this chapter, mitigation solutions introduced by other researchers for horizontal and vertical vibration as well as earthquake excitations are reviewed.

To address the shortcomings of the available methods, in this thesis, an isolation mechanism based on the use of negative geometric stiffness is proposed to isolate structures from vertical component of earthquakes. This study contains theoretical and experimental results and discusses the influence of various design parameters on isolation performance.

In the next chapter, analytical and numerical models of the proposed isolator will be presented, and results will be discussed.

1.2 Vibration mitigation systems

Almost all structures are exposed to different types of vibration in their lifetime. There are many sources of structural vibration, for instance, human activities or natural sources such as earthquake and wind. While in most cases vibrations may cause inconvenience for inhabitants or users, in some situations vibrations can lead to the collapse of structures. Therefore, in order to mitigate unexpected deterioration and raise the safety of structures, different systems can be adopted. There are three methods introduced to control vibrations in structures: passive, active, and hybrid (active-passive, and semi-active). Structural vibration control includes multiple principles [9]. The first principle is that an auxiliary oscillator system can be added to absorb vibrational energy transferred from the main structure in order to reduce the motion of the main structure. For instance, a passive-tuned mass damper or an active mass damper driver (AMD) system is an auxiliary oscillator system which is an active control method. The second principle is to decrease the energy transmitted from the input excitation into the structure. For example, base-isolation is a passive control system which reduces the energy flow transferred to structures. The third principle is to provide additional damping for the main structure. Oil damper systems, for example, follow this principle using either passive or semi-active control. The fourth principle is to prevent buildings from resonance subjected to input excitations. For instance, base-isolated buildings as well as variable-stiffness system with semi-active control increase the natural period of the system up to around 3-4s which avoids resonance due to earthquake excitations. The fifth principle, which is only implemented in active-controlled systems, is to produce computer-controllable forces for the main structure.

For protecting structures from deterioration due to vibration as well as earthquake ground motions, four control techniques have been used: active [10], passive [11-13], hybrid [2] and semi-active [14].

1.2.1 Passive control systems

Passive control is a method of controlling vibration and dissipating vibrational energy without requiring external power [15]. There are three main devices which have been used as passive control systems in structures: dampers, absorbers, and isolators.

- Dampers

A damper is a device which dissipates the vibrational energy of a structure. The damping device uses the energy of excitation and turns it into other types of energy thereby reducing the energy available to cause potential damage. There are at least four types of dampers: (1) friction dampers, (2) viscous dampers, (3) yielding dampers, and (4) magnetorheological dampers (MR

dampers) [16]. The first three types are passive and the last damper, MR damper, can be either a passive or semi-active control system. Friction dampers dissipate energy by rubbing two surfaces on each other (using dry friction or Coulomb friction). This is considered an efficient, practical and economic type of damper without any need for maintenance. Mualla and Belev investigated the seismic performance of a friction damper in a single frame numerically and experimentally [17]. The results showed that this damper significantly reduces the response displacement as well as the base shear. Viscous dampers consist of a steel cylinder containing silicon oil and a piston and do not need any maintenance during their lifetime [16]. This type of damper changes the vibration energy into pushing fluid through an orifice. Moreover, it is able to dissipate the energy, and reduce the acceleration and deformation due to vibrations. In a study, the effect of internal stiffness of a viscous damper was investigated for a full-scale stay cable application experimentally and analytically [18]. The results illustrated that the internal stiffness of the viscous damper should be minimal in order to get the maximum damping. Another type of damper is yielding dampers which are made up of a metal and dissipate energy by plastic non-linear behaviour [16]. Although the system is ductile, the initial stiffness and its bearing capacity are high. This damper is mostly used as a fuse in metal bracing in structures. In a study, aluminium shear yielding dampers had the effect of an energy dissipating device [19]. This study was carried out on a one-storey industrial building subjected to seismic excitation. The analytical and experimental results showed 36-82% reduction in the maximum base shear force, and it reduced the roof acceleration and displacement significantly.

- Absorbers

Absorbers are secondary oscillators which are attached to a body or structure to protect it by absorbing the kinetic energy due to excitation; therefore, they vibrate instead of the main structure, while the main structure remains more or less stationary. Tuned mass dampers (TMD), tuned liquid dampers (TLD), and tuned liquid column dampers (TLCD) are three common absorbers. The function of these three absorbers were investigated in an experimental study which showed that they perform well [20]. As an example, multiple tuned mass dampers have been designed using a formal optimization methodology for structures with 3D irregularities [21]. This method would reduce the structural and non-structural damage due to severe excitation. An eight-story irregular building was used as an example in this research and the location of the required TMDs was investigated. Another article introduced tuned liquid damper (TLD) for a single-degree-of-freedom structure [22]. TLD is a kind of passive damper which can absorb vibrations by using the sloshing motion of the liquid inside a container. The sloshing motion of the liquid is nonlinear and complex. This research was conducted to tune the natural frequency of the sloshing motion to the natural frequency of the structure in order to absorb vibrational energy. The TLD damper can be constructed relatively simply. In addition, it needs low maintenance and is practical for retrofitting structures. This system was only investigated for horizontal vibration excitation. Some other absorbers have also been introduced to prevent structures from vibrating [23]. For instance, shape memory alloy wires have been implemented in buildings as a real-time tuned vibration absorber which is an adaptive passive control system. The stiffness of this beam-like absorber is changed by changing the temperature. Moreover, a synthetic shunt impedance has been employed in order to change the characteristics of the absorber to adjust its frequency to the excitation frequency and increase the performance [24]. Analytical and experimental research was done as well as a comparison of the performance of the proposed system to a non-adaptive undamped system. Hirunyapruk et al [25] used a magneto-rheological fluid as the core of a beam-like vibration absorber to make the stiffness tuneable. This concept is helpful for the case in which the

excitation frequency is time harmonic, and the frequency varies with time. In this mechanism, the shear stiffness of the absorber changes while the magnetic field changes.

- Isolators

Isolation bearings are widely used passive control systems which isolate structures from seismic ground motions. In order to limit force transmission, the structure can be retrofitted by a base-isolator [26]. In this situation, the structure can be isolated from the vibration coming from the base. Isolators are effective at frequencies greater than $\sqrt{2k/m}$ (where k and m are the stiffness and the mass of the structure, respectively). It was shown that if the stiffness decreases, the isolation would be effective over a wider range of frequencies.

There are three general types of base isolations: frictional/sliding bearings and elastomeric bearing. Resilient-friction base isolation (R-FBI) is an example of a sliding bearing, which was investigated by some researchers [27-29]. This type of bearing works based on a friction between a Teflon and a stainless-steel surface, which resists small horizontal loads but slides under large loads. There is a hard rubber cylindrical core, which carrying the horizontal and vertical loads on the foundation. The friction pendulum system (FPS) is another example for the sliding isolation system [30; 31]. This isolator performs based on articulated slider on spherical concave chrome surface in which the friction coefficient plays a significant role. As an example of the Elastomeric bearing, lead-rubber bearing (LRB) is one of the most popular and frequently used of this type [32]. There are many publications addressing the application of LRBs in different buildings and bridges [33; 34]. This type of bearing consists of two steel plates on the top and the bottom and several elastomer layers in the middle to provide lateral flexibility and isolation. There is a lead core which dissipates energy by yielding. There are some steel shims inside the elastomeric part to provide the vertical stiffness and load bearing capacity.

The main problem of purely passive controlled building isolation for seismic applications is that the performance depends on the input excitation [35]. In other words, if a passive system is optimised for an earthquake input, defined after another historical earthquake with different characteristics, it may perform poorly. There are also some other limitations and problems related to passive control systems [36]. For example, the rubber in lead-rubber-bearing base-isolators is susceptible to ageing and loss of durability. Those passive systems based on fluid viscosity need regular maintenance. For those systems based on steel yielding or lead extrusion, also, there are some complexities regarding the installation and replacement of parts after strong earthquakes. Moreover, polymer-based systems, for instance, perform differently in different temperatures. Therefore, active-control can be an option for mitigating building vibration for a wider range of earthquake inputs without the mentioned limitations.

Another practical vibration isolator is the vibration barrier (ViBa) [37]. This isolator which was introduced by Cacciola & Tombari [38], is a buried structure which works based on structure-soil-structure interaction (SSSI). The study showed that the greater the soil density and consequent interaction between structure and soil, the more effective the ViBa would become. However, in a less dense soil, isolation decreases, and the resonance can be observed at the natural frequencies of the structure. It was also shown that for a soil stiffness of 200 N/m, the energy dissipation became maximised. The experimental study resulted in a considerable reduction of 87% in the acceleration of a structure due to harmonic ground motion. Moreover, the hypothesis of this research includes linear soil behaviour and single-dimensional ground motion which could cause unrealistic results. There are some other papers addressing ViBa

isolator and developing this method for different situations theoretically and experimentally [2; 14; 26]. This method has so far only been considered for horizontal ground excitations.

1.2.2 Active and semi-active control systems

Active control is a technology that relies on sensors, actuators and computer control, and needs a significant amount of power to control structures subjected to excitation [39]. The real-time-measured data are employed in the process so this system can reduce the structural response drastically. The seismic-response-control philosophy of active control was first introduced by Kobori in 1956 [40]. This system was then designed and validated for the Kyobashi Seiwa Building in Tokyo, Japan in 1989 by Kobori et al. [41; 42]. Moreover, Yao published a practical scheme of active control in earthquake engineering in 1972 which inspired many researchers in this area [43].

There are various active control strategies, which are used to mitigate the response of structures subjected to lateral forces such as wind and earthquake. For instance, Yan et al. designed an optimum active TMD for a high-rise building subjected to wind loads [44]. In another study, active tendon systems were suggested for cable-stayed bridges subjected to wind loads [45]. Active coupled building systems are also another active control strategy which has been proposed by a number of researchers [46; 47]. In this method, by using actuators and connecting two or multiple buildings together, the response of a structure is controlled. This technique is usually used for coupling two buildings with different height and stiffness to reduce the response of structures subjected to earthquake excitation. By adding more actuators, the effect can be magnified.

Because of economic reasons, active-controlled systems are usually used in high-rise buildings and luxury hotels and would be too expensive in short buildings. Since active control systems require considerable power resources, in the case of a power failure, there will be no protection against wind or earthquake loads. Semi-active control, however, requires less power and mostly operates using batteries.

Semi-active control is also a kind of hybrid control that needs much less power than active control to work. It needs power only for some of the stages. Therefore, this system has an appropriate efficiency and effectiveness using less power. As mentioned previously, the MR damper can be an active or semi-active controllable fluid device [48]. This damper consists of iron particles in oil, which can align themselves subjected magnetic fields. As a result, the viscosity of the fluid changes depending on the magnetic field. If the magnetic field is constant, it behaves like a linear fluid passive control system, while, if the magnetic field varies, the viscosity and stiffness change and the system behaves as semi-active control. This semi-active control MR damper dissipates energy subjected to electromagnetic forces [16]. Xu et al. proposed a modified sigmoid model to estimate the behaviour of MR dampers, and provided a detailed design of an optimum MR dampers for seismic applications [49]. Experimental results showed good agreement with the numerical results which proves the accuracy of this model. Another study investigated the use of MR dampers for semi-active controlling base-isolated structures [50]. Experiments and analysis showed that this damper reduces both relative displacements and absolute acceleration of a base-isolated building effectively. A study was conducted to find a semi-active damping coefficient by solving the nonlinear inhomogeneous - constrained optimal control problem to decrease the displacement of the structure in unisolated modes [51].

Although single passive, active, or semi-active control systems have limited applications in the structures subjected to vibrations, hybrid systems, which involve a combination of any of those systems, are a more practical solution for a smart structure technology and improve the performance of a structure subjected to vibrations [52; 53].

1.2.3 Hybrid control systems

Hybrid control is an alternative system to a single passive or active control systems in structures and can alleviate the limitations of these two systems and protect the structure better [53]. There is less required power for active control in this system as it has a higher efficiency [54]. In addition, unlike pure passive control, it is not limited to low-rise buildings, and can minimise the possibility of uplift arising from severe horizontal excitations. Most of the time, base isolators are combined with other devices such as dampers to decrease the displacement of the main structure. There are various types of hybrid systems such as a combination of an active mass driver (AMD) and passive dampers [55]. Madden et al. also considered adding an adaptive fluid damper to a 2D sliding base-isolated frame to reduce displacement of a building subjected to earthquake excitations [56].

1.3 Mitigation of the vertical component of earthquake excitation

1.3.1 Overview

Most of the successful seismic mitigation systems in use are for horizontal seismic excitation, and there is no practical/commercial solution for vertical component of earthquake excitations in near-fault areas. In the last few years, researchers have tried to address the importance of vertical excitation and develop mitigation solutions. For instance, Furukawa et al. have done experimental research on a four-storey building on a base-isolator to investigate the performance of base-isolators for the vertical component of earthquakes [57]. They showed that if the vertical acceleration exceeds $2g$ in the building, damage would be detrimental as the vertical acceleration is amplified in the higher storeys. Some of the papers focus on three dimensional (3D) seismic isolation. For example, Liu et al. investigated a 3D isolator for a four-storey building subjected to seismic ground motions [58]. In this technique, there are lead-rubber bearings used beneath the building to isolate it from horizontal ground motion. For the vertical isolation, however, some simple linear springs and viscous dampers are employed as isolation components. This research compared the experimental and analytical model (in SAP2000 software) of an isolated structure with a non-isolated structure. Although they studied several earthquakes and carried out theoretical and experimental studies, the isolation was not completely satisfactory. This is thought to be because the stiffness which is used for the vertical isolator is constant, whereas tuneable stiffness would be ideal to isolate buildings over a broader frequency range.

Vu et al. proposed a vertical distributed flexibility and damping strategy (VDF) for base-isolated buildings [59]. In this method, column bearings are installed to columns in order to reduce the vertical seismic motions in higher levels rather than in the base. There are many aspects which should be addressed about this strategy in the future. For instance, the details of the column bearings should be investigated. Moreover, the relative displacement between the floors and the large lateral deformation may cause damages to non-structural components which need further study.

In another paper, a vertical seismic base-isolation system with a variable stiffness using hydraulic cylinders was proposed for long-span spatial structures [60]. Taking advantage of validated numerical models and experiments, it was shown that, although complicated, this mechanism performed similarly to a traditional 3D linear spring isolator and the complications in the system did not improve the performance.

A numerical investigation conducted by Barbieri et al. employed semi-active control strategies in a two-story building on a variable stiffness mechanism for vertical seismic isolation [61]. This does not depend on applying dynamic forces to oppose to the earthquake forces. Instead, isolation was achieved by changing the stiffness of the supports to half its static state value, when either the acceleration of the excitation or the velocity of the base exceeds a specific value. The results showed that transmissibility of acceleration could be reduced by using an isolator with such stiffness variation. However, this was a specific case study and would rely on having an active control system to change the stiffness.

1.3.2 Quasi-zero stiffness isolators

The idea of quasi-zero-stiffness (QZS) dates back to 1989 [62]. Having high static and low dynamic stiffness (HSLDS), this nonlinear mechanism can be designed to have a low resonance frequency. This idea gained popularity in recent decades as researchers employed this idea in various areas, such as in space research to simulate zero gravity [63] as well as in mechanical engineering to isolate vehicle seats from vibrations caused by road profiles [64]. There have been a variety of researches utilizing negative stiffness (NS) elements to create a HSLDSS or QZSS. For instance, Carrella et al. added two inclined springs to a linear mass-spring system to achieve QZSS and investigated its static behaviour using a Taylor Series extension [65]. Zheng et al. used a magnetic element to add NS to a system to create a QZS isolator [66]. In this study, the dynamic behaviour of the mechanism subjected to harmonic excitation was evaluated analytically and experimentally. In another study, Liu et al. added two horizontal buckled Euler beams to obtain a QZSS [67]. Le and Ahn proposed another QZSS with two inclined arms and horizonal springs for isolating vehicle seats from vibrations [64]. The design parameters for the mechanism, shown in Figure 1.1 (a), was investigated theoretically and experimentally. Figure 1.1 (b) shows the dimensionless force versus dimensionless displacement graphs in which $\gamma_1$is configurative parameters of the proposed system ($\gamma_1 = \frac{a}{L_0}$).

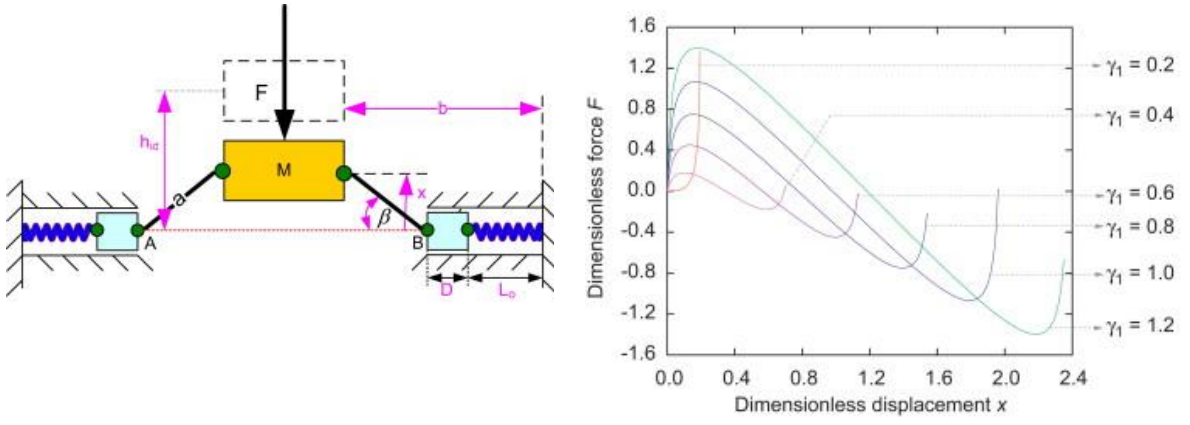

(a) (b)

Figure 1.1.(a) Negative stiffness mechanism, (b) Force- displacement graphs [64].

As it can be seen, the horizontal springs add negative stiffness to the system which are the main elements to make a QZSS. This is explained comprehensively in chapter 2. The results showed

that this can isolate the mass from excitations over a wide range of frequencies. After that, more experimental investigations were conducted for a NS structure subjected to low frequency vibrations (i.e. ≤ 5 Hz) [68]. Moreover, Le and Nguyen suggested adjusting the parameters of a QZSS in order to keep the performance high and isolation for any changes in the self-weight of the mechanism [69]. In another paper, an optimization was carried out for four negative stiffness systems for a vehicle seat suspension [70]. For this purpose, the bearing capacity of the mechanism has to be compromised with the low stiffness to get the maximum vibration isolation. In another study, the benefit of active control strategies in QZS mechanism was investigated [71-73].

Zhang et al investigated the effect of inertia of the inclined arms, friction and nonlinear damping in a QZSS [74]. The results showed that in order to avoid the impact of inertia on the performance, the mass of the arms should not be more than 10^{-3} times the total mass on the isolator. Friction and nonlinear damping, however, do not have significant effects at higher frequencies.

Since a QZS isolator system has been proven to be an effective adaptive passive control system, it has been becoming more popular amongst earthquake engineers for seismic applications in the last decade. This is because by reducing the natural frequency of the system to lower than 0.5 Hz, isolation of the vertical acceleration with high frequency content (e.g. > 1 Hz) can be improved. Mochida et al also investigated the use of negative stiffness in reducing the transmission of forces in structures and suggested its use for seismic isolation [75]. However, it was limited to static analysis and they did not conduct any dynamic analysis. Asai proposed a QZSS within a variable ellipse curve mechanism to reduce the acceleration response at the structure and proved the efficiency with a prototype experiment [76]. Bouna et al. proposed a QZSS adopting two inclined springs to add NS for the piers of multi-span bridge to isolate the vibration and compared this system with a linear viscoelastic isolator [77]. A parameter study was carried out to investigate the effect of each design variable such as spring stiffness and damping on the isolation performance. The dynamic behaviour of this mechanism was only evaluated using sinusoidal input not earthquake excitation. Najafijozani et al. investigated 3D adaptive seismic isolator mechanisms for nuclear powerplant equipment [78]. In this study, six adaptive vertical isolators with linear and nonlinear spring and damping were compared. The results showed that the system with a nonlinear spring (with hardening behaviour) and linear damping decreases the peak response acceleration more than other cases. In addition, the linear or nonlinear damping did not significantly affect the results. Liu et al proposed a QZS isolator consisting of two inclined bars and horizontal springs to add NS and a vertical damper to reduce vertical ground motion in near-fault earthquakes [79]. Although the results show that the QZSS effectively reduces the response of a mass subjected to near-fault excitations, details of the design parameters need to be quantified, which requires further study. Besides, changes in the payload, the effect of rocking etc. were not addressed in this research. Zhou et al. proposed another configuration of a QZSS for vertical seismic isolation [80]. In this study, two inclined springs added NS to the system. The experimental results were provided for this system, however, there was no verification with an analytical modelling. They also investigated the efficiency of the isolator through experiments and compared the results with numerical analysis. In another paper, Zhou et al. proposed a QZSS consisting of a spring disc to add NS and a vertical spring to support the payload for vertical seismic isolation. [81] In this research the performance of this isolator was investigated numerically and analytically for a seven-storey building. Although the results are promising, the feasibility of this system in practice needs further investigation. Also, the detailed design and the combination of horizontal and

vertical vibration need to be studied. Two years after that, Zhou et al. developed a 3D base-isolator system including the same QZSS configuration (for vertical and rotational isolation) and a friction pendulum system (for isolation in the horizontal direction) for a 20-storey building subjected to earthquake excitations and metro vibration [82]. The numerical results, which were generated by OpenSees software, showed that the isolator reduces base shear significantly, however, the overturning may cause a large displacement and drift in higher floors. This research was just limited to two earthquake inputs (Chi-chi and El Centro) and did not consider uncertainties in the design (e.g. any changes in payload or mistuning). In addition, a friction element is not considered in the modelling which is not realistic. In another research, the mentioned QZSS (with disc spring) was combined with an LRB to isolate a large-aspect-ratio facility from vertical and horizontal components of earthquakes [83]. The numerical results show that the performance of the isolator varies for different earthquake excitations and input amplitude. Generally, those earthquakes with high period content are disadvantaged from the isolation. This research did not consider the effect of friction or any uncertainties in the modelling. The feasibility and the detailed design of this isolator also required further investigation.

The studies on vertical isolators to date do not consider theoretical and experimental investigation into the QZSS or the HSLDSS isolators performance under seismic loading and the effect of friction and uncertainties on their static and dynamic behaviour. The purpose of this study is to address this gap in literature

1.4 Research questions

The general objectives of this research are to investigate the applicability of a QZSS or a HSLDSS for earthquake isolation of structures.

The overall question is how to minimise transfer of damaging forces to the structure. Considering the variation in loads on civil engineering structures, and the uncertainties associated with construction, the performance of an isolator need to be clearly understood in terms of parameters associated with geometry and load change. This leads to the following research questions:

- How to minimize vertical force transmission?
- How does the mechanism behave subjected to vertical excitations considering the uncertainties?
- How to optimize the design parameters of the isolator after taking into account the answers to the first two questions?

1.5 Thesis outline

This thesis consists of six chapters including introduction and conclusion.

In Chapter 2, the analytical and numerical models of a HSLDSS are developed. The behaviour of the mechanism subjected to static loading as well as time harmonic excitation is investigated. Harmonic balance method and direct integration method are employed to solve the equations of motion for the system. In addition, the effect of each design parameter is studied when the structure is subjected to static and harmonic excitation loadings. The impact of uncertainties in

the payload as well as mistuning in the system are addressed. At the end of this chapter, the effects of linear and nonlinear friction element in the model are investigated.

In Chapter 3, the response of the HSLDSS mechanism subjected to 23 near-fault earthquake ground motions is presented and discussed. Moreover, the mechanism design variables are optimised for these input signals in order to minimise the peak acceleration, RMS response, and peak displacement. The behaviour of the linear, QZSS, and other HSLDSS are compared together to show which case is more efficient.

In Chapter 4, the rig and equipment which were used in the experiments are described. In addition, the tests conducted and the measurements taken are explained.

In Chapter 5, experimental results from static, time harmonic and earthquake tests are presented. These results are compared to the numerical ones and discussion is provided. In this Chapter, the friction force is measured from three techniques and the results are presented.

In Chapter 6, a comprehensive conclusion is provided regarding the results and discussions in the previous chapters.

1.6 References

[1] Zare, M., & Hamzehloo, H. (2004). A study of the strong ground motions of 26 December 2003 Bam earthquake: Mw6.5. *Journal of Seismology and Earthquake Engineering, 5*(4), 33-56.

[2] Cacciola, P., Espinosa, M. G., & Tombari, A. (2015). Vibration control of piled-structures through structure-soil-structure-interaction. *Soil Dynamics and Earthquake Engineering, 77*, 47-57.

[3] Niazi, M., & Bozorgnia, Y. (1991). Behavior of near-source peak horizontal and vertical ground motions over smart-1 array, Taiwan. *Bulletin of the Seismological Society of America, 81*(3), 715.

[4] Bozorgnia, Y., & Campbell, K. W. (2016). Ground motion model for the vertical-to-horizontal (V/H) ratios of PGA, PGV, and response spectra. *Earthquake Spectra, 32*(2), 951-978.

[5] Papazoglou, A. J., & Elnashai, A. S. (1996). Analytical and field evidence of the damaging effect of vertical earthquake ground motion. *Earthquake Engineering & Structural Dynamics, 25*(10), 1109-1137.

[6] Pujols, J. C. G., & Ryan, K. L. (2020). Slab vibration and horizontal-vertical coupling in the seismic response of low-rise irregular base-isolated and conventional buildings. *Journal of Earthquake Engineering, 24*(1), 1-36.

[7] Pujols, J. C. G., & Ryan, K. L. (2018). Computational simulation of slab vibration and horizontal-vertical coupling in a full-scale test bed subjected to 3D shaking at E-Defense. *Earthquake Engineering & Structural Dynamics, 47*(2), 438-459.

[8] NZS 1170.5:2004, *Structural design actions – Part 5: Earthquake actions standard, Amendment 1.*

[9] Nishitani, A., & Inoue, Y. (2001). Overview of the application of active/semiactive control to building structures in Japan. *Earthquake Engineering & Structural Dynamics, 30*(11), 1565-1574.

[10] Cha, Y.-J., & Agrawal, A. K. (2017). Seismic retrofit of mrf buildings using decentralized semi-active control for multi-target performances. *Earthquake Engineering & Structural Dynamics, 46*(3), 409-424.

[11] Chang, C.-M., Shia, S., & Lai, Y.-A. (2018). Seismic design of passive tuned mass damper parameters using active control algorithm. *Journal of Sound and Vibration, 426*, 150-165.

[12] Eljajeh, Y., & Petkovski, M. (2018). Self-adaptive approach for optimisation of passive control systems for seismic resistant buildings. *Bulletin of Earthquake Engineering, 16*(7), 3171-3194.

[13] Wu, Q., Dai, J., & Zhu, H. (2018). Optimum design of passive control devices for reducing the seismic response of twin-tower-connected structures. *Journal of Earthquake Engineering, 22*(5), 826-860.

[14] Tombari, A., Zentner, I., & Cacciola, P. (2016). Sensitivity of the stochastic response of structures coupled with vibrating barriers. *Probabilistic Engineering Mechanics, 44*, 183-193.
[15] Franchek, M. A., Ryan, M. W., & Bernhard, R. J. (1996). Adaptive passive vibration control. *Journal of Sound and Vibration, 189*(5), 565-585.
[16] Chandnani, D., Joshi, R., & Trivedi, K. (2016). Characteristics & applications of different types of dampers as seismic energy dissipater. *International Journal of Computer Science and Network, 5*(2).
[17] Mualla, I. H., & Belev, B. (2002). Performance of steel frames with a new friction damper device under earthquake excitation. *Engineering Structures, 24*(3), 365-371.
[18] Zhou, H., Sun, L., & Xing, F. (2014). Damping of full-scale stay cable with viscous damper: Experiment and analysis. *Advances In Structural Engineering, 17*(2), 265-274.
[19] Sachan, A., & Rai, D. C. (2012). *Aluminium shear yielding damper (AL-SYD) as an energy dissipation device in truss moment frames (TMFS)*. Presented at the 15th World Conference on Earthquake Engineering.
[20] Bigdeli, Y., & Kim, D. (2016). Damping effects of the passive control devices on structural vibration control: TMD, TLC and TLCD for varying total masses. *Journal of Civil Engineering, 20*(1), 301-308.
[21] Daniel, Y., & Lavan, O. (2014). Gradient based optimal seismic retrofitting of 3D irregular buildings using multiple tuned mass dampers. *Computers & Structures, 139*, 84-97.
[22] Marivani, M., & Hamed, M. S. (2009). Numerical simulation of structure response outfitted with a tuned liquid damper. *Computers & Structures, 87*(17), 1154.
[23] Rustighi, E., Brennan, M. J., & Mace, B. R. (2003). *Design of an adaptive vibration absorber using shape memory alloy*. Southampton: University of Southampton, Institute of Sound and Vibration Research.
[24] McDaid, A. J., & Mace, B. R. (2013). A self-tuning electromagnetic vibration absorber with adaptive shunt electronics. *Smart Materials and Structures, 22*(10), 105013.
[25] Hirunyapruk, C., Brennan, M. J., Mace, B. R., & Li, W. H. (2010). A tunable magneto-rheological fluid-filled beam-like vibration absorber. *Smart Materials and Structures, 19*(5).
[26] Swain, A., & Ghosh, P. (2016). Experimental study on dynamic interference effect of two closely spaced machine foundations. *Canadian Geotechnical Journal, 53*(2), 196-209.
[27] Su, L., Ahmadi, G., & Tadjbakhsh, I. G. (1991). Performance of sliding resilientfriction baseisolation system. *Journal of Structural Engineering, 117*(1), 165-181.
[28] Mostaghel, N., & Khodaverdian, M. (1987). Dynamics of resilient-friction base isolator (R-FBI). *Earthquake Engineering & Structural Dynamics, 15*(3), 379-390.
[29] Clark, P. W., & James, M. K. (1990). *Experimental testing of the resilient-friction base isolation system*. Berkeley: Earthquake Engineering Research Center, University of California.
[30] Zayas, V. A., Low, S. S., & Mahin, S. A. (1990). A simple pendulum technique for achieving seismic isolation. *Earthquake Spectra, 6*(2), 317-333.
[31] Calvi, G. M., Calvi, P. M., & Moratti, M. (2017). Seismic isolation of buildings using devices based on sliding between surfaces with variable friction coefficient. *Innovative Infrastructure Solutions, 2*(1), 1-18.
[32] Kelly, J. M., & Hodder, S. B. (1982). Experimental study of lead and elastomeric dampers for base isolation systems in laminated Neoprene bearings. *Bulletin of the New Zealand Society for Earthquake Engineering, 15*(2), 53-67.
[33] Shoaei, P., & Mahsuli, M. (2019). Reliability-based design of steel moment frame structures isolated by lead-rubber bearing systems. *Structures Structures, 20*, 765-778.
[34] Hameed, A., Koo, M.-S., Do, T. D., & Jeong, J.-H. (2008). Effect of lead rubber bearing characteristics on the response of seismic-isolated bridges. *Journal of Civil Engineering, 12*(3), 187-196.
[35] Calise, A. J., I., C. J., J., G. B., & C., H. C. (1996). Hybrid passive/active control performance in buildings using robust control design approaches. *IFAC Proceedings Volumes, 29*(1), 5547-5552.
[36] Dolce, M., Cardone, D., & Marnetto, R. (2000). Implementation and testing of passive control devices based on shape memory alloys. *Earthquake Engineering & Structural Dynamics, 29*, 945-968.

[37] Tombari, A., Zentner, I., & Cacciola, P. (2014). *Sensitivity of the stochastic response of structures protected by the vibrating barrier control device*. from http://eprints.brighton.ac.uk/15418/1/CSM7-Tombari_Zentner_Cacciola-converis.pdf.
[38] Cacciola, P., & Tombari, A. (2015). Vibrating barrier: a novel device for the passive control of structures under ground motion. *Proceedings of the Royal Society A: Mathematical, Physical and Engineering Science, 471*(2179), 20150075.
[39] Preumont, A., & Seto, K. (2008). *Active control of structures*. Chichester, U.K.: John Wiley.
[40] Kobori, T. (1956). Quake resistant and nonlinear problems of the structural vibrations to violent earthquake. *Journal of Kyoto University Disaster Prevention Laborator*, 116 – 124.
[41] Kobori, T., Koshika, N., Yamada, K., & Ikeda, Y. (1991). Seismic-response-controlled structure with active mass driver system. Part 2: Verification. *Earthquake Engineering & Structural Dynamics, 20*(2), 151-166.
[42] Kobori, T., Koshika, N., Yamada, K., & Ikeda, Y. (1991). Seismic-response-controlled structure with active mass driver system. Part 1: Design. *Earthquake Engineering & Structural Dynamics, 20*(2), 133-149.
[43] Yao, J. T. P. (1972). Concept of structural control. *Journal of Structural Division, ASCE, 98*(7), 1567–1574.
[44] Yan, N., Wang, C. M., & Balendra, T. (1999). Optimal damper characteristics of ATMD for buildings under wind loads. *Journal of Structural Engineering, 125*(12), 1376-1383.
[45] Bossens, F., & Preumont, A. (2001). Active tendon control of cable-stayed bridges: a large scale demonstration. *Earthquake Engineering & Structural Dynamics, 30*, 961-980.
[46] Christenson, R. E., Spencer, B. F., Hori, N., & Seto, K. (2003). Coupled building control using acceleration feedback. *Computer Aided Civil and Infrastructure Engineering, 18*(1), 4-18.
[47] Ying, Z. G., Ni, Y. Q., & Ko, J. M. (2003). Stochastic optimal coupling-control of adjacent building structures. *Computers and Structures, 81*(30-31), 2775-2787.
[48] Bagherkhani, A., & Baghlani, A. (2021). Reliability assessment of MR fluid dampers in passive and semi-active seismic control of structures. *Probabilistic Engineering Mechanics, 63*.
[49] Xu, Z.-D., Sha, L.-F., Zhang, X.-C., & Ye, H.-H. (2013). Design, performance test and analysis on magnetorheological damper for earthquake mitigation numerical and experimental study on magnetorheological dampers. *Structural Control and Health Monitoring, 20*(6), 956-970.
[50] Oliveira, F., Botto, M. A., Morais, P., & Suleman, A. (2018). Semi-active structural vibration control of base-isolated buildings using magnetorheological dampers. *Journal of Low Frequency Noise, Vibration and Active Control, 37*(3), 565-576.
[51] Vu, D. C., Politopoulos, I., & Diop, S. (2018). A new semi-active control based on nonlinear inhomogeneous optimal control for mixed base isolation. *Structural Control and Health Monitoring, 25*(1).
[52] Fisco, N. R., & Adeli, H. (2011). Smart structures: Part I: Active and semi-active control. *Scientia Iranica, 18*(3 A), 275-284.
[53] Fisco, N. R., & Adeli, H. (2011). Smart structures: Part II: Hybrid control systems and control strategies. *Scientia Iranica, 18*(3), 285-295.
[54] Mohammadi, S., Hatam, S., & Khodayari, A. (2015). Modeling of a hybrid semi-active/passive vibration control technique. *Journal of Vibration and Control, 21*(1), 21-28.
[55] Lu, L. Y., Lin, G. L., & Lin, C. H. (2009). A unified analysis model for energy dissipation devices used in seismic-resistant structures. *Computer-Aided Civil and Infrastructure Engineering*(1), 41-61.
[56] Madden, G. J., Wongprasert, N., & Symans, M. D. (2003). Analytical and numerical study of a smart sliding base isolation system for seismic protection of buildings. *Computer-Aided Civil and Infrastructure Engineering, 18*(1), 19-30.
[57] Furukawa, S., Sato, E., Shi, Y., Becker, T., & Nakashima, M. (2013). Full-scale shaking table test of a base-isolated medical facility subjected to vertical motions. *Earthquake Engineering & Structural Dynamics, 42*(13), 1931-1949.
[58] Liu, W., Tian, K., Wei, L., He, W., & Yang, Q. (2018). Earthquake response and isolation effect analysis for separation type three-dimensional isolated structure. *Bulletin of Earthquake Engineering, 16*(12), 6335-6364.
[59] Vu, B., Unal, M., Warn, G. P., & Memari, A. M. (2014). A distributed flexibility and damping strategy to control vertical accelerations in base-isolated buildings distributed flexibility and damping strategy. *Structural Control and Health Monitoring, 21*(4), 503-521.

[60] Chen, Z., Ding, Y., Shi, Y., & Li, Z. (2019). A vertical isolation device with variable stiffness for long-span spatial structures. *Soil Dynamics and Earthquake Engineering, 123*, 543-558.
[61] Barbieri, M., Pellicano, F., & Ilanko, S. (2018). Active vibration control of seismic excitation. *Nonlinear Dynamics, 93*(1), 41-52.
[62] Alabuzhev, P., Gritchin, A., & Kim, L. (1989). *Vibration protecting and measuring systems with quasi-zero stiffness*. New York: Hemisphere.
[63] Denoyer, K., & Johnson, C. (2001). *Recent achievements in vibration isolation systems for space launch and on-orbit applications*. Presented at the 52nd International Astronautical Congress.
[64] Le, T. D., & Ahn, K. K. (2011). A vibration isolation system in low frequency excitation region using negative stiffness structure for vehicle seat. *Journal of Sound and Vibration, 330*(26), 6311-6335.
[65] Carrella, A., Brennan, M. J., & Waters, T. P. (2007). Static analysis of a passive vibration isolator with quasi-zero-stiffness characteristic. *Journal of Sound and Vibration, 301*(3-5), 678-689.
[66] Zheng, Y., Zhang, X., Luo, Y., Yan, B., & Ma, C. (2016). Design and experiment of a high-static-low-dynamic stiffness isolator using a negative stiffness magnetic spring. *Journal of Sound and Vibration, 360*, 31-52.
[67] Liu, X., Huang, X., & Hua, H. (2013). On the characteristics of a quasi-zero stiffness isolator using Euler buckled beam as negative stiffness corrector. *Journal of Sound and Vibration, 332*(14), 3359-3376.
[68] Le, T. D., & Ahn, K. K. (2013). Experimental investigation of a vibration isolation system using negative stiffness structure. *International Journal of Mechanical Sciences, 70*, 99-112.
[69] Le, T. D., & Nguyen, V. A. D. (2017). Low frequency vibration isolator with adjustable configurative parameter. *International Journal of Mechanical Sciences, 134*, 224-233.
[70] Papaioannou, G., Voutsinas, A., & Koulocheris, D. (2020). Optimal design of passenger vehicle seat with the use of negative stiffness elements. *Proceedings of the Institution of Mechanical Engineers, Part D: Journal of Automobile Engineering, 234*(2-3), 610-629.
[71] Sun, X., Xu, J., Jing, X., & Cheng, L. (2014). Beneficial performance of a quasi-zero-stiffness vibration isolator with time-delayed active control. *International Journal of Mechanical Sciences, 82*, 32-40.
[72] Yong, W., Shunming, L., Chun, C., & Xingxing, J. (2015). Dynamic analysis of a high-static-low-dynamic-stiffness vibration isolator with time-delayed feedback control. *Shock and Vibration, 2015*.
[73] Wang, Y., Li, S., Cheng, C., & Su, Y. (2018). Adaptive control of a vehicle-seat-human coupled model using quasi-zero-stiffness vibration isolator as seat suspension. *Journal of Mechanical Science and Technology, 32*(7), 2973-2985.
[74] Zhang, X., Cao, Q., & Huang, W. (2021). Dynamic characteristics analysis for a quasi-zero-stiffness system coupled with mechanical disturbance. *Archive of Applied Mechanics, 91*(4), 1449-1467.
[75] Mochida, Y., Kida, N., & Ilanko, S. (2015). Base isolator of vertical seismic vibration using a negative stiffness mechanism. In *Vibration Engineering and Technology of Machinery* (pp. 1113-1119).
[76] Asai, T. A., Yoshikazu; Kimura, Kosuke; Masui, Takeshi. (2017). Adjustable vertical vibration isolator with a variable ellipse curve mechanism. *Earthquake Engineering & Structural Dynamics*.
[77] Bouna, H. S., Nbendjo, B. R. N., & Woafo, P. (2020). Isolation performance of a quasi-zero stiffness isolator in vibration isolation of a multi-span continuous beam bridge under pier base vibrating excitation. *Nonlinear Dynamics, 100*(2), 1125-1141.
[78] Najafijozani, M., Becker, T. C., & Konstantinidis, D. (2020). Evaluating adaptive vertical seismic isolation for equipment in nuclear power plants. *Nuclear Engineering and Design, 358*.
[79] Liu, D., Liu, Y., Sheng, D., & Liao, W. (2018). Seismic response analysis of an isolated structure with QZS under near-fault vertical earthquakes. *Shock and Vibration, 2018*(3), 9149721-9149721.
[80] Zhu, G., Liu, J., Cao, Q., Cheng, Y., Lu, Z., & Zhu, Z. (2020). A two degree of freedom stable quasi-zero stiffness prototype and its applications in aseismic engineering. *Science China Technological Sciences, 63*, 496–505.

[81] Zhou, Y., Chen, P., & Mosqueda, G. (2019). Analytical and numerical investigation of quasi-zero stiffness vertical isolation system. *Journal of Engineering Mechanics, 145*(6), 04019035.
[82] Zhou, Y., Chen, P., & Mosqueda, G. (2021). Numerical studies of three-dimensional isolated structures with vertical quasi-zero stiffness property. *Journal of Earthquake Engineering*, 1-22.
[83] Zhou, Y., & Chen, P. (2019). Numerical simulation of a new 3D isolation system designed for a facility with large aspect ratio. *Computer Modeling in Engineering and Sciences, 120*(3), 759-777.

Chapter 2.

Analytical and Numerical Models for Harmonic Excitation

2.1 Introduction

As mentioned in the previous chapter, isolation from the vertical component of an earthquake would be an advantage for buildings located in near-fault areas. To be able to develop a mechanism with high-static-low-dynamic stiffness to satisfy the needs, the static and dynamic behaviours must be fully understood. In this chapter, relevant equations are derived for this mechanism under both static and time harmonic dynamic loadings. These equations are solved analytically (if possible) or numerically using MATLAB software. Moreover, the effect of each of the design parameters is studied to find the range of ideal parameters. In the last part, dry friction is also introduced into the model and the effect of this on the system behaviour using numerical analysis is explored.

In the next chapter, the behaviour of the mechanism will be investigated under earthquake excitation.

2.2 Model description

The single-degree of freedom (SDoF) system representation of the mechanism is shown in Figure 2.1, which is the same as the proposed model in the paper by Le & Ahn [1]. The aim is to isolate the mass (m) from base motion. This system comprises two rigid, massless arms (inclined bars in the figure) with length l. The angle between arms and the horizontal direction is θ. One end of each arm is supported by a horizontal spring (stiffness k_h) and the other end is connected to the mass. The mass is also supported by a vertical spring (stiffness k_v) which is parallel to a viscous damper (c). One end of each spring is connected to the base. The two horizontal springs remain horizontal at all time. The arms are assumed to be able to rotate freely in relation to the mass and the horizontal springs.

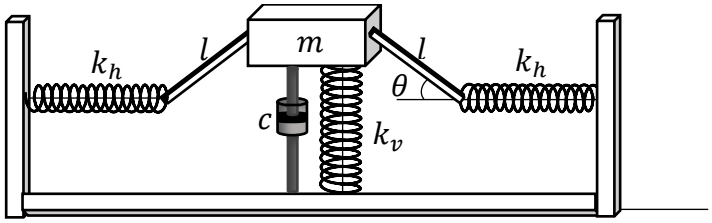

Figure 2.1. View of the SDoF model of the system with the isolator mechanism [1].

There are two main differences between the equations in this research and the literature. First, the equations in this research are based on more tangible parameters with physical expressions whereas in the literature, the parameters are mostly ratios of different dimensions. Second, the equations of motion in this research are developed from the unloaded position as an origin, while in the literature the origin of the equations is the static equilibrium position with arms in horizontal position ($\theta = 0$). Considering the unloaded position as an origin allows to study the system at different equilibrium positions and investigate the effects of mistuning which is not possible with the equation in the literature. A QZSS is generally designed to have equivalent stiffness of zero at the static equilibrium position ($\theta = 0$). The vertical spring has a positive stiffness and the horizontal springs add negative stiffness to the system if they are in

compression when $\theta = 0$. Therefore, in the equilibrium position, the arms are horizontal and they add the maximum negative stiffness to the system and the equivalent stiffness of the system becomes zero while retaining the stability, but is at a critical state. It is important to note that the stiffness of the horizontal spring cannot be larger than this value or else the system becomes unstable at $\theta = 0$.

2.3 Static behaviour of the mechanism

To find the static stiffness of the system, consider a force F which is applied at point A along the vertical upward direction (x) as shown in Figure 2.2. For any given force F the internal force in the inclined bars, horizontal springs and the vertical spring are F_i, F_h, and F_v, respectively. The origin of the vertical coordinate x ($x = 0$) is set at the unloaded state of point A, which is the position of the point A before applying the static loading. It is, also, assumed that both horizontal and vertical springs are unstretched in this position (Figure 2.3 (a)). The initial value of θ is θ_0. Considering $b = l\cos\theta$ is the horizontal projected length of each arm and $b_0 = l\cos\theta_0$ is the initial value of b when $\theta = \theta_0$. Figure 2.3 (b) shows the mechanism in the static equilibrium position, when F is due to the weight and the arms are designed to be horizontal. θ_s is the angle of the arms with horizontal axis at the static equilibrium position, which in this case equals to 0°.

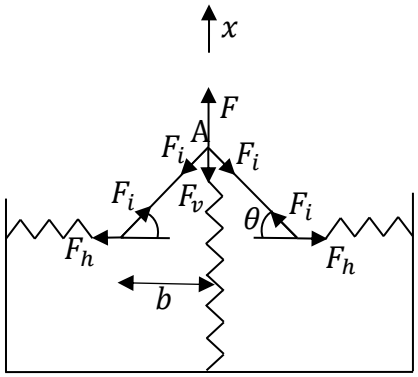

Figure 2.2. Force diagram of the SDoF system and the isolator mechanism

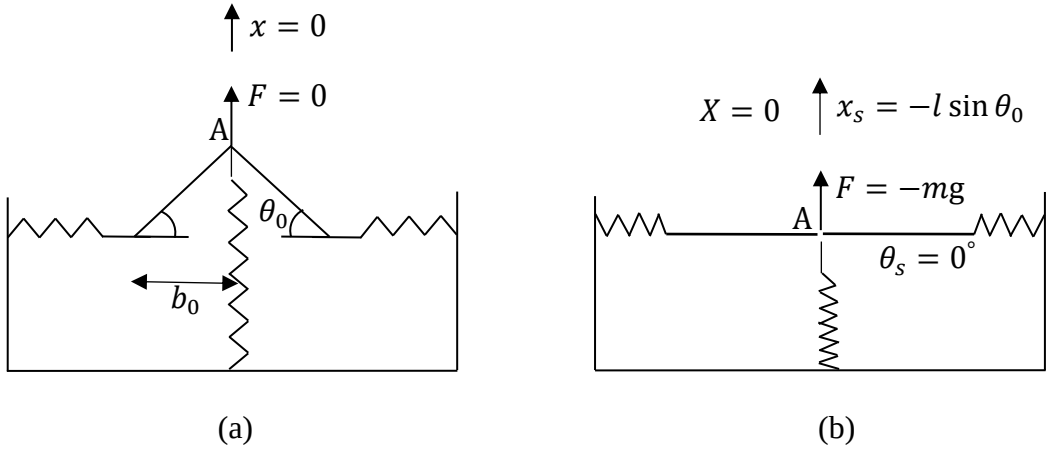

Figure 2.3. Diagram of the isolator mechanism for (a) unloaded position, (b) static equilibrium position

For any applied load F, the equation of equilibrium of point A in the vertical direction is given by

$$F = 2\,F_i \sin\theta\ + F_v\,. \tag{2.1}$$

The internal forces in the horizontal springs, vertical spring and the inclined arms are given by

$$F_h = k_h\,(b_0 - b), \tag{2.2}$$

and

$$F_i = \frac{F_h}{\cos\theta} = \frac{k_h}{\cos\theta}(b_0 - b), \tag{2.3}$$

and

$$F_v = -x\,k_v, \tag{2.4}$$

respectively.

By substituting Eq. (2.3) and Eq. (2.4) into Eq. (2.1), the static equation is rewritten as

$$F = 2k_h\,(b_0 - b)\tan\theta - x\,k_v. \tag{2.5}$$

Assuming that the static load *F* is due to the weight and the arms are designed to be horizontal $(\theta_s = 0^\circ)$at the equilibrium state(Figure 2.3 (b)), the static displacement x_s is then given by

$$x_s = -l\sin\theta_0. \tag{2.6}$$

By substituting Eq. (2.6) into Eq. (2.4), the internal force in the vertical spring is given by

$$F_v\ = k_v\,l\sin\theta_0. \tag{2.7}$$

By rewriting

$$b = \sqrt{l^2 - (l\sin\theta_0 + x)^2}, \tag{2.8}$$

and substituting Eq. (2.8) into Eq. (2.2) and Eq. (2.3), the forces in the horizontal springs and the arms are given by

$$F_h = k_h\,\left(l\cos\theta_0 - \sqrt{l^2 - (l\sin\theta_0 + x)^2}\right), \tag{2.9}$$

and

$$F_i = \frac{k_h}{\cos\theta}\left(l\cos\theta_0 - \sqrt{l^2 - (l\sin\theta_0 + x)^2}\right), \tag{2.10}$$

respectively.

If Eq. (2.9) is divided by $k_v\,l$, the dimensionless force in the horizontal springs is given by

$$\hat{F}_h = \lambda\,\left(\cos\theta_0 - \sqrt{1 - \left(\sin\theta_0 + \frac{x}{l}\right)^2}\right), \tag{2.11}$$

in which $\lambda = \frac{k_h}{k_v}$. Considering $x = x_s$, the maximum dimensionless compressive force in the horizontal springs (when $\theta_s = 0°$) for any given initial angle is given by

$$\hat{F}_h = \lambda\,(\cos\theta_0 - 1), \tag{2.12}$$

which is also shown in Figure 2.4. As illustrated, by using higher initial angle, the compression force in the horizontal springs will be higher. This is because the horizontal springs experience larger displacement and are compressed more when the arms reach a horizontal position. Using higher horizontal to vertical spring stiffness ratio λ, results in higher compression force in the horizontal equilibrium position. Overall, by increasing either λ or the initial angle θ_0, the compression in the horizontal spring increases which also increases the nonlinearity in the system.

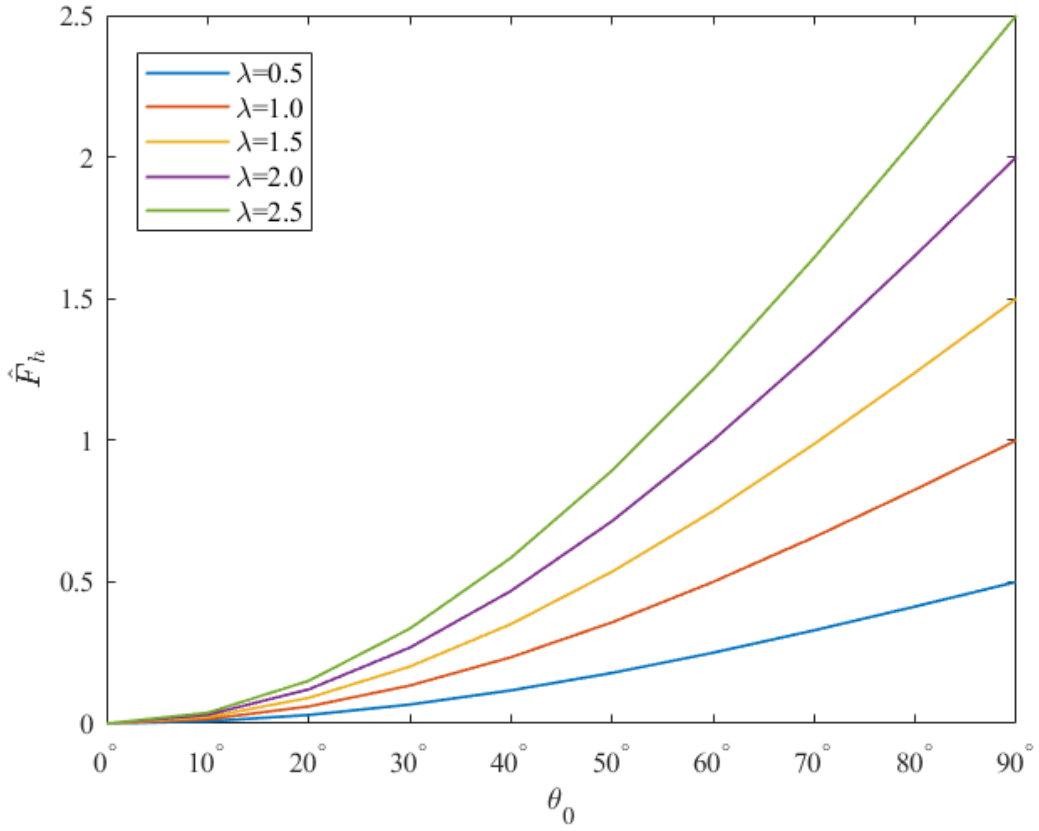

Figure 2.4. Dimensionless force in horizontal spring for various initial angles θ_0 and λ.

The force-displacement equation can be rewritten as

$$F = 2k_h\left(l\cos\theta_0 \; - \sqrt{l^2 - (l\sin\theta_0 + x)^2}\,\right) \times \frac{l\sin\theta_0 + x}{\sqrt{l^2 - (l\sin\theta_0 + x)^{\,2}}} - k_v\,x. \tag{2.13}$$

By substituting $X = l\sin\theta_0 + x$ into Eq. (2.13), This equation can be rewritten based on a new orientation (Figure 2.3 (b)) given by

$$F = 2k_h\,\left(l\cos\theta_0 - \sqrt{l^2 - X^2}\right) \times \frac{X}{\sqrt{l^2 - X^2}} - k_v\,(X - l\sin\theta_0). \tag{2.14}$$

As can be seen in Eq. (2.14), there are four parameters involved in the static behaviour of the mechanism, namely k_h, k_v, θ_0, and l.

In order to simplify this, the equation is divided by $k_v\ l$ to give the dimensionless equation

$$\hat{F} = 2\,\lambda\,\hat{X}\left(\frac{\cos\theta_0}{\sqrt{1-\hat{X}^2}} - 1\right) - \hat{X}. \tag{2.15}$$

in which $\hat{F} = \frac{F - k_v\, l \sin\theta_0}{k_v\, l}$ and $\hat{X} = \frac{X}{l}$. Using this equation, the number of unknowns decreases from four to two (initial angle θ_0 and the ratio of the stiffness as of the horizontal and vertical spring λ).

Figure 2.5 illustrates the force-displacement relationship for different initial angles θ_0 with $\lambda = 1$. As shown, for small values of θ_0 the static behaviour is close to linear. However, by increasing the initial angle for the same value of λ, the effects of nonlinearity increase.

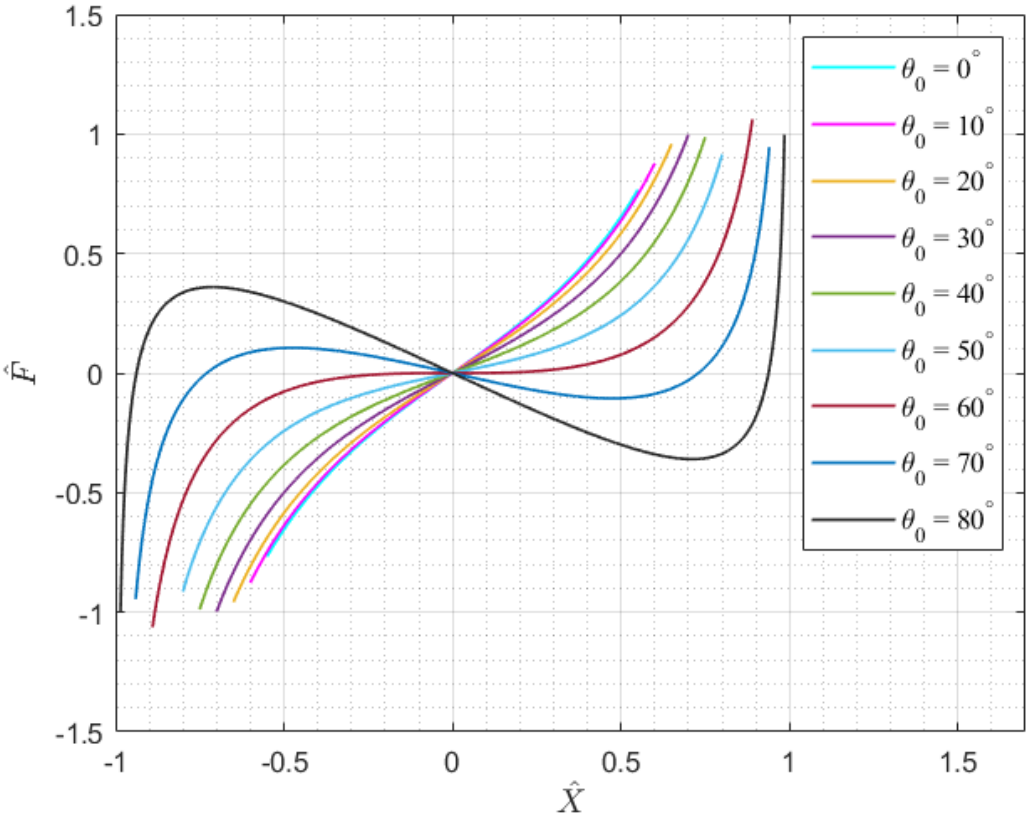

Figure 2.5. Dimensionless force-displacement graph for various initial angles $\theta_0,\ \lambda = 1$.

The equivalent vertical stiffness of the mechanism can be found from the derivative of the force F with respect to the vertical displacement. Therefore,

$$k_e = -\frac{d(F)}{dX}. \tag{2.16}$$

Consequently, substituting Eq. (2.14) into Eq. (2.16) gives

$$k_e = 2\,k_h\left(\frac{l^3\cos\theta_0}{(l^2 - X^2)^{\frac{3}{2}}} - 1\right) + k_v. \tag{2.17}$$

By dividing Eq. (2.17) by $k_v\ l$, the dimensionless equivalent vertical stiffness is given by

$$\hat{k}_e = 2\lambda\left(\frac{\cos\theta_0}{\left(1-\hat{X}^2\right)^{\frac{3}{2}}}-1\right)+1; \tag{2.18}$$

in which $\hat{k}_e = k_e/k_v$.

The force-displacement behaviour of the system with an initial angle of 60° and three values of $\lambda = 0$, 1.0, 3.0 is shown in Figure 2.6. It is evident that by increasing λ the effects of nonlinearity increase. For this case, if $\lambda \leq 1$, there will be only one equilibrium position, and if $\lambda > 1$, there will be three equilibrium positions. In the latter case, the middle equilibrium position, which occurs when $\theta_s = 0°$, the equivalent stiffness of the system is negative (shown in Figure 2.7); the middle equilibrium position is unstable. This mechanism will be designed in order to have a small positive/zero stiffness; the negative equivalent stiffness will be avoided to ensure the stability of the mechanism.

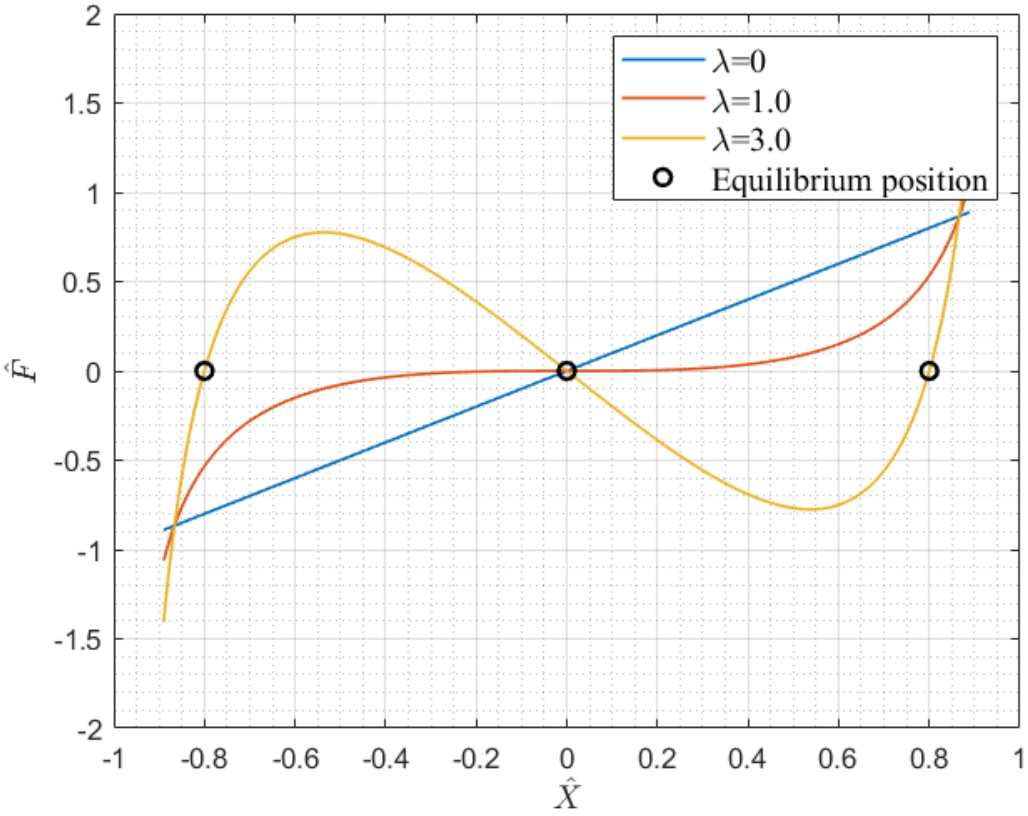

Figure 2.6. Dimensionless force-displacement graph for an initial angle of 60 degrees and λ =0, 1, and 3.

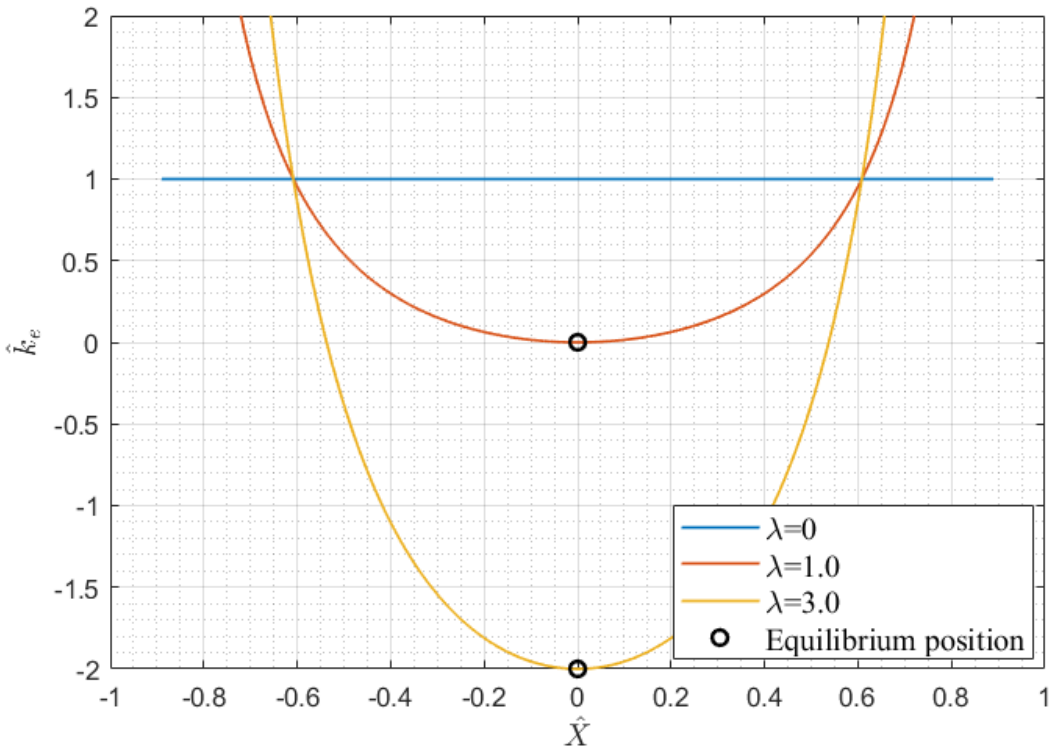

Figure 2.7. Dimensionless equivalent stiffness-displacement graph for an initial angle of 60 degrees and $\lambda = 0, 1,$ and 3.

For each initial angle and configuration, there is a combination of horizontal and vertical spring stiffness which causes zero stiffness at the static equilibrium position, giving a so-called quasi-zero-stiffness-system (QZSS). By setting $\hat{X}$ and $\hat{k}_e$ to zero in Eq. (2.18), the value of the ratio $\lambda = k_h/k_v$, which provides the QZSS, is given by

$$\lambda_{QZS} = \frac{1}{2(1-\cos\theta_0\ )} \quad . \tag{2.19}$$

By substituting Eq. (2.19) into Eq. (2.18), the equivalent stiffness of a QZSS is

$$\hat{k}_{e,QZS} = \left(\frac{1}{1-\cos\theta_0}\right)\left(\frac{\cos\theta_0}{\left(1-\hat{X}^2\right)^{\frac{3}{2}}} - 1\right) + 1 \tag{2.20}$$

which is zero when $\hat{X} = 0$ (in the static equilibrium position). Then all the static loadings are carried by the vertical spring as the horizontal springs do not provide any vertical resistance.

Figure 2.8 shows the relationship between the ratio of the spring stiffness λ and the initial angle θ_0 to satisfy the QZS condition. This is presented in Eq. (2.19). As shown, the higher initial angle needs less horizontal spring stiffness to make the QZSS.

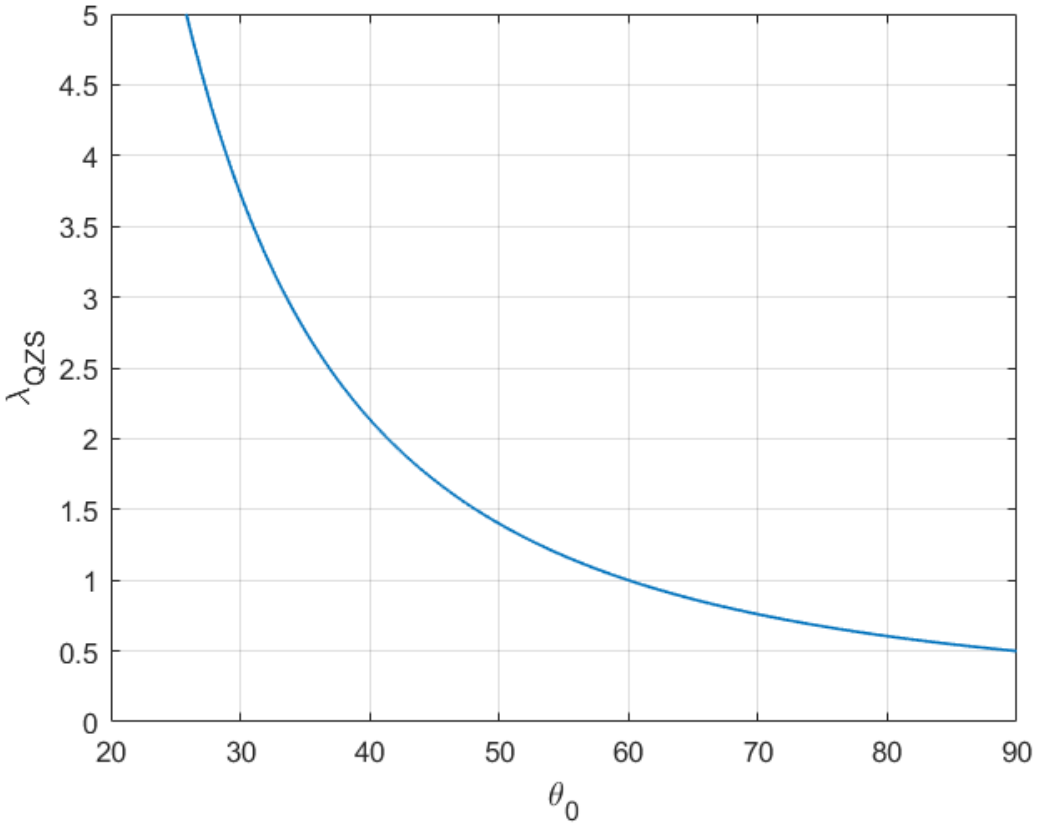

Figure 2.8. Relationship between λ and θ_0 for a QZSS

2.4 Choosing design parameters

Considering a QZSS, the vertical spring should be defined so that it carries the weight of the building solely at the equilibrium state, since the arms which would lie horizontally cannot contribute to the vertical component of the force. Therefore, k_v can be calculated by dividing the static force by the spring displacement, which is equal to the vertical projected length of the arm at the initial state. This gives

$$k_v = \frac{mg}{l \sin\theta_0} \ . \tag{2.21}$$

In the QZSS, the equivalent vertical stiffness at static equilibrium is zero. Thus, by setting $k_{e,QZS} = 0$ in Eq. (2.18), k_h can be calculated as

$$k_{h,QZS} = \frac{k_v}{2(1-\cos\theta_0\ )} \ . \tag{2.22}$$

By substituting Eq. (2.21) into Eq. (2.22), the stiffness of the horizontal spring can also be calculated directly from

$$k_{h,QZS} = \frac{mg}{2l \sin\theta_0\ (1-\cos\theta_0\ )} \ , \tag{2.23}$$

where l and θ_0 are two design parameters which need to be determined. The natural frequency of the system in the vertical direction can provide a useful criterion for this purpose. As the

frequency content of vertical earthquake excitations are richer in higher frequency components (higher than 1 Hz) [2], the vertical natural frequency of the building should be less than 1 Hz.

Since, during the vibration, the location of the mass changes, it affects the equivalent stiffness of the system. If the displacement of the system is infinitesimal around the instantaneous position of the mass, the linearised natural frequency of the system subjected to an excitation is defined as

$$\omega_{n\_QZS} = \sqrt{\frac{k_{e,QZS}}{m}} = \sqrt{\frac{k_v \hat{k}_{e,QZS}}{m}} \ . \tag{2.24}$$

If Eq. (2.20) is substituted into Eq. (2.24), therefore

$$\omega_{n\_QZS} = \sqrt{\frac{k_v}{m}} \cdot \sqrt{\left(\frac{1}{1-\cos\theta_0}\right)\left(\frac{\cos\theta_0}{\left(1-\hat{X}^2\right)^{\frac{3}{2}}} - 1\right) + 1} \ . \tag{2.25}$$

Eq. (2.25) shows that the frequency of the QZSS is a function of $\hat{X}$ which shows it varies with the displacement of the mass. The maximum value of the frequency ω_{n_QZS} should ideally remain below 1 Hz (2π rad/s) for seismic applications [2]. Therefore, to find the desirable parameter range, each factor of ω_{n_QZS} is analysed separately. Ignoring the nonlinear term, the natural frequency of the linear system is

$$\omega_n = \sqrt{\frac{k_v}{m}} \ . \tag{2.26}$$

Therefore,

$$\sqrt{\frac{k_v}{m}} \leq 2\pi \ . \tag{2.27}$$

Substituting Eq. (2.21) into Eq. (2.27) and rearranging gives

$$\theta_0 \geq \frac{g}{4\pi^2 l}, \tag{2.28}$$

which is shown in Figure 2.9. The desirable region in this graph recommends the natural frequency of the linear system to be less than 2π rad/sec (1 Hz).

On the other hand, the nonlinear term, which changes during an earthquake, should also be investigated. To do so, the dimensionless natural frequency of a linearised QZSS is introduced as

$$\widehat{\omega}_{n\_QZS} = \sqrt{\left(\frac{1}{1-\cos\theta_0}\right)\left(\frac{\cos\theta_0}{\left(1-\hat{X}^2\right)^{\frac{3}{2}}} - 1\right) + 1}, \tag{2.29}$$

where $\widehat{\omega}_{n\_QZS} = \frac{\omega_{n\_QZS}}{\sqrt{\frac{k_v}{m}}}$.

Figure 2.10 shows the relationship between the dimensionless frequency of a QZSS and the dimensionless displacement of the mass, shown in Eq. (2.29), for various initial angles. Considering the linear natural frequency $\sqrt{\frac{k_v}{m}} = 2\pi$, the dimensionless frequency should remain below 1 (the shaded zone) for any given dimensionless displacement. As shown in Figure 2.10, the maximum frequency of the system with lower initial angles changes rapidly with the displacement. For instance, for a system with initial angle of $\theta_0 = 10^{\circ}$, a displacement of $0.1l$ gives a maximum frequency of 1 Hz (considering the linear frequency $\sqrt{\frac{k_v}{m}} = 2\pi$). By increasing the displacement/length of the arm ratio (value varies for different initial angles), however, the maximum frequency exceeds 1 Hz. On the other hand, a QZSS with higher initial angles provide a wider range of displacements without exceeding frequency of 1 Hz. A QZSS with initial angle of 80°, for example, can keep the maximum frequency below 1 Hz for displacements up to 0.84 l. Therefore, higher initial angles are preferred since they allow higher displacements while keeping the maximum frequency below 1 Hz.

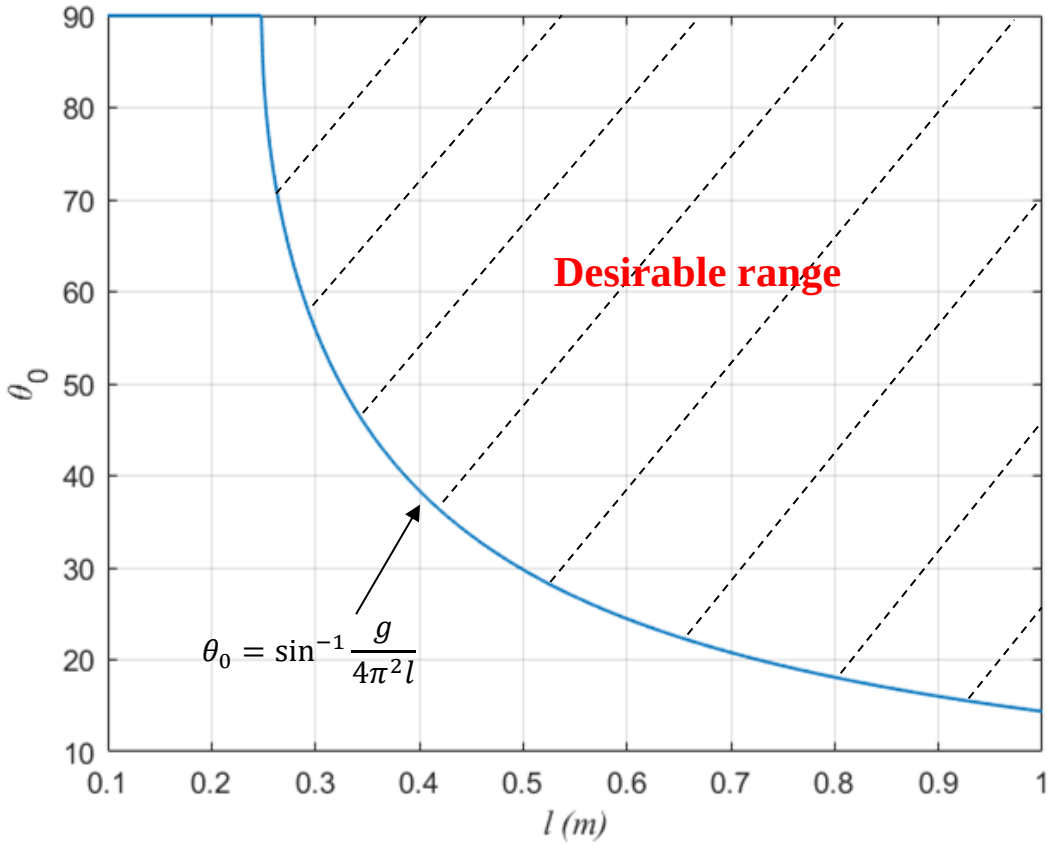

Figure 2.9. Relationship between initial angle and the length of the arms for a linear system to ensure $\widehat{\omega}_{n\_QZS} \leq 2\pi$

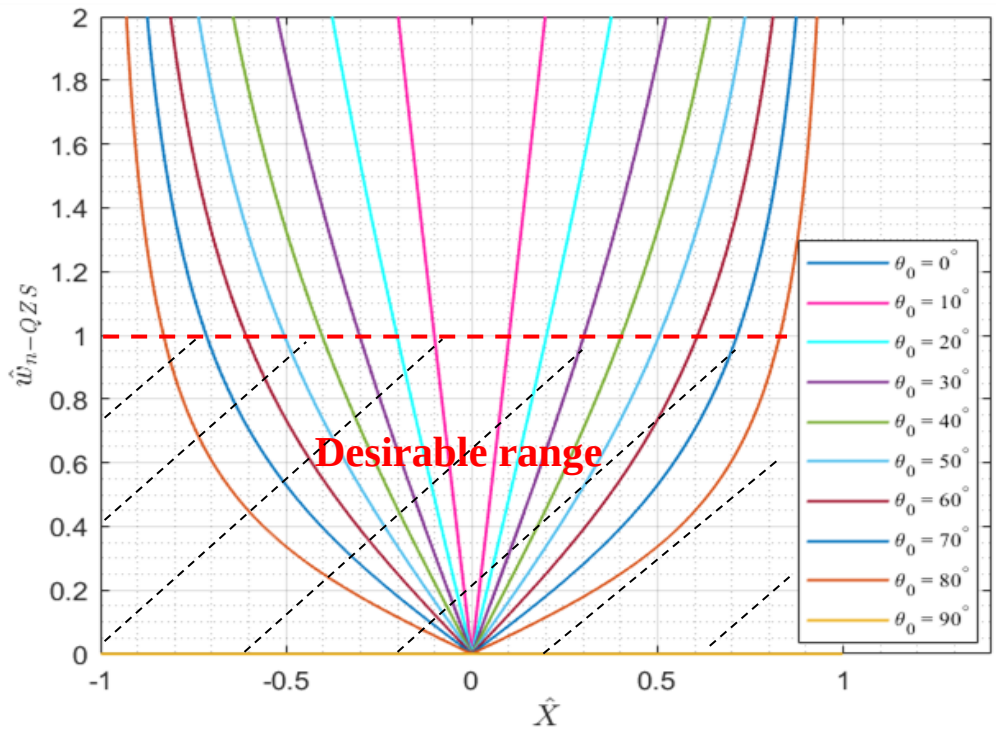

Figure 2.10. Relationship between dimensionless frequency and displacement for QZSS with large displacements

2.5 Dynamic behaviour subjected to time harmonic excitations

2.5.1 Equation of motion

In this section, the dynamic behaviour of the SDoF system with the mechanism is investigated. Figure 2.11 illustrates the dynamic model in which Y is the absolute dynamic displacement of the mass (which is measured from the static equilibrium position $\theta_s = 0$) and z is the displacement of the ground excitation.

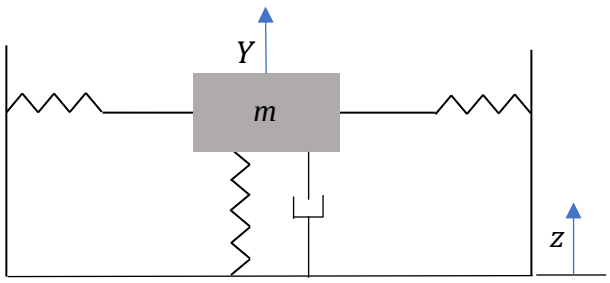

Figure 2.11. Idealized model of the mechanism with viscous damping

Therefore, the dynamic equation for the SDoF system is written around the static equilibrium position where $\theta_s = 0°$ as

$$m\ddot{Y} + c\left(\dot{Y} - \dot{z}\right) + k_e\,(Y - z) = 0\,. \tag{2.30}$$

By substituting Eq.(2.17) into the Eq. (2.30) and replace X with $Y - z$ gives

$$m\ddot{Y} + 2k_h\left(l\cos\,\theta_0 - \sqrt{l^2-(Y-z)^2}\,\right)\times\frac{(Y-z)}{\sqrt{l^2-(Y-z)^2}} + k_v\,(Y-z) + c\,(\dot{Y}-\dot{z}) = 0\,. \tag{2.31}$$

If the relative displacement of the mass to the base is defined as

$$Y' = Y - z\,, \tag{2.32}$$

and substituted into Eq. (2.31), it gives

$$m\,(\ddot{Y}' + \ddot{z}) + 2k_h\left(l\cos\theta_0 - \sqrt{l^2-Y'^2}\right)\times\frac{Y'}{\sqrt{l^2-Y'^2}} + k_v\,Y' + c\,\dot{Y}' = 0\,, \tag{2.33}$$

where

$$c = 2\xi m\omega_n\,, \tag{2.34}$$

in which ξ is a damping ratio and ω_n is the natural frequency of a linear system which is given by $\omega_n = \sqrt{\frac{k_v}{m}}$.

Dividing Eq. (2.31) by $k_v\,l$ gives the dimensionless dynamic equation of motion as

$$\frac{1}{\omega n^2}\ddot{\hat{Y}}' + 2\,\lambda\left(\cos\theta_0 - \sqrt{1^2-\hat{Y}'^2}\right)\times\frac{\hat{Y}'}{\sqrt{1^2-\hat{Y}'^2}} + \hat{Y}' + \frac{2\xi}{\omega n}\,\dot{\hat{Y}}' = -\frac{1}{\omega n^2}\ddot{Z}\,; \tag{2.35}$$

in which $\hat{Y}' = \frac{Y'}{l}$ and $Z = \frac{z}{l}$ are the dimensionless relative displacement of the mass and the dimensionless base excitation, respectively.

By defining

$$\alpha = 1 + 2\lambda\,(\cos\theta_0 - 1) \tag{2.36}$$

and

$$\beta = \lambda\,\cos\theta_0\quad, \tag{2.37}$$

Eq. (2.15) can be rewritten as

$$\hat{F} = \hat{Y}' + \frac{\hat{Y}'\left(2\,\beta - 2\,\lambda\sqrt{1-\hat{Y}'^2}\right)}{\sqrt{1-\hat{Y}'^2}}\,, \tag{2.38}$$

which can be approximated by the Taylor series given by

$$\hat{F} = \alpha\,\hat{Y}' + \beta\,\hat{Y}'^3 + \frac{3\,\beta\,\hat{Y}'^5}{4} + \frac{5\,\beta\,\hat{Y}'^7}{8} + \cdots\,. \tag{2.39}$$

As it can be seen in Figure 2.12, the Taylor series with order 3, 5, and 7 give increasingly accurate approximation for the small displacements. A Taylor series of order 3 will henceforth be used to approximate the response.

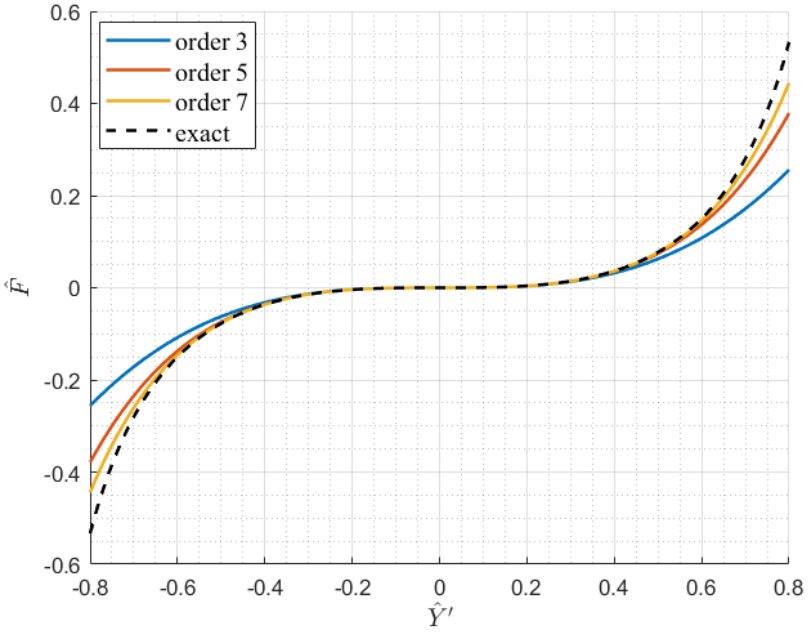

Figure 2.12. Comparison of the Taylor series of order 3, 5, and 7 with the exact solution for a QZSS

2.5.2 Analytical solution

In order to analytically solve the equation of motion for the mechanism subjected to harmonic excitations, harmonic balance method is adopted. This method has previously been used by other researchers for this system [1]. This method is an approximation of the accurate solution. It is assumed that the relative displacement of the mass is small, then the Taylor series of order 3 is used and the higher orders are ignored. Since this method is not accurate for large excitation amplitudes, it is only used to verify the MATLAB numerical model. This can be seen in Figure 2.14. Then the numerical model is used for further analysis.

By substituting the Taylor series of order 3 into Eq. (2.35), the dynamic equation of motion can be rewritten as

$$\frac{1}{\omega n^2}\ddot{\hat{Y}}' + \frac{2\xi}{\omega n}\dot{\hat{Y}}' + \alpha\hat{Y}' + \beta\hat{Y}'^3 = -\frac{1}{\omega n^2}\ddot{Z} \tag{2.40}$$

The time harmonic excitation can be written as $Z = U\cos(\omega t)$, where $U = z/l$. Consequently, the acceleration of the base is $\ddot{Z} = -U\omega^2\cos(\omega t)$. By substituting $\ddot{Z}$ into Eq. (2.40), it becomes

$$\frac{1}{\omega n^2}\ddot{\hat{Y}}' + \frac{2\xi}{\omega n}\dot{\hat{Y}}' + \alpha\hat{Y}' + \beta\hat{Y}'^3 = U\Omega^2\cos(\omega t) \tag{2.41}$$

in which $\Omega = \frac{\omega}{\omega n}$ is the dimensionless frequency ratio. If the response of the system is considered as

$$\hat{Y}' = A\cos(\omega t + \emptyset) \tag{2.42}$$

Then the $\dot{\hat{Y}}'$ and $\ddot{\hat{Y}}'$ are defined as

$$\dot{\hat{Y}}' = -A\omega\sin(\omega t + \emptyset)\ , \tag{2.43}$$

and

$$\ddot{\hat{Y}}' = -A\omega^2\cos(\omega t + \emptyset)\ . \tag{2.44}$$

Substituting Eq.(2.42), Eq.(2.43) and Eq.(2.44) into Eq.(2.41) gives

$$\begin{gathered}\Omega^2(-A\cos(\omega t + \emptyset)\ ) - 2\xi\Omega(A\sin(\omega t + \emptyset)\ ) + \alpha(A\cos(\omega t + \emptyset)\ ) \\ + \beta(A\cos(\omega t + \emptyset)\ )^3 = U\Omega^2\cos(\omega t)\end{gathered} \tag{2.45}$$

which can be expanded, using $\cos^3(\omega t + \emptyset) = \frac{3}{4}\cos(\omega t + \emptyset) + \frac{1}{4}\cos(3\omega t + \emptyset)$ and ignoring the third harmonic, to give

$$\begin{gathered}-A\Omega^2\cos(\omega t + \emptyset) - 2\xi\Omega A\sin(\omega t + \emptyset) + A\alpha\cos(\omega t + \emptyset) + \frac{3}{4}\beta A^3 \\ \cos(\omega t + \emptyset) = U\Omega^2\cos(\omega t)\end{gathered} \tag{2.46}$$

As there are only $\sin(\omega t + \emptyset)$ and $\cos(\omega t + \emptyset)$ terms in the equation. Then harmonics in both sides must be balanced. The multipliers of $\cos(\omega t + \emptyset)$ and $\sin(\omega t + \emptyset)$ on the left-hand side of Eq.(2.46) are

$$Fc = -A\Omega^2 + A\alpha + \frac{3}{4}\beta A^3 \tag{2.47}$$

and

$$Fs = -2\xi\Omega A \tag{2.48}$$

respectively. Then based on the fact that $Fc^2 + Fs^2 = (U\Omega^2)^2$, we have

$$\left(\frac{3\,\beta\,A^3}{4} - A\,\Omega^2 + \alpha\,A\right)^2 + (2\xi\Omega A)^2 = (U\Omega^2)^2. \tag{2.49}$$

Consequently, Eq. (2.49) is solved to give two values for Ω as

$$\Omega_{1,2} = \sqrt{\frac{4\,A^2\,\alpha + 3\,A^4\,\beta - 8\,A^2\,\xi^2 \pm 2\,A\sqrt{\frac{9\,A^4\,U^2\,\beta^2}{4} - 12\,A^4\,\beta\,\xi^2 + 6\,A^2\,U^2\,\alpha\,\beta - 16\,A^2\,\alpha\,\xi^2 + 16\,A^2\,\xi^4 + 4\,U^2\,\alpha^2}}{4\,(A^2 - U^2)}}. \tag{2.50}$$

The dimensionless absolute displacement of the system, is

$$\hat{Y} = A\cos(\omega t + \emptyset) + U\cos(\omega t)\,, \tag{2.51}$$

which can be expanded to give

$$\hat{Y} = (A\cos\emptyset + U)\cos(\omega t) - A\sin\emptyset\sin(\omega t) \tag{2.52}$$

Therefore, the absolute transmissibility can be written as

$$|T_a| = \frac{|\hat{Y}|}{|Z|} = \frac{\sqrt{(A\cos\emptyset + U)^2 + (A\sin\emptyset)^2}}{U} \tag{2.53}$$

which can be simplified to give

$$|T_a| = \sqrt{1 + A^2 + \frac{2A\left(\frac{3\beta A^3}{4} - A\Omega^2 + \alpha A\right)}{\Omega^2}}\,. \tag{2.54}$$

Figure 2.13 shows the transmissibility curves for various values of excitation amplitude for a QZSS with $\alpha = 0, \beta = 0.5, \lambda = 1$ and $\xi = 0.05$. As it can be seen, by increasing the excitation amplitude, the peak value increases and move toward higher frequencies.

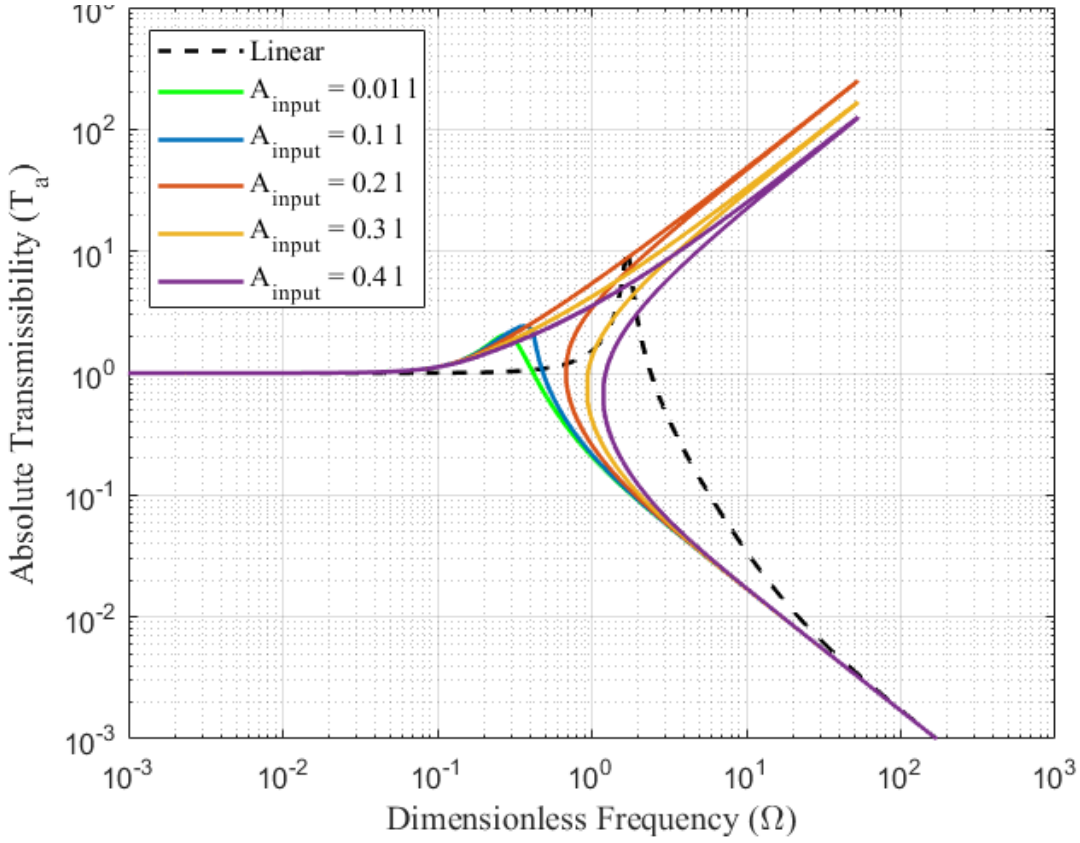

Figure 2.13. Comparing the transmissibility curves for a linear system with a QZSS with $\alpha = 0, \beta = 0.5, \lambda = 1$ and $\xi = 0.05$ and various input amplitudes

2.5.3 Numerical solution

Eq. (2.31) is solved numerically using step-by-step direct integration of the equation of motion. MATLAB ode45 solver is obtained to solve the equation. This solver is based on an explicit Runge-Kutta (4,5) formula which gives a solution for a single time step only. The default parameters are used for the solver. For instance, the relative error tolerance and maximum error tolerance are $1e^{-3}$ and $1e^{-6}$ respectively. The initial conditions include displacement and velocity. For the first step, the static displacement was used as an initial condition for the equation based on unloaded position origin and zero displacement for the equation based on equilibrium position origin. The velocity for the initial conditions in both cases are zero. The

solution for each time step is considered as initial condition to solve the equation for the following time step.

The numerical results are verified with the analytical results shown in Figure 2.14, which gives the transmissibility curve for a system with $\alpha = 0.866,\ \beta = 0.433$, $\xi = 0.05$ and $U = 0.1$. The numerical modelling correctly simulates the behaviour of the mechanism. Therefore, numerical modelling is used for more complex cases for which the analytical computation is out of reach. There is a region in the transmissibility curve where there are three possible solutions available. Two of these are stable and one is unstable. The unstable solution cannot be found using the solver as it only converges to the stable solution.

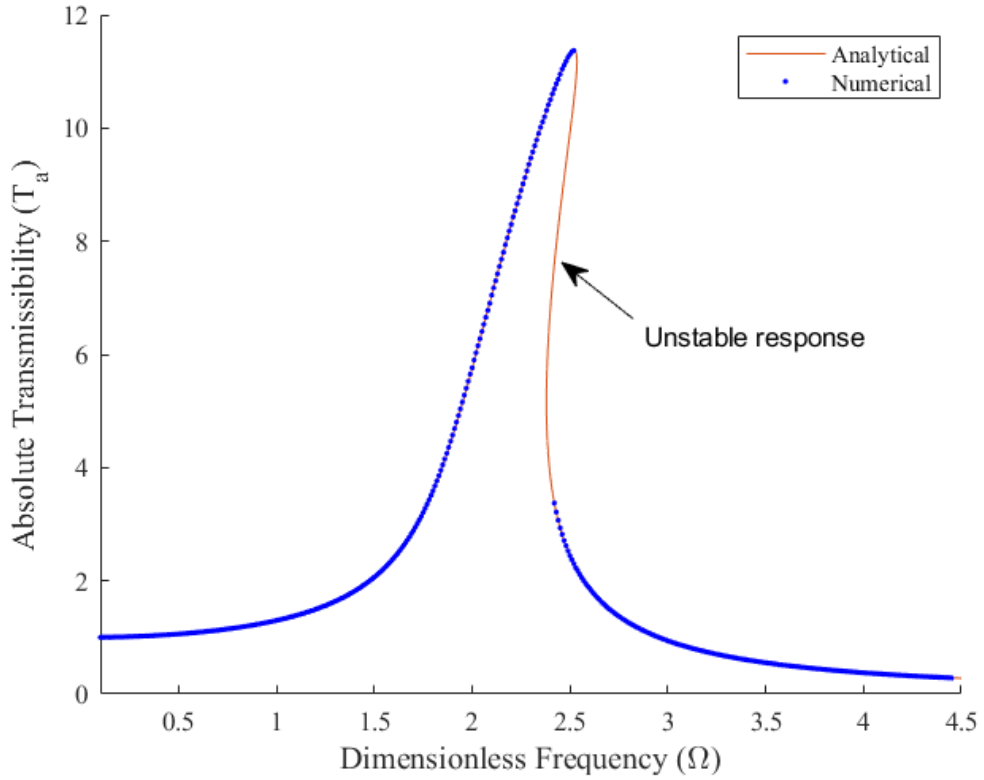

Figure 2.14. Comparison between analytical and numerical results for a system with $\alpha = 0.866,\ \beta = 0.433$, $\xi = 0.05$ and $U = 0.1$ without friction

2.6 Other equilibrium positions

The dynamic behaviour of the mechanism has been analysed for the case where the weight of the system brings the arms into the horizontal position $\theta_s = 0°$ (static equilibrium position). However, in practice, this may not be the case because of some uncertainties. Therefore, it is important to evaluate the dynamic behaviour of the system for other static equilibrium positions to see how sensitive the mechanism is to changes in the system parameters. For this purpose, two mistuning factors have been considered, which are the variation in the geometric configuration of the arms and the change in payload. Substituting Eq.(2.17) into Eq. (2.30) gives the equation of motion for any static equilibrium position

$$m\ddot{y} + c(\dot{y} - \dot{z}) + 2k_h \left(l\cos\theta_0 - \sqrt{l^2 - \left(l\sin\theta_0 + (y-z)\right)^2} \right) \times \frac{l\sin\theta_0 + (y-z)}{\sqrt{l^2 - \left(l\sin\theta_0 + (y-z)\right)^2}} + k_v\,(y-z) - mg = 0; \quad (2.55)$$

in which y is the absolute displacement of the mass from the unloaded position.

2.6.1 Mistuning

In practice, there might be a mistuning because of some error in installation. In other words, the rig may not be installed in the exact configuration for which it was designed. For instance, the initial angle of the arms with respect to the horizontal may be slightly different from the design. In this part, the performance of the mechanism is evaluated when the system is subjected to a shift in location of the payload by $0.1\ l$ and $0.01\ l$, above or below, compared to the values defined when designing the system. It is important to note that by mistuning the system, the equilibrium position is not at $\theta = 0^{\circ}$, so, it is not a QZSS anymore. The effects of mistuning on the performance of a QZSS is studied considering a system with $k_v = k_h = 140$ N/m ($\lambda = 1$), $\theta_0 = 60^{\circ}$, $l = 0.1$ m and $mg = 12$ N. The static behaviour of this mechanism is shown in Figure 2.15 (a). As illustrated, the mistuning of $0.01\ l$ (positive mistuning implies that the initial location is above the intended point) does not affect the static behaviour of the system significantly. However, by increasing this error to $0.1\ l$, the changes in the static behaviour are considerable. Moreover, by mistuning the system to a higher initial position (increasing the initial angle), the nonlinearity which causes the negative stiffness increases. As a matter of fact, a QZSS is generally designed to obtain the maximum possible negative stiffness in the system to provide a zero stiffness in the static equilibrium position while retaining stable. Therefore, by adding more nonlinearity to the system, there will be a zone with negative equivalent stiffness. In this case, there are three possible equilibrium positions, two stable and one unstable at $\theta = 0^{\circ}$. Therefore, the stable static equilibrium position will be at $\theta_s \neq 0°$.

Considering $mg = 12$ N, $\theta_0 = 45^{\circ}$ and $\lambda = 1$, the stiffness $k_v = k_h$ is calculated so that the static equilibrium position is reached at zero angle. This mechanism is not QZSS, since the equivalent stiffness at the static equilibrium system is non-zero and positive, so-called High Static Low Dynamic Stiffness System (HSLDSS). The static behaviour of this system for various mistuning values is shown in Figure 2.15 (c). As can be seen, by increasing the initial angle, the nonlinearity of the system increases and by mistuning the mass into lower initial positions, the nonlinearity reduces. However, the system remains stable with only one equilibrium position and positive stiffness at a time.

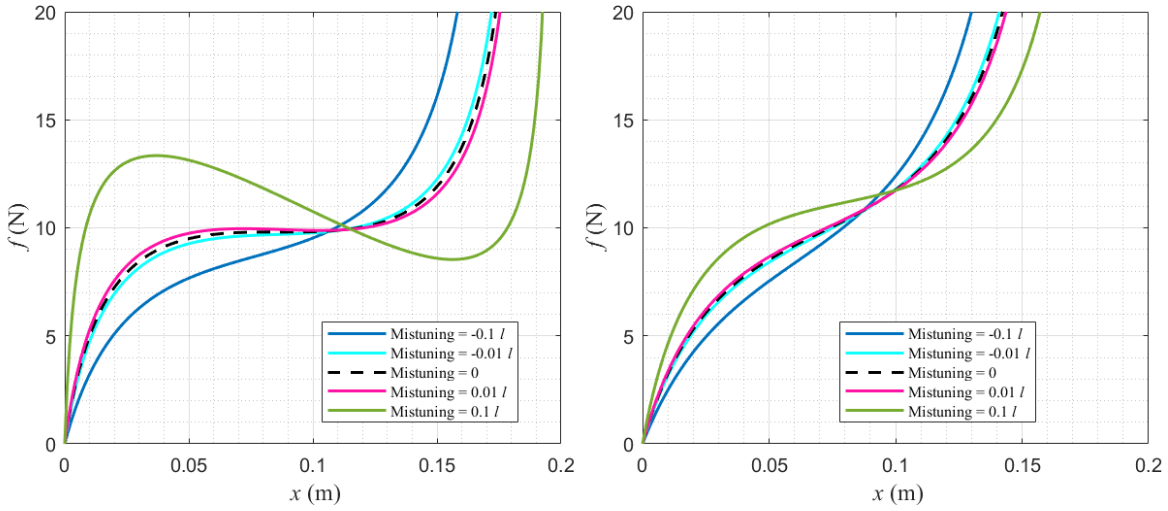

Figure 2.15. Force-displacement graph for a system $mg = 12\text{N}$, $l = 0.1\,m$ and $\lambda = 1$ with mistuning. (a) QZSS ($\theta_0 = 60^\circ$), and (b) HSLDSS ($\theta_0 = 45^\circ$)

To compare the dynamic behaviour of the QZSS and the HSLDSS with and without mistuning subjected to harmonic excitations, transmissibility of the acceleration is used. Transmissibility is defined as the ratio of the maximum amplitude of the response acceleration to the amplitude of input excitation. The peak response of the system subjected to input harmonic excitation is numerically calculated for different frequencies (the numerically obtained response is multi-harmonic in general). Figure 2.16 (a) shows the input and the response acceleration time histories of QZSS subjected to a harmonic excitation with frequency and amplitude of 0.5 Hz and 0.08g, respectively. As it can be seen, the response of the system has multiple harmonics and it takes several minutes to settles after the initial disturbance. The transmissibility then is the peak value of the response (when settled) to that of the input. So, for this case the transmissibility is 1. Subsequently, the transmissibility for different input frequencies is calculated numerically.

Figure 2.16 (b) shows the transmissibility for a QZSS with various degrees of mistuning. Comparing these two graphs (Figure 2.16 (b) and (c)), it is noted that mistuning affects the transmissibility of the QZSS system more than the HSLDSS in the frequency range bellow 3 Hz. In other words, although the QZSS without mistuning performs better than a HSLDSS and isolate wider range of frequencies, by adding a mistuning to the system, it can be seen that as there is a risk of mistuning, the HSLDSS behaves better and is more resilient than the QZSS.

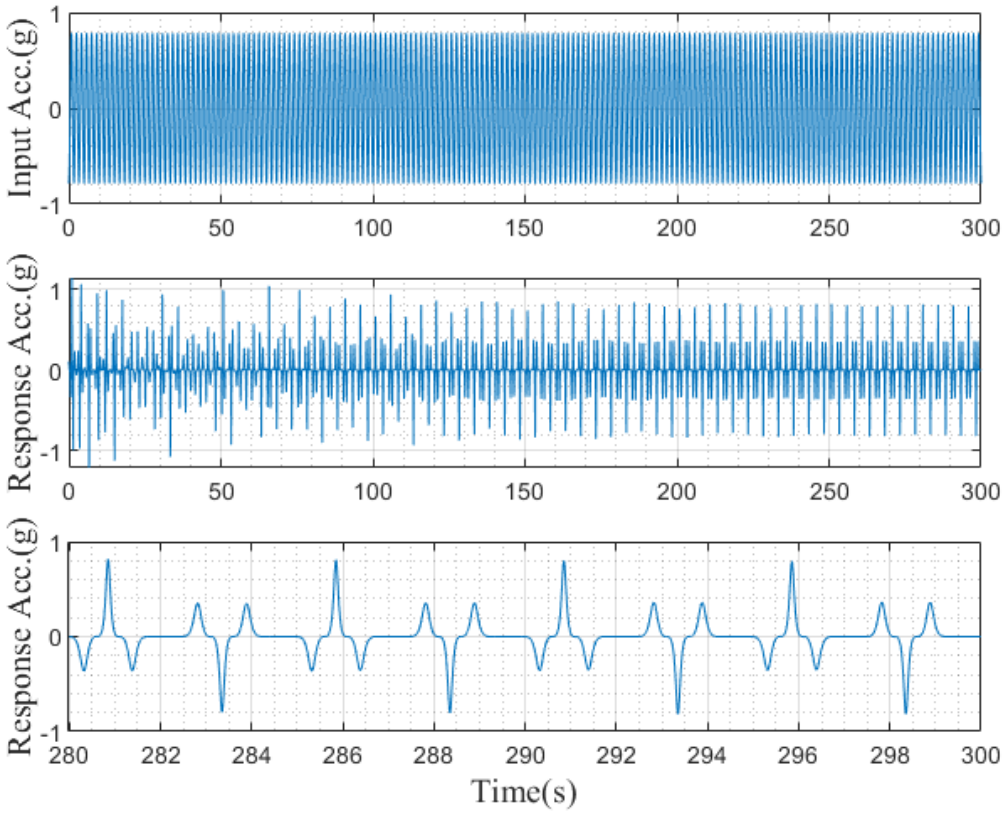

(a)

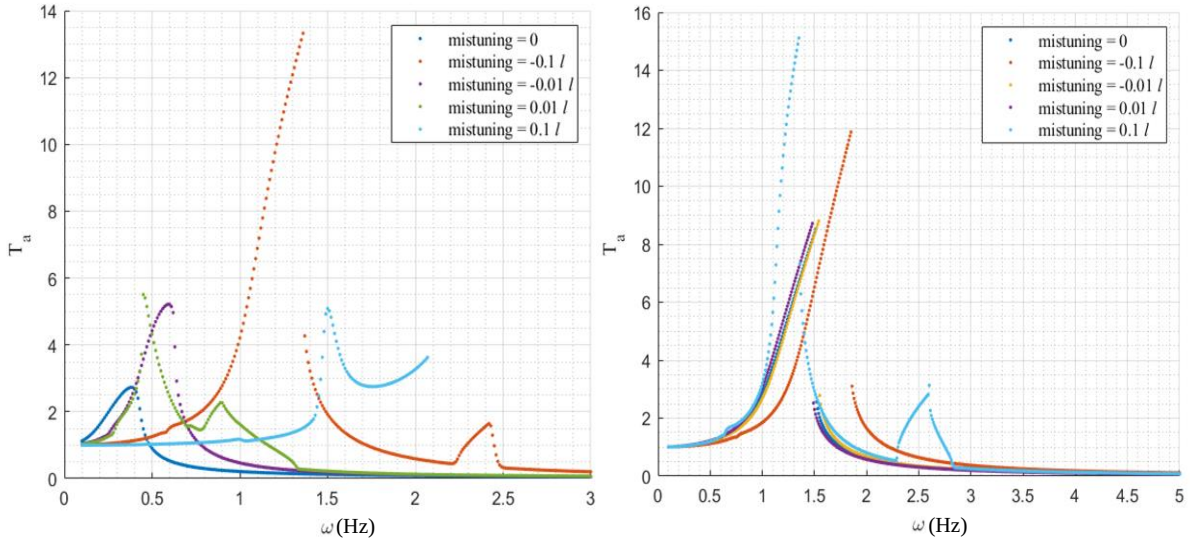

(b) (c)

Figure 2.16. (a) Input and response acceleration time histories for a QZSS $mg = 12$ N, $l = 0.1\,m$ and $\lambda = 1$ without mistuning and the excitation frequency of 0.5 Hz and amplitude of $0.8g$. (b)Transmissibility for a QZSS ($\theta_0 = 60^{\circ}$), and (c) HSLDSS ($\theta_0 = 45^{\circ}$)

Negative values of the mistuning parameter indicate that the initial position of the mass is below the intended location. As can be seen, not only does the mistuning increase the response of the system at low frequencies, but it also changes the resonance frequency of the system. It is also evident that by mistuning the mass to the higher or lower positions (except $-0.01\ l$), two other branches emerge before and after the main branch at the resonance. These two branches are called emerging branches and show harmonics at $\frac{1}{2}\omega_n$ and $2\omega_n$. For a mistuning of $-0.01\ l$, however, only one other branch is noticeable at $\frac{1}{2}\omega_n$. As mentioned before, for the case of mistuning of $0.1\ l$, the system can experience negative stiffness in some stage: the light blue dots in Figure 2.16 (b) illustrate this case. As seen at some frequencies, the numerical model did not converge to a stable solution.

The transmissibility for the HSLDSS with various values of mistuning is presented in Figure 2.16 (c). It is evident that this system is less sensitive to the mistuning in comparison to the similar QZSS shown in Figure 2.16 (b). Except for the case with $0.1\ l$ mistuning which has three branches, the response of the system has only one main branch. Moreover, the resonance frequency of the system is not affected significantly. Therefore, a system with some positive stiffness in the static equilibrium position (non-zero equivalent stiffness) is less sensitive to the mistuning than a QZSS.

2.6.2 Change in the payload

The static load on a building support varies all the time due to changes in live load. As there are many uncertainties in calculating the weight of the building and the expected live load, it is important to see how the dynamic behaviour of the system changes with various weights. In this section, the behaviour of a QZSS and another a HSLDSS, which has low stiffness at the equilibrium position but not zero, are studied for changes in the payload of $\pm 0.1\ mg$ and $\pm 0.01\ mg$. The transmissibility curves for these two systems against the variation in the payload is presented in Figure 2.17 (a) and Figure 2.17 (b).

Figure 2.17 (a) illustrates the transmissibility curves for the QZSS, which was introduced in the previous section with different payload. It is important to note that by changing the payload, the equilibrium position is not at $\theta = 0^{\circ}$, so, it is not a QZSS anymore. The response of the system with an increase in the payload of $0.01\ mg$ is similar to that of the system with a decrease in the payload of $0.01\ mg$. In other words, increasing or decreasing the payload by 1% has a similar influence on the behaviour of the QZSS. In this scenario, two other branches emerge at $\frac{1}{2}\omega_n$ and $2\omega_n$.

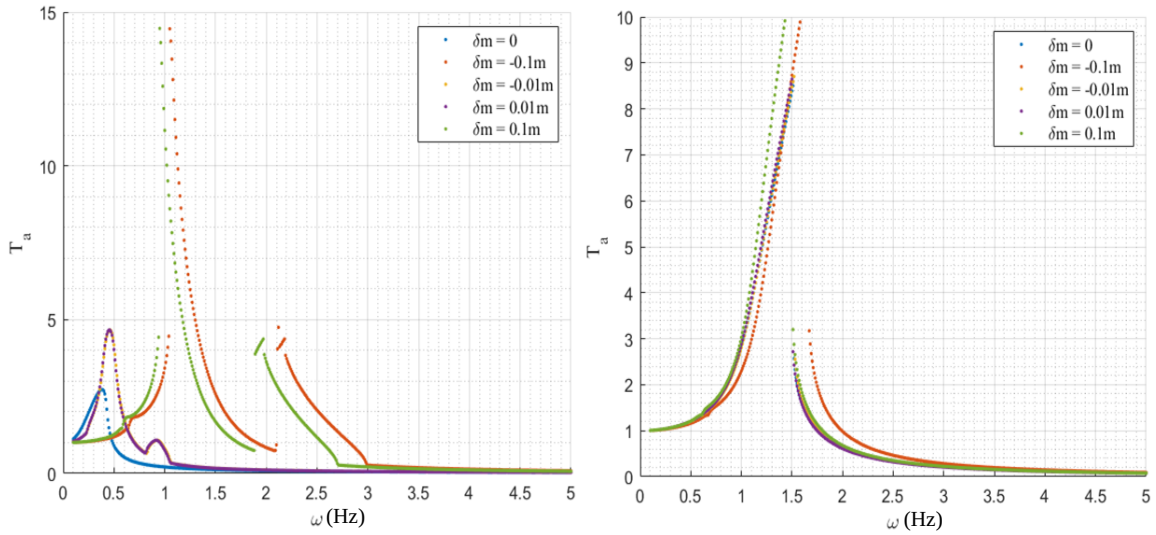

Figure 2.17. Transmissibility curves for a system $mg = 12$N and $\lambda = 1$ with changes in payload and the excitation amplitude of 0.08 g (a) QZSS ($\theta_0 = 60^\circ$), and (b) non-QZSS ($\theta_0 = 45^\circ$)

In addition, by changing the load on a QZSS by $\pm 10\%$, the resonance frequency increases. Moreover, the emerging branches at $\frac{1}{2}\omega_n$ and $2\omega_n$ become more evident. It is interesting to note that both in this case and the previous case with a $\pm 1\%$ change in payload, the behaviour of the system is very similar with a slight shift of the resonance peak.

Considering a HSLDSS with $mg = 12$N, $\theta_0 = 45^\circ$ and $\lambda = 1$, the stiffness $k_v = k_h$ is calculated in order to have the static equilibrium position at zero angle. The transmissibility curves for this system are presented in Figure 2.17 (b), which shows that this system is much less sensitive to the variation of the weight of the system in comparison to the QZSS. Moreover, the emerging branches are not well formed.

2.7 Mechanism with friction

Friction is a complicated phenomenon which exists to some extent in all mechanisms, and in many cases the effects of friction cannot be neglected. For this specific mechanism, some dry friction was observed (stick and slip behaviour) from the experiments conducted for this study which is explained in chapter 5 and needs to be considered in the analysis. The dry friction has been addressed by other researchers for a similar mechanism [3; 4] as well. Because of the complexity, it is difficult to identify the main source. Rubbing of surfaces, from springs on guide rods for instance, is the main source of friction in this mechanism. The friction force can be in both the horizontal and vertical directions. The model including dry friction is shown in Figure 2.18, which illustrates the dry friction elements for this mechanism.

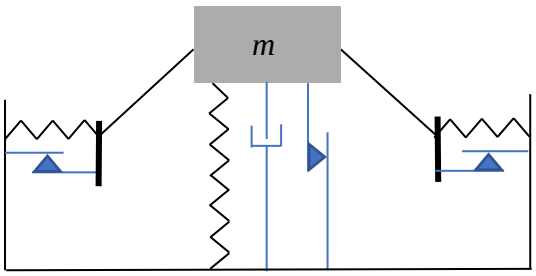

Figure 2.18. Idealized model for the mechanism with viscous damping and Coulomb friction

There have been many models proposed for dry friction, or Coulomb friction, such as stick-slip model (signum function), the smooth Coulomb model, velocity-based model etc. [5]. In this study, the continuous Coulomb friction model has been chosen for the numerical modelling in order to avoid computational difficulties caused by force discontinuities in a stick-slip model. This model has been proven to be an accurate approximation for the signum function [6]. Figure 2.19 shows the continuous Coulomb friction model which is used in this study. This model illustrates $f_d \tanh\left(\frac{\dot{Y}'}{v_d}\right)$, in which f_d refers to the constant asymptotes for the dynamic friction force and v_d is the velocity tolerance which is a real number in the neighbourhood of zero.

By adding the dry friction terms for the horizontal and the vertical motion to Eq. (2.33), the equation of motion is written as

$$m\left(\ddot{Y}' + \ddot{z}\right) - 2k_h\left(\sqrt{l^2 - Y'^2} - l\cos\theta_0\right) \times \frac{Y'}{\sqrt{l^2 - Y'^2}} + k_v\, Y' + c\,\dot{Y}' + f_{dv}.\tanh\left(\frac{\dot{Y}'}{v_d}\right) + 2\frac{Y'}{\sqrt{l^2 - Y'^2}} f_{dh}.\tanh\left(\frac{\dot{Y}'_h}{v_d}\right) = 0 \quad (2.56)$$

in which f_{dv} and f_{dh} are constant asymptotes for the friction forces in the vertical and horizontal direction respectively, $\dot{Y}'_h$ is the velocity in the horizontal direction which is derived from differentiating the horizontal displacement $\left(\sqrt{l^2 - Y'^2} - l\cos\theta_0\right)$ with respect to time. This parameter is written as

$$\dot{Y}'_h = \frac{Y'}{\sqrt{l^2 - Y'^2}}\dot{Y}'. \quad (2.57)$$

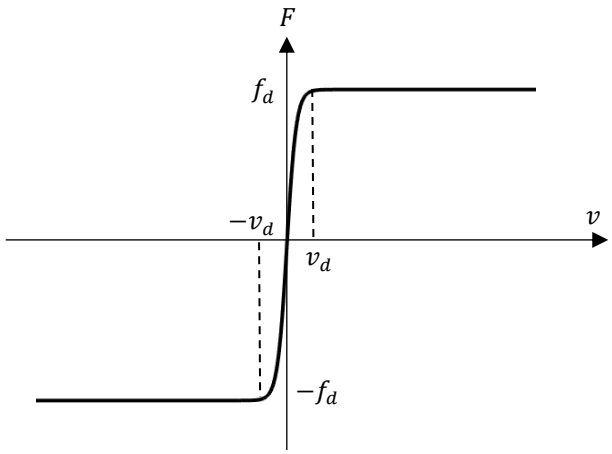

Figure 2.19. Smooth Coulomb friction model

Figure 2.20 illustrates the transmissibility of the system with different maximum vertical friction forces defined as a fraction of mg. For this mechanism, parameters are taken as $\alpha = 0.866$, $\beta = 0.433$, $\lambda = 0.5$, $\xi = 0.05$, $v_d = 0.002$ and with a harmonic excitation amplitude of 0.1 l. As can be seen, by increasing the friction force, the stick part of the graph widens and the response of the system at lower frequencies decreases significantly, while the response increases at higher frequencies, around 20% at 3 Hz for $f_{dv} = 0.3\,mg$. As the higher frequencies (greater than 1.5 Hz) are of importance in earthquake applications, it is desirable to minimize the friction in the vertical elements of the mechanism to gain more isolation in the system.

The effect of friction in the horizontal elements, however, is observed to be less severe (Figure 2.21). Although it decreases the peak in the resonance area, the increase at higher frequencies is imperceptible. Therefore, taking advantages of some friction in the horizontal direction may be useful for reducing the response around resonance.

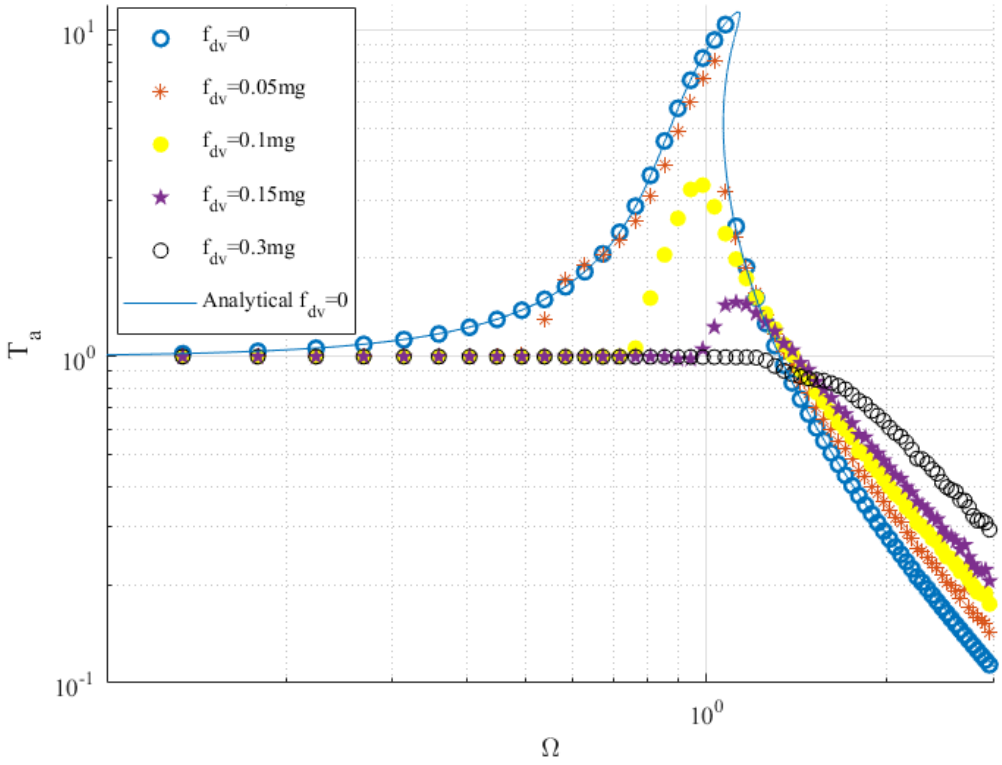

Figure 2.20. Absolute transmissibility curves for various values of vertical friction for a system with $\alpha = 0.866$, $\beta = 0.433$, $\lambda = 0.5$, $\xi = 0.05$, $v_d = 0.002$ and $f_{dh} = 0$

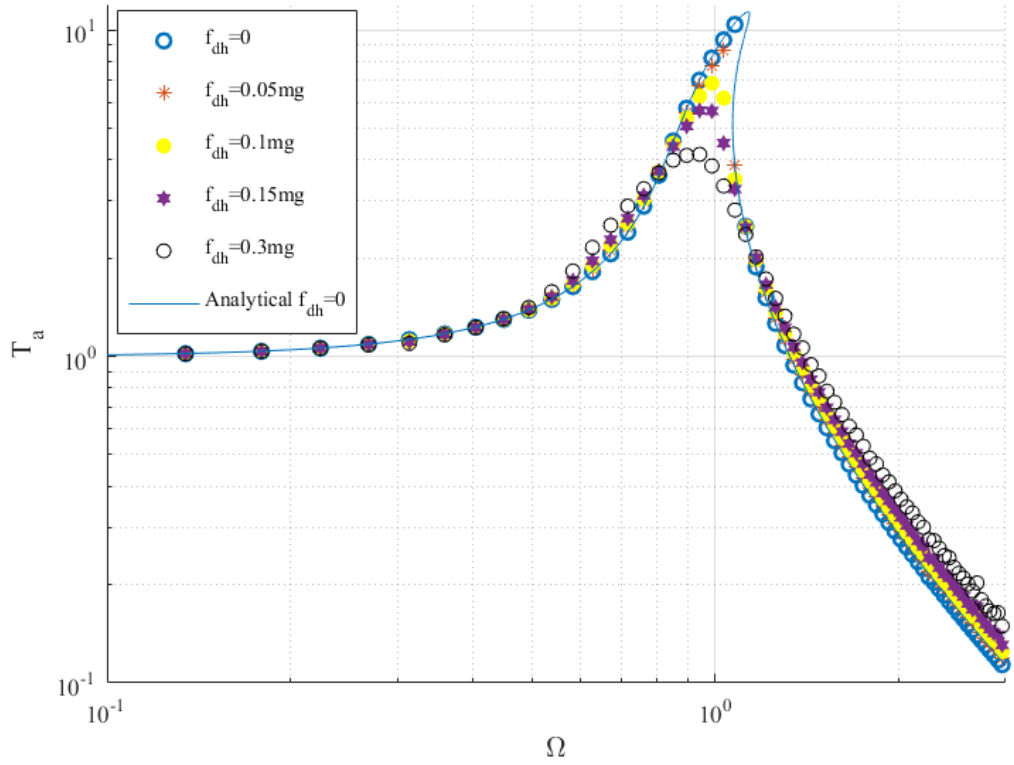

Figure 2.21. Absolute transmissibility curves for various values of vertical friction for a system with $\alpha = 0.866$, $\beta = 0.433$, $\lambda = 0.5$, $\xi = 0.05$, $v_d = 0.002$ and $f_{dv} = 0$

2.8 Conclusion

In this chapter, the equation of motion for HSLDSS including friction effects subject to base-excitations was developed and the design parameters were identified and studied. As expected, the QZSS was found to be the most effective isolation system for harmonic excitation, and the ways of designing the parameters for the QZSS were provided. In addition, the effects of the tolerance in the initial configuration of the system, and the uncertainty in the weight of the system were considered. The results show that the dynamic behaviour of QZSS is highly sensitive to these changes and is susceptible to become unstable. while designing the system with less nonlinearity decreases the sensitivity.

In addition, the effects of dry friction in both vertical and horizontal directions were modelled using Tanh function and the results were compared. The results indicate that friction forces in both horizontal and vertical directions decrease the transmissibility at resonance while they increase it in the high frequency range. Therefore, the friction in the system must be minimal to get a higher isolation performance in the high frequency range.

2.9 References

[1] Le, T. D., & Ahn, K. K. (2011). A vibration isolation system in low frequency excitation region using negative stiffness structure for vehicle seat. *Journal of Sound and Vibration, 330*(26), 6311-6335.

[2] NZS 9781776646029 1776646029, *Structural design actions – Part 5: Earthquake actions standard, Amendment 1*.

[3] Liu, X., Zhao, Q., Zhang, Z., & Zhou, X. (2019). An experiment investigation on the effect of Coulomb friction on the displacement transmissibility of a quasi-zero stiffness isolator. *Journal of Mechanical Science and Technology*.

[4] Donmez, A., Cigeroglu, E., & Ozgen, G. O. (2020). An improved quasi-zero stiffness vibration isolation system utilizing dry friction damping. *An International Journal of Nonlinear Dynamics and Chaos In Engineering Systems, 101*(1), 107-121.

[5] Pennestrì, E., Rossi, V., Salvini, P., & Valentini, P. P. (2016). Review and comparison of dry friction force models. *Nonlinear Dynamics, 83*(4), 1785-1801.

[6] Mostaghel, N. (2005). A non-standard analysis approach to systems involving friction. *Journal of Sound and Vibration, 284*(3-5), 583-595.

Chapter 3.
Numerical modelling for earthquake excitation and designing variables

3.1 Introduction

In the previous chapter, the equations of motion for static and dynamic behaviour of the isolator have been derived. Moreover, the solution for harmonic excitation was provided and the numerical model was verified by the analytical results.

In this chapter, the dynamic behaviour of the mechanism subjected to earthquake excitation is investigated. A set of 23 near-fault earthquake time histories are used as inputs for selecting suitable design variables. Moreover, the behaviour of a suggested quasi-zero-stiffness system (QZSS) is compared with a linear system as well as a high-static-low-dynamic-stiffness system (HSLDSS) with small stiffness in the static equilibrium position.

In the next chapter, experimental model will be presented as well as the equipment which were used for the tests.

3.2 Design objectives

3.2.1 Earthquake excitation selection

In this chapter, 23 historical near-fault earthquakes are taken from the PEER ground motion database website [1] and used to find the suitable design parameters of the isolator. In near-fault areas (less than 20 km from a fault), the intensity of the vertical component of earthquakes is usually more significant than for other areas. As it was mentioned in the literature review, the spectral acceleration of a building with a natural frequency of more than 1 Hz subjected to a vertical excitation can exceed 1.5 time the horizontal one in near-field areas [2]. Therefore, a set of 23 earthquakes with a magnitude of 6.5 (in the Richter scale) or more and less than 15 km distance from a fault are chosen for this study. Table 3-1 shows the year and station of occurrence, magnitude (M), distance from the source (Rcl), and the average shear velocity at 30 m depth (VS30) of each signal as well as the characteristics of the vertical component of these earthquakes including peak ground acceleration (PGA), velocity (PGV) and displacement (PGD). These earthquakes are also used in other publications [3; 4].

Table 3-1. Near-fault strong vertical ground motions [1]

No.	Earthquake	Year	Station	M (Richter)	Rcl (km)	VS30 (m/s)	PGA (g)	PGV (cm/s)	PGD (cm)
1	Tabas, Iran	1978	Tabas	7.4	2.1	767	0.64	40.89	12.3
2	Imperial Valley	1979	EC Meloland Overpass FF	6.5	0.1	186	0.24	18.9	9.6
3	Imperial Valley	1979	El Centro Array #7	6.5	0.6	211	0.58	27.1	10.0
4	Loma Prieta	1989	LGPC	6.9	3.9	478	0.90	55.9	2.0
5	Erzincan,	1992	Erzincan	6.7	4.4	275	0.23	16.4	10. 5
6	Northridge	1994	Jensen Filter Plant	6.7	5.4	373	0.35	31.2	7.5
7	Northridge	1994	Newhall - W Pico Rd Canyon	6.7	5.5	286	0.30	28.6	13.1
8	Northridge	1994	Rinaldi Receiving Sta	6.7	6.5	282	0.96	42.2	3.7
9	Northridge	1994	Sylmar - Converter Sta	6.7	5.4	251	0.61	26.1	8.3
10	Northridge	1994	Sylmar - Converter Sta East	6.7	5.2	371	0.48	120	34.0
11	Northridge	1994	Sylmar Olive View Med FF	6.7	5.3	441	0.54	18.6	7.9
12	Kobe, Japan	1995	Port Island	6.9	3.3	198	0.57	62.1	27.8
13	Kobe, Japan	1995	Takatori	6.9	1.5	256	0.28	16.2	4.4
14	Kocaeli, Turkey	1999	Yarimca	7.4	4.8	297	0.24	30.8	29.5
15	Chi-Chi, Taiwan	1999	TCU052	7.6	0.7	579	0.20	144.0	154.0
16	Chi-Chi, Taiwan	1999	TCU065	7.6	0.6	306	0.26	69.4	57.3
17	Chi-Chi, Taiwan	1999	TCU068	7.6	0.3	487	0.53	213.0	222.6
18	Chi-Chi, Taiwan	1999	TCU084	7.6	11.2	553	0.32	25.6	13.2
19	Chi-Chi, Taiwan	1999	TCU102	7.6	1.5	714	0.18	68.4	51.6
20	Duzce, Turkey	1999	Duzce	7.2	6.6	276	0.35	20.2	20.8
21	Bam, Iran	2003	Bam	6.6	1.7	487.4	0.97	39.9	8.5
22	Christchurch,	2010	Heathcote Valley Primary	6.2	3.4	422	2.18	40.0	23.3
23	Lucerne, Landers	1992	Lucerne	7.28	2.19	1369	0.818	97.6	29.8

One of the factors to quantify the severity of a ground motion is a frequency content [5]. This characteristic can be observed using spectral accelerations, which represent the responses of elastic linear SDoF systems subjected to harmonic excitations with specific frequencies. Frequency content of a ground motion can also be obtained from Discrete Fourier Transform (FFT) of the acceleration time history. Since the system studied in this research is nonlinear, FFT is chosen to show the frequency contents of the inputs. To

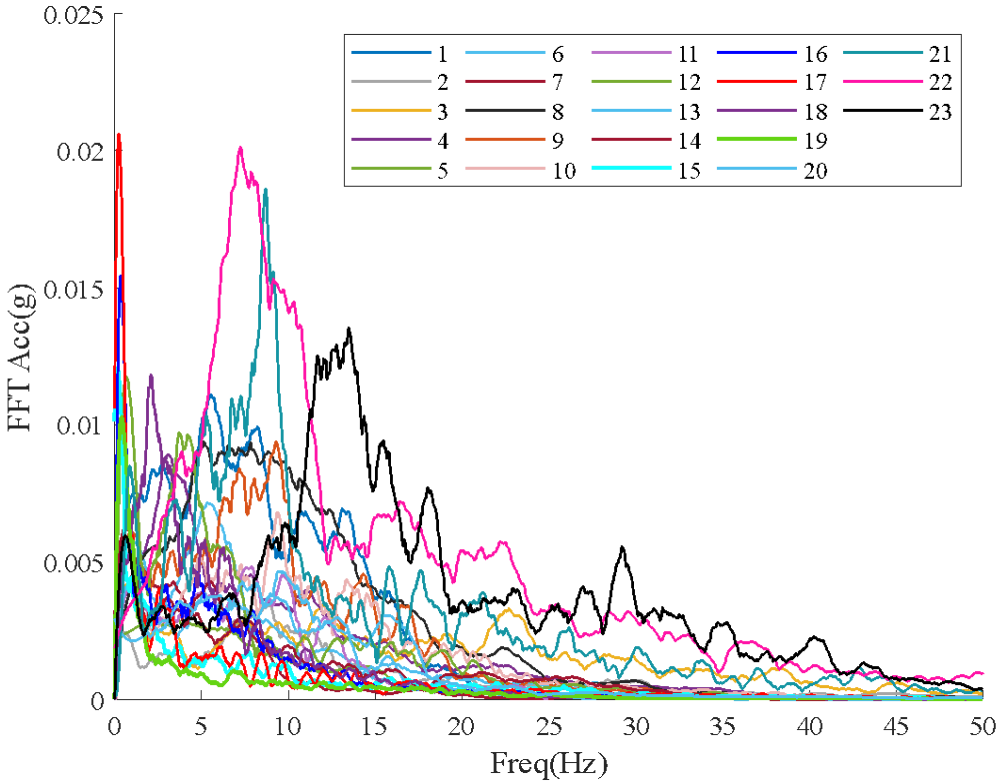

Figure 3.1. Fast Fourier Transform of acceleration for 23 near-fault earthquake signals [1]

indicate the FFT for the 23 near-fault earthquake signals. The graphs have been smoothened using sgolayfilt(order,framelen) function in MATLAB in order to decrease the noises and see the general trend of the graphs. Pronominal order (order) 3 and frame length (framelen) of 101 was found to be suitable parameters for this function to meet the purpose. As can be seen, most of the earthquake accelerations are rich in higher frequencies (higher than 1 Hz). For instance, the Bam and Christchurch earthquakes, Nos. 21 and 22, have a substantial frequency content around 5-10 Hz. Therefore, an isolator with a natural frequency of less than 1 Hz is expected to considerably reduce the response of the system. However, the Northridge (No. 6), Kobe (No. 12) and the Chichi earthquake from a few different stations (No. 15, 16, 17 and 19) have significant low frequency content. Therefore, the response of a system with an isolator could even be amplified due to these input signals (because of resonance) even with an isolator giving a natural frequency lower than 1 Hz.

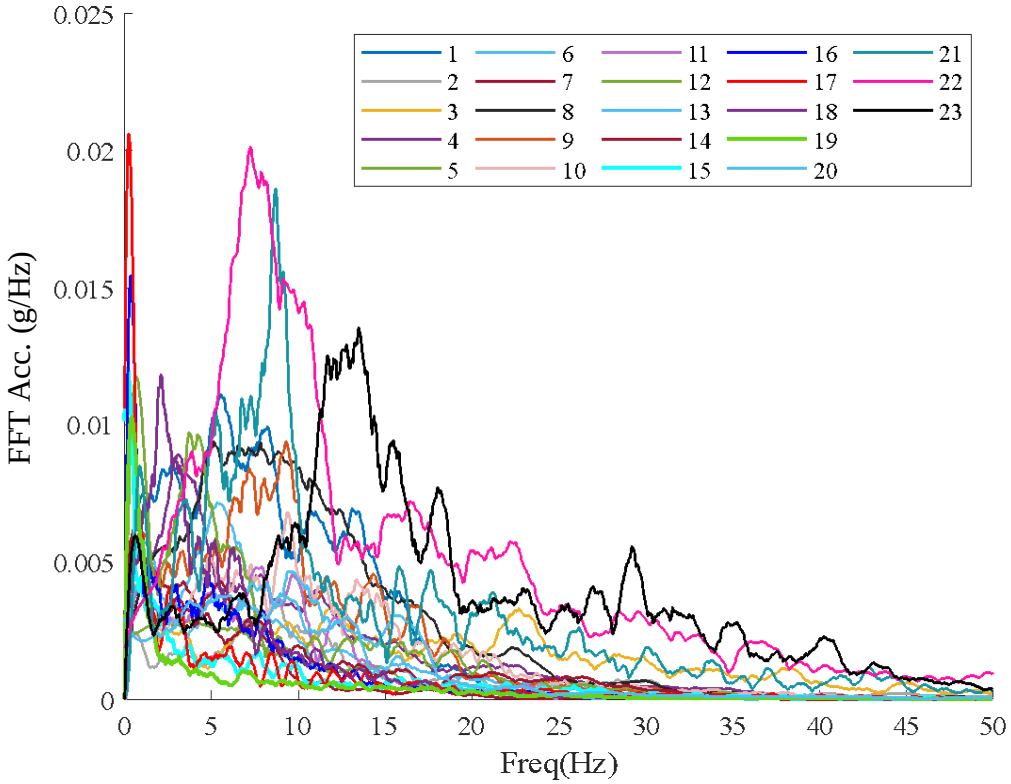

Figure 3.1. Fast Fourier Transform of acceleration for 23 near-fault earthquake signals [1]

3.2.2 Performance criteria

The criteria which are used for evaluating the performance of the mechanisms for the earthquake applications are based on the following factors, with lower values indicating better performance:

(a) Maximum acceleration ratio: defined as the ratio of the maximum magnitude response acceleration to the maximum magnitude base acceleration.

(b) Maximum Root Mean Square (RMS) acceleration ratio: the RMS ratio of the response/base strong motion acceleration. The RMS criterion is calculated for the strong motion duration of the signal as this part includes the majority of energy which is the main cause of damage to structures [6]. To do this, the duration of the strong motion is calculated based on a percentage of cumulative energy [7] given by

$$CE = \int a^2(t)dt, \tag{3.1}$$

in which a is the base acceleration time history and t is time. The part of the signal with CE between 5% and 95% gives the strong ground motion which is used to determine the RMS response.

(c) Maximum relative displacement ratio: the ratio of the maximum relative response displacement to that of the base.

(d) Maximum nondimensional force amplification

$$f_{tr} = \left(\frac{\ddot{y} + g}{g}\right). \tag{3.2}$$

This criterion illustrates the amplification of the compressive force in the system due to earthquake excitation and is defined in terms of the payload. For instance, if $f_{tr} = 1.4$, it means that the maximum compressive force in the system during an earthquake reaches 1.4 times the static payload.

3.3 Designing of QZSS parameters

In this section, the variables in a QZSS are selected based on the earthquake signals tabulated in the previous section.

In this process, the effect of the length of the arms, the initial angle of the arms, the damping coefficient and horizontal friction element (nonlinear friction force) and vertical friction element (linear friction force) will be considered. It should be noted that the stiffnesses are determined according to the QZSS equations given in Chapter 2.

3.3.1 Length of the arms (l)

The length of the arms is one of the design variables. This length must provide enough stroke in the event of an earthquake. In other words, the length of the arms must allow enough space for the relative displacement of the mass. Therefore, the 23 near-fault earthquakes are taken to find a suitable option for this variable. On the other hand, a shorter length would be an advantage as it decreases the required space and provides a viable option for retrofitting buildings.

The equation of motion Eq. (2.56) is considered in this section to find the suitable design variables. To simplify this equation for this purpose, the horizontal and vertical friction forces can be defined as a fraction of the payload and represented as

$$f_{dh} = \eta_h mg \tag{3.3}$$

and

$$f_{dv} = \eta_v mg \tag{3.4}$$

respectively, in which η_h and η_v are constant ratios for the horizontal and vertical friction forces and mg is the static payload. By substituting Eq. (2.21) and Eq. (2.26) into Eq.(2.34), the damping term is rewritten as

$$c = 2\xi m \sqrt{\frac{g}{l \sin\theta_0}}. \tag{3.5}$$

Therefore, by considering the system as a QZSS, Eq. (2.21), Eq. (2.23), Eq. (3.3), Eq. (3.4), Eq. (3.5) and Eq. (2.57) are substituted into Eq. (2.56), and expressed as

$$m\left(\ddot{Y}' + \ddot{z}\right) - \frac{mg}{l\sin\theta_0\,(1-\cos\theta_0\ )}\left(\sqrt{l^2 - Y'^2} - l\cos\theta_0\quad\right) \times \frac{Y'}{\sqrt{l^2 - Y'^2}} + \frac{mg}{l\sin\theta_0}\,Y' + 2\xi m\sqrt{\frac{g}{l\sin\ \theta_0}}\,\dot{Y}' + \eta_v mg.\tanh\left(\frac{\dot{Y}'}{v_d}\right) + 2\frac{Y'}{\sqrt{l^2 - Y'^2}}\eta_h mg.\tanh\left(\frac{Y'\dot{Y}'}{v_d\sqrt{l^2 - Y'^2}}\right) = 0 \tag{3.6}$$

Then m can be cancelled out from the equation which can be expressed as

$$\ddot{Y}' - \frac{g}{l\sin\theta_0\,(1-\cos\theta_0)}\left(\sqrt{l^2 - Y'^2} - l\cos\theta_0\right) \times \frac{Y'}{\sqrt{l^2 - Y'^2}} + \frac{g}{l\sin\theta_0}\,Y' + 2\xi\sqrt{\frac{g}{l\sin\theta_0}}\,\dot{Y}' + \eta_v g.\tanh\left(\frac{\dot{Y}'}{v_d}\right) + 2\frac{Y'}{\sqrt{l^2 - Y'^2}}\eta_h g.\tanh\left(\frac{Y'\dot{Y}'}{v_d\sqrt{l^2 - Y'^2}}\right) = -\ddot{z} \tag{3.7}$$

As can be seen, this equation only depends on two design variables, θ_0 and l. Consequently, θ_0 is also replaced by $\frac{g}{4\pi^2 l}$, from Eq. (2.28), considering 1 Hz as the target natural frequency of the system. Then the equation of motion will only depend on l, the length of the arms, and is given by

$$\ddot{Y}' - \frac{4\pi^2}{\left(1 - \sqrt{1 - \left(\frac{g}{4\pi^2 l}\right)^2}\right)}\left(\sqrt{l^2 - Y'^2} - l\sqrt{1 - \left(\frac{g}{4\pi^2 l}\right)^2}\ \right) \times \frac{Y'}{\sqrt{l^2 - Y'^2}} + 4\pi^2 Y' + 4\xi\pi\dot{Y}' + \eta_v g.\tanh\left(\frac{\dot{Y}'}{v_d}\right) + 2\frac{Y'}{\sqrt{l^2 - Y'^2}}\eta_h g.\tanh\left(\frac{Y'\dot{Y}'}{v_d\sqrt{l^2 - Y'^2}}\right) = -\ddot{z} \tag{3.8}$$

Therefore, the suitable length of the arms for a QZSS (at equilibrium) is the one which minimize the response of the system subjected to the 23 near-fault earthquakes. Considering $\xi = 0.05$, $\eta_v = \eta_h = 0$, the response of the system with various length of the arms, from 0.20 m to 2 m, are presented in the graphs.

Figure 3.2 shows the ratio of the maximum acceleration of the response to the maximum acceleration of the input signal for all the earthquake input signals tested. As is illustrated, for the some of the earthquake signals (No. 10, 12, 14, 15, 16, 17, and 19), the maximum acceleration ratio initially reduces by increasing the length of the arms from 0.2 m to around 0.6 m. However, the minimum of 0.4 m for the arms is necessary to provide a required stroke in some cases (there is no response applicable for 0.2 m and 0.3 m arms subjected to some earthquake signals, No. 10, 12, 16, 17, and 19).

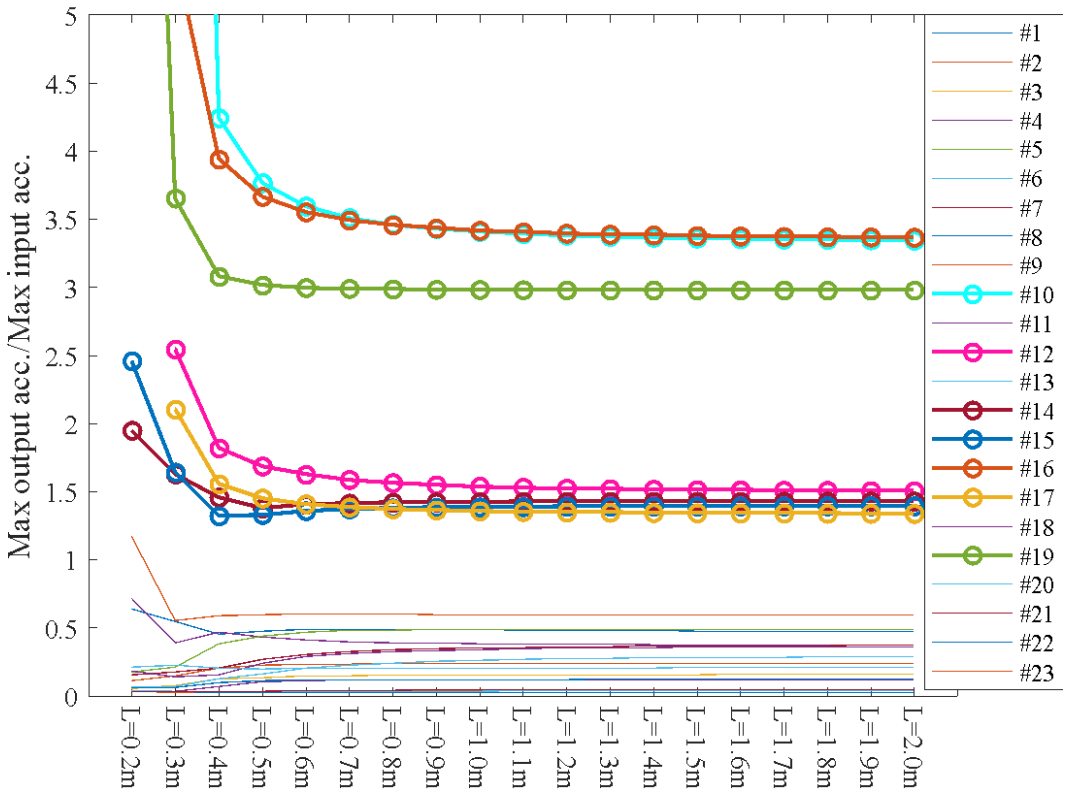

Figure 3.2. Maximum acceleration ratio of a QZSS with 5% damping without friction for various length of the arms

Having 0.6 m long arms or longer do not affect this criterion remarkably. As it was expected, the response is higher for Kobe, Northridge and the Chi-Chi earthquake because of containing low frequency contents which cause resonance in the system. The response of the system to the rest of the inputs remains lower than 1 for the system with 0.3 m or longer arms, although in some cases, by increasing the arm length, a slight increase can be observed. It is interesting to note that for almost all the earthquake inputs, there is not any major change in the maximum acceleration ratio for arms longer than 0.8 m. In other words, the system behaviour does not benefit from arms of longer length. This is because the ratio of the amplitude of the excitation to the length of the arms gets smaller and the variation as the angle decreases.

While Figure 3.2 shows the variation of the ratio of peak acceleration magnitudes, Figure 3.3 shows the RMS acceleration ratio for the same set of input signals. This figure indicates a similar trend as the maximum acceleration ratio graph for most of the input signals except for No. 14, which has more fluctuations. It is evident that for greater than 1m length arms, the RMS ratio remains almost unchanged for all of the signals.

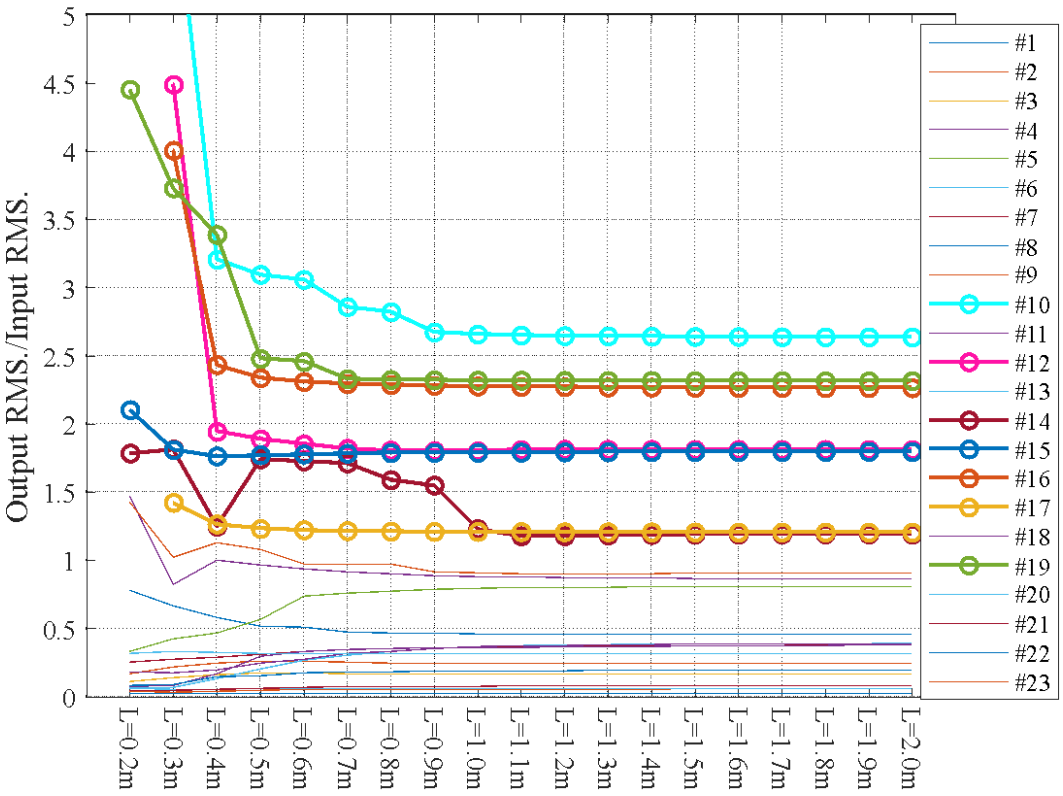

Figure 3.3. RMS acceleration ratio of a QZSS with 5% damping without friction for various length of the arms

As mentioned already, the length of the arms plays a significant role in the required space for the rig underneath the building. Therefore, shorter length would be preferable. In this case, 0.6 m appears to be a good compromise considering both the maximum acceleration ratio as well as the RMS acceleration ratio criteria. **Consequently, the writer suggests using <u>0.6 m</u> long arms for the isolator irrespective of any other design variables.**

3.3.2 Initial angle (θ_0)

The initial angle θ_0 is another design variable which is defined as the angle of the inclined arms with the horizontal axis in the unloaded state. As it was shown in the previous chapter, to have a QZSS with a natural frequency of 1 Hz, the relationship between l and θ_0 must satisfy $\theta_0 = \frac{g}{4\pi^2 l}$. Therefore, by knowing that the length of the arms is equal to 0.6 meters, the initial angle can be calculated as 24.4°. As illustrated in Figure 2.9 in the previous chapter, for a given length of the arms, 0.6 m, the initial angle of 24.4° or higher gives the natural frequency of 1 Hz or less respectively. Furthermore, all initial angles higher than 24.46° can be considered for a desirable QZSS for seismic purposes. In order to find the suitable initial angle, an analysis is done, and results are presented as follow. In this analysis, the damping coefficient is considered as 0.63 (for the damping term when $\omega_n = 2\pi$ and $\xi = 0.05$). This is to have only initial angle as a variable to be able to find the reasonable value. Friction is ignored in both horizontal and vertical directions.

Figure 3.4 shows the maximum acceleration ratio of a QZSS as a function of initial angles subjected to 23 earthquake inputs. As can be seen, the maximum acceleration ratio decreases by increasing the initial angle for most of the earthquake signals, while the reverse is true for

that of earthquake #15 and #17. For records #10, #12 and #16, there are some fluctuations. This fluctuation can be because of the frequency content of each earthquake signal which causes resonance in the system with these specific parameters. It is evident that there is no specific angle to minimize all the responses at the same time. However, $\theta_0 = 60^\circ$ gives a reasonable reduction in 19 cases except for #15, #16, #17 and #19. The response for these four earthquake inputs will be reduced using higher value for damping in the next section.

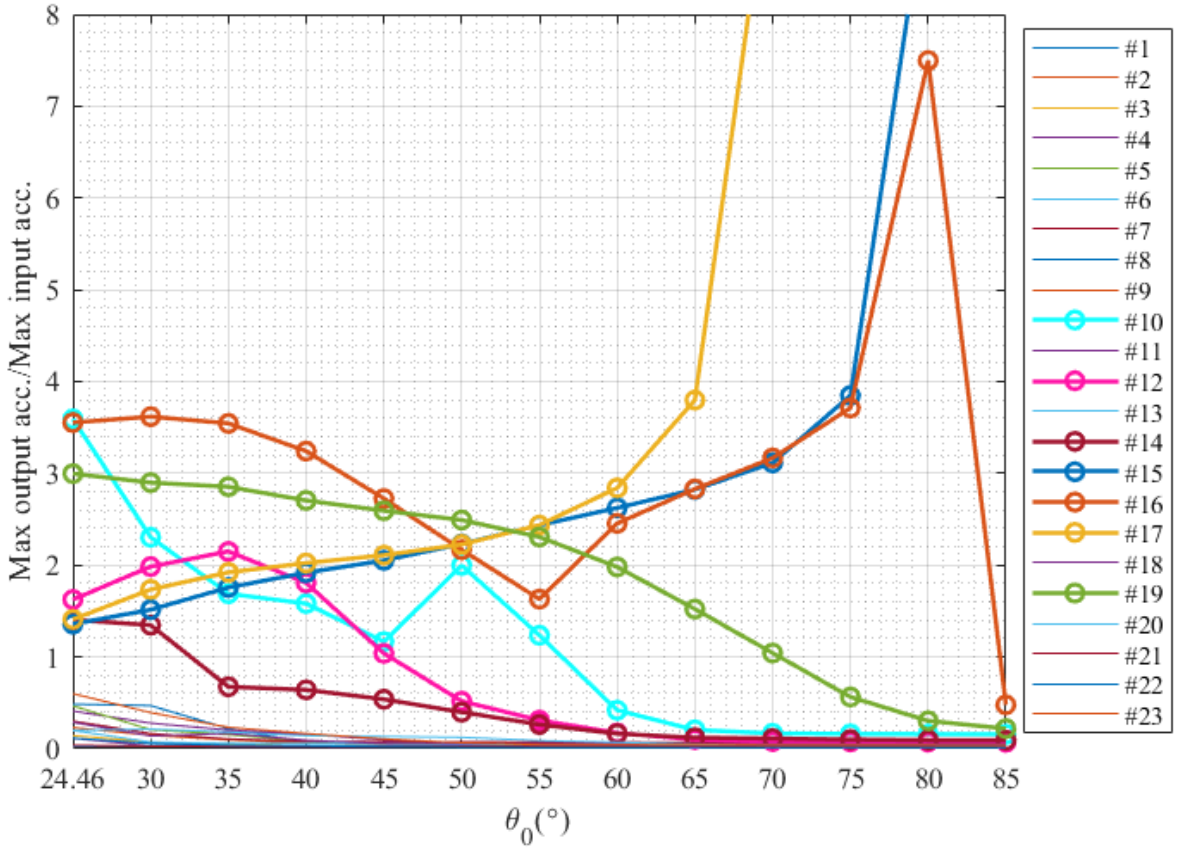

Figure 3.4. Maximum acceleration ratio of a QZSS with 0.6 m long arms, damping coefficient 0.63, without friction as a function of initial angle, θ_0

Considering the influence of initial angle in a slightly different way, Figure 3.5 indicates the variation of the RMS acceleration ratio with initial angle. It is evident that the trend is more or less similar to the maximum acceleration ratio. **Similarly, $\boldsymbol{\theta_0 = 60^\circ}$ can be suggested as an initial angle for designing the efficient isolator system which reduces the RMS acceleration ratio for most of the cases.**

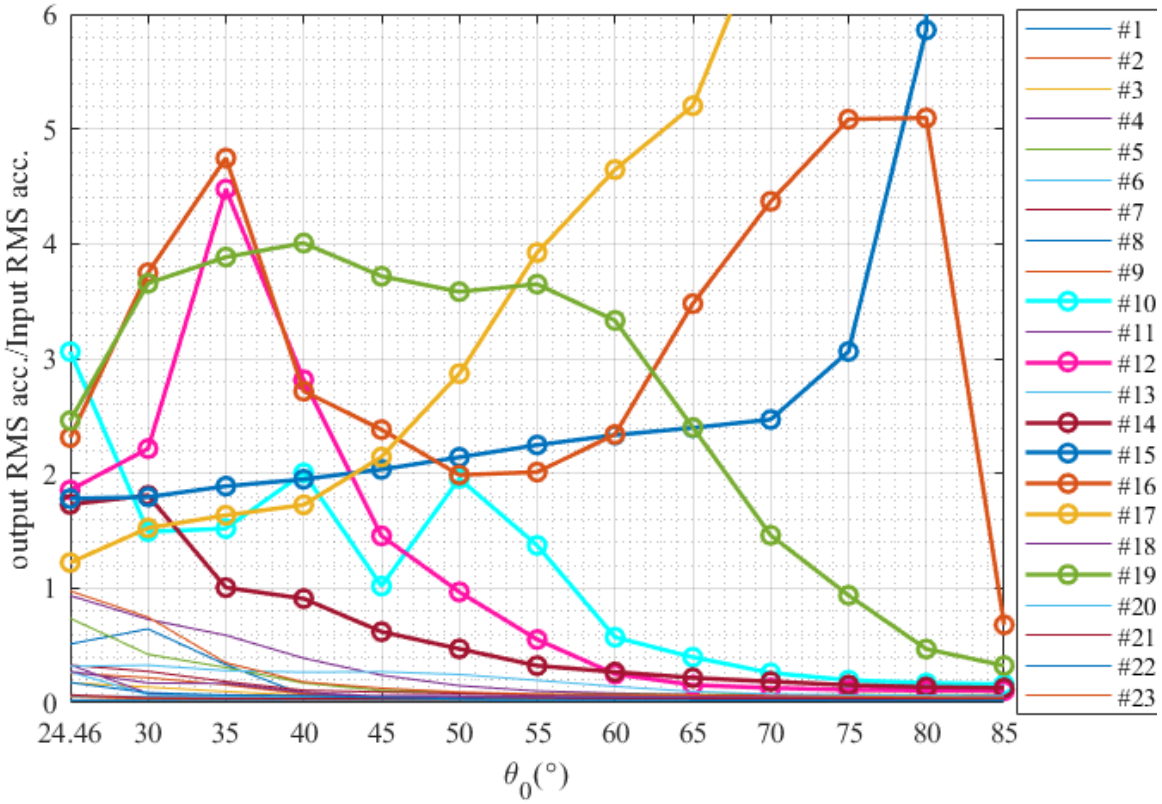

Figure 3.5. RMS acceleration ratio of a QZSS with 0.6 m long arms 5% damping without friction and various initial angles

3.3.3 Damping and friction ratios (ξ, η_h, η_v)

Having considered the two geometric design parameters that affect the stiffness of the system, the next set of variables to be considered are factors that give rise to energy dissipation. The damping and the friction ratios should be studied for this mechanism to see how the system behaves for different ratios. Damping ratios of 5 to 30% are considered for this mechanism and the results are shown in Figure 3.6, Figure 3.7, and Figure 3.8. The maximum acceleration ratio for various damping inputs is shown in Figure 3.6. Generally, by increasing the damping in the system, the maximum acceleration ratio increases slightly in most of the cases. This is true for those inputs with high frequency content (more than 1 Hz) which are well isolated by the mechanism and are the main focus of the design. This suggests that the damping ratio of 10% can reduce the maximum acceleration ratio for #15, #16, #17 and #19. Therefore, the maximum acceleration ratio is less than 1 for all input earthquakes with at least 50% reduction in peak acceleration for most of cases.

The effect of damping on the RMS acceleration ratio is shown in Figure 3.7. As can be seen, the RMS acceleration ratio graph follows similar trend as the maximum acceleration ratio for most of the cases. It seems to suggest that 10% damping ratio can control the response effectively. Although this ratio is amplified for #15 and #17 by 35%, there is a reduction for all other cases.

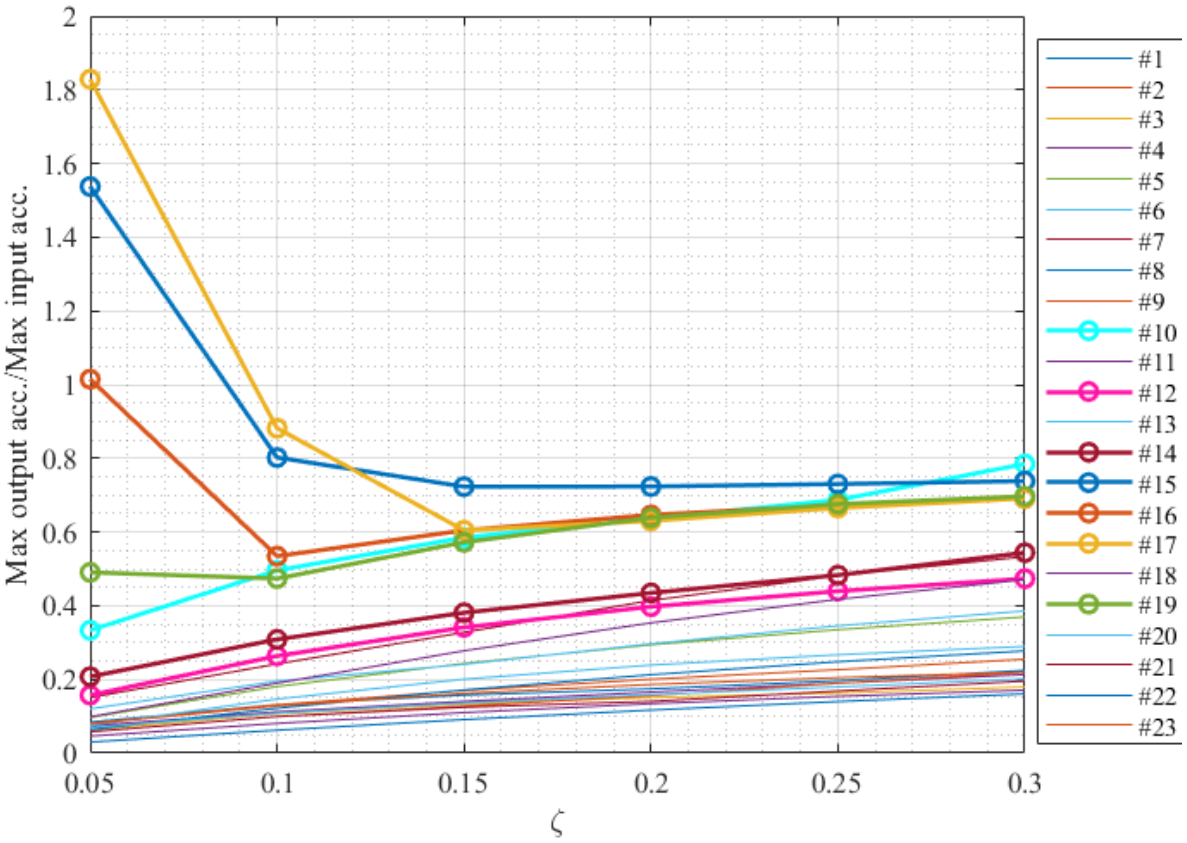

Figure 3.6. Maximum acceleration ratio of a QZSS with 0.6 m long arms, $\theta_0 = 60^\circ$ and various damping ratios without friction

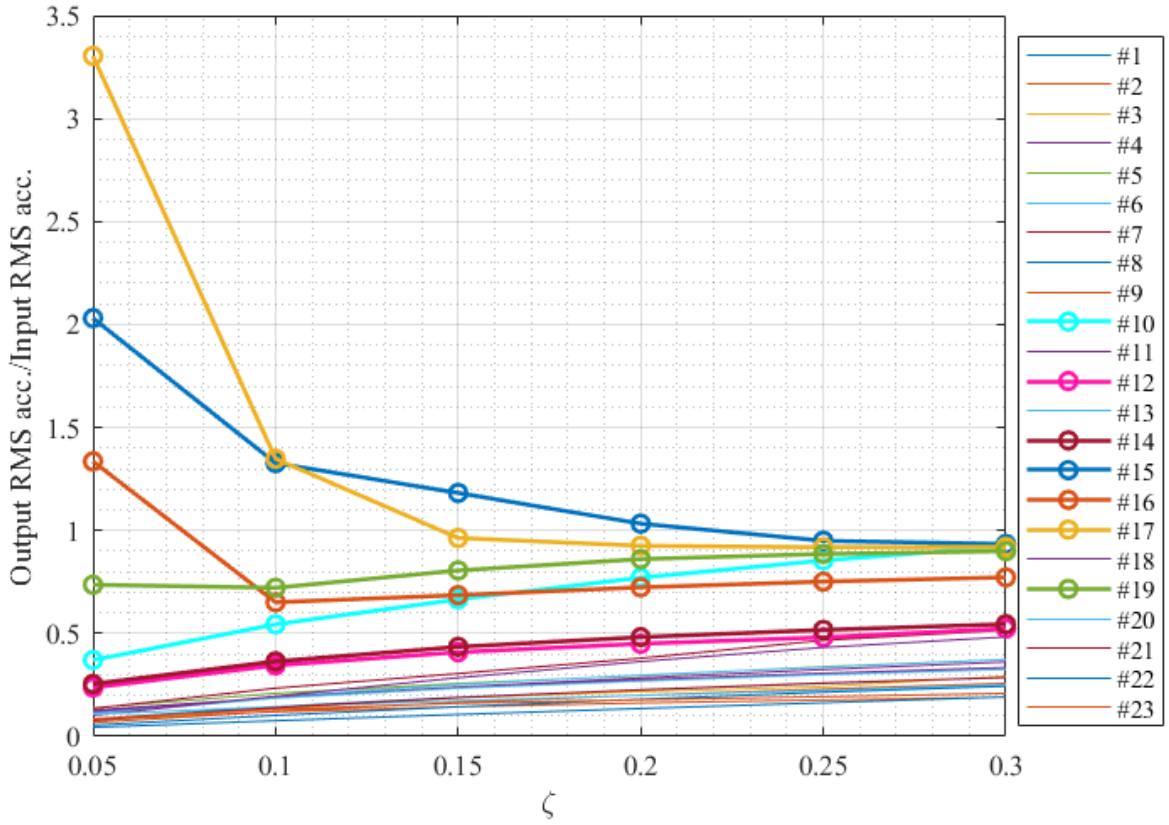

Figure 3.7. RMS acceleration ratio of a QZSS with 0.6 m long arms, $\theta_0 = 60^\circ$ and various damping ratios without friction

Figure 3.8 illustrates the maximum displacement ratio for various damping ratios. As is evident, by increasing damping ratio, the maximum displacement ratio increases for most of the cases except #16 and #19. 10% damping ratio can still be suggested for the system. In this case, the maximum displacement ratio for 21 out of 23 inputs will be 1 or less, although there is an amplification in two cases.

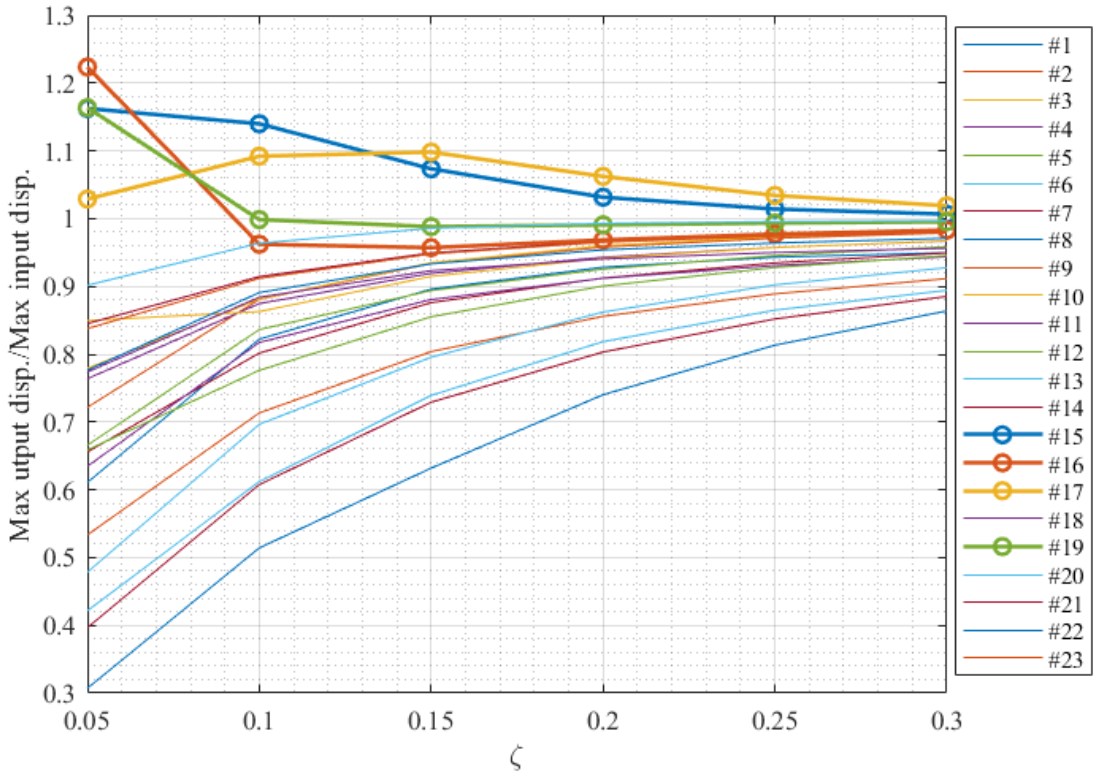

Figure 3.8. Maximum displacement ratio of a QZSS with 0.6 m long arms, $\theta_0 = 60^{\circ}$ and various damping ratios without friction

Having considered the effect of viscous damping, the effect of dry friction will now be discussed. The changes due to horizontal friction ratio are studied first. The variation of the maximum acceleration ratio of a QZSS with horizontal friction force ranging from 0-0.3 is shown in Figure 3.9. The graph shows that by increasing the nonlinear friction in the system the performance of the isolator decreases. For friction forces more than 0.1 *mg* the response of the system is around 1, which means the isolator does not work. Similarly, in Figure 3.10 the RMS acceleration ratio follows a similar trend. For friction forces equal or more than 0.05 *mg*, the RMS ratio increases significantly and the performance of the isolator decreases. Although that friction parameters are difficult to control in design, from the results it is clear that generally the nonlinear friction force reduces the performance of the isolator. Therefore, it is suggested to decrease this friction in the system as much as possible to improve the isolator performance.

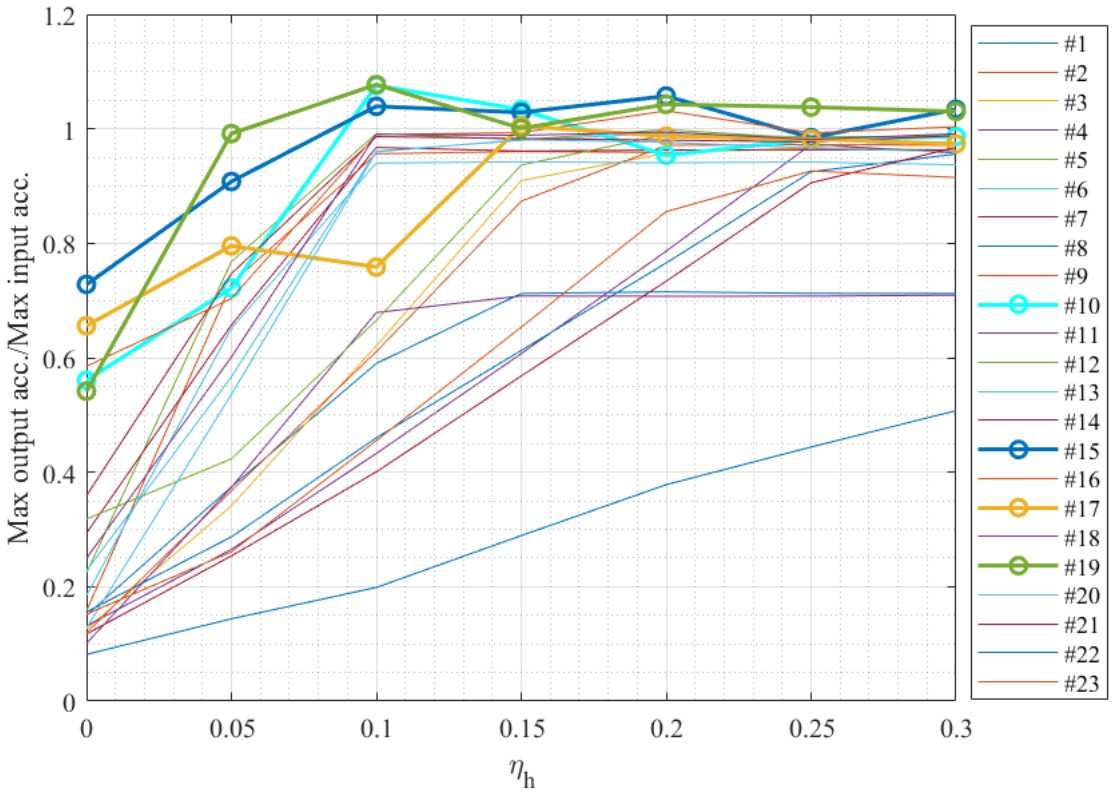

Figure 3.9. Maximum acceleration ratio of a QZSS with 0.6 m long arms, $\theta_0 = 60^\circ$, 10% damping ratio and various horizontal friction ratios

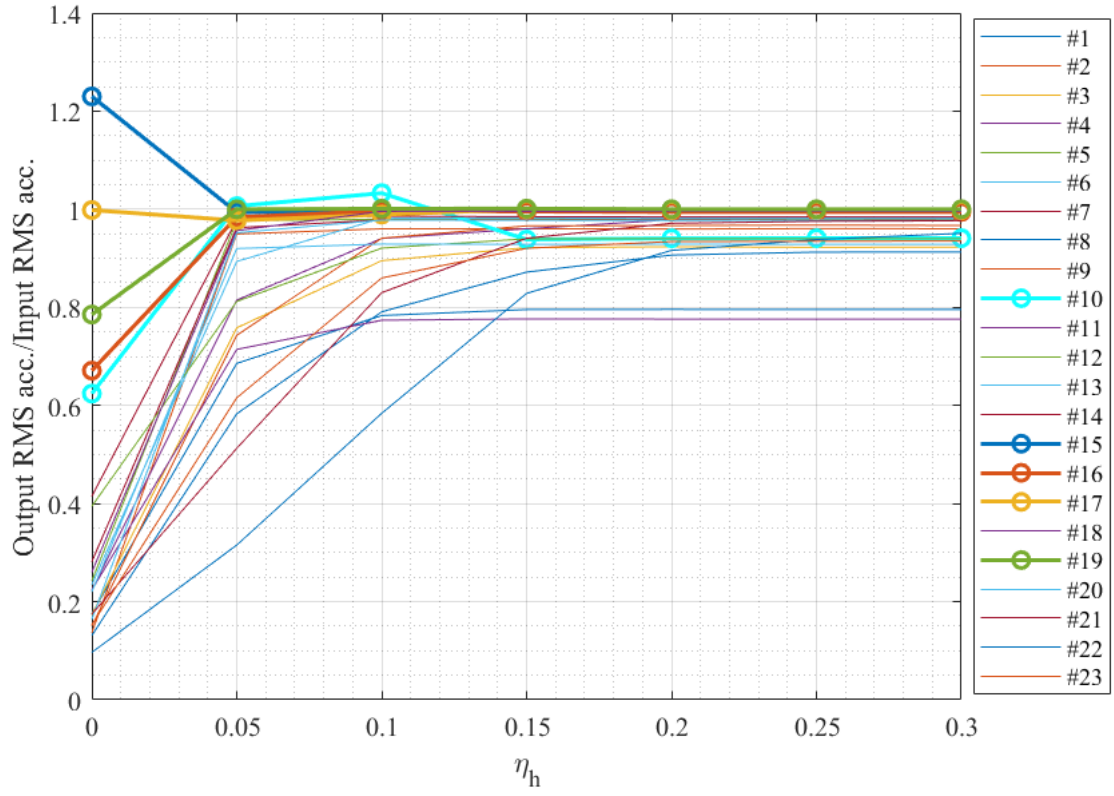

Figure 3.10. RMS acceleration ratio of a QZSS with 0.6 m long arms, $\theta_0 = 60^\circ$, 10% damping ratio and various horizontal friction ratios

While nonlinear friction reduces the performance of the isolator, the vertical friction in the system appears to reduce the effectiveness in the isolation system as well. When low, the linear friction decreases the maximum acceleration ratio for two inputs (#12 and #17), as shown in Figure 3.11. This can be because this friction can stop the mass from moving freely. However, it increases the response significantly for most cases. The effect of vertical friction is even more severe for the RMS acceleration ratio (Figure 3.12). However, the system may benefit from 5% friction.

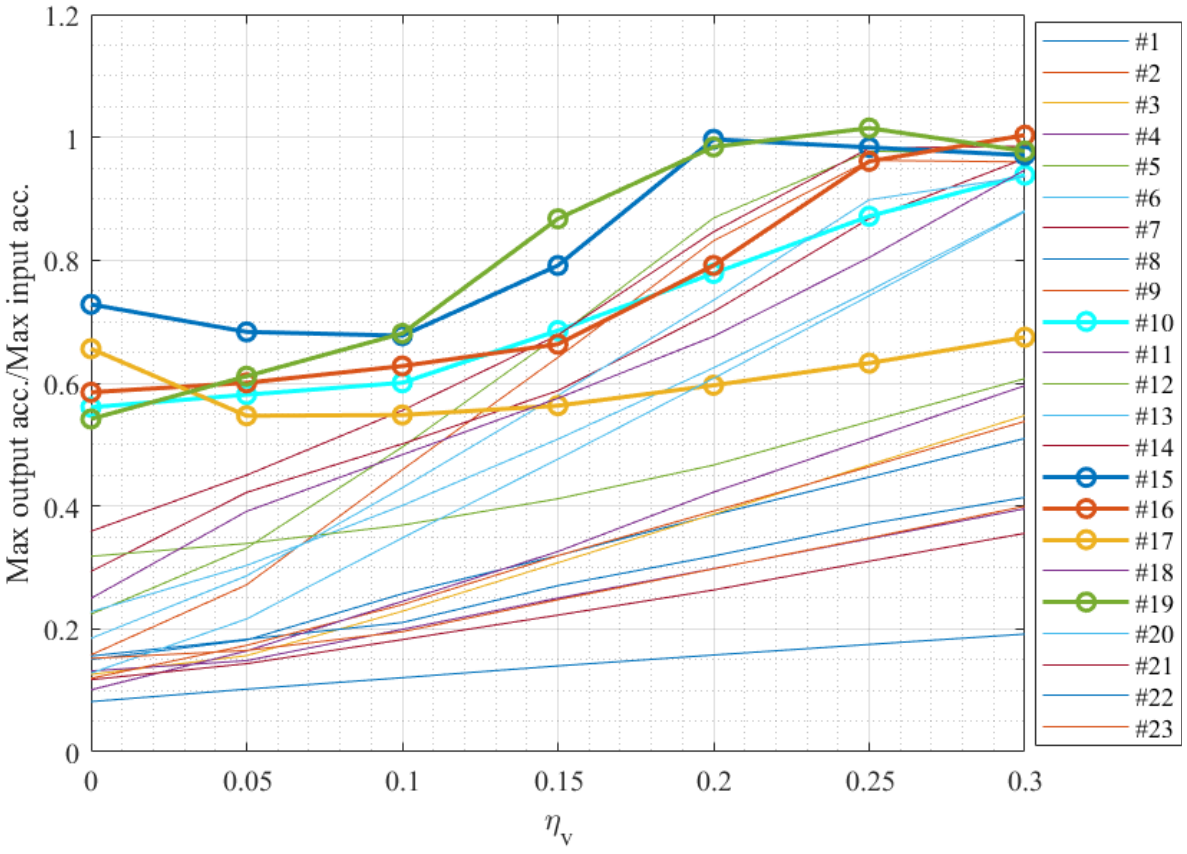

Figure 3.11. Maximum acceleration ratio of a QZSS with 0.6 m long arms, $\theta_0 = 60^\circ$, 10% damping ratio and various vertical friction ratios

Comparing linear and nonlinear friction effects of the system, the nonlinear friction force reduces the performance of the isolator much more than the linear one. Therefore, it is important to decrease this friction. The linear friction, however, can be allowed up to 5% of the weight of the system as the isolator retains good performance.

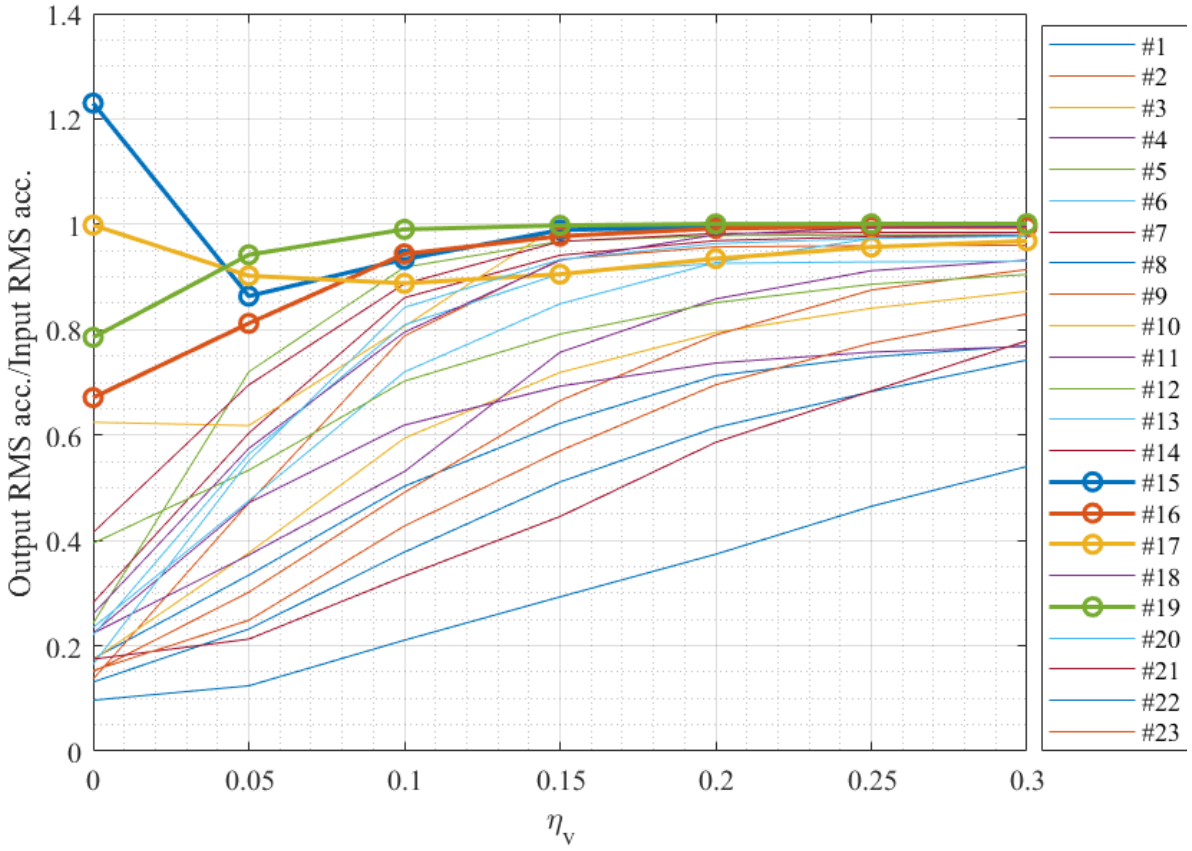

Figure 3.12. RMS acceleration ratio of a QZSS with 0.6 m long arms, $\theta_0 = 60^\circ$, 10% damping ratio and various vertical friction ratios

3.4 Comparison of non-QZSS and QZSS

3.4.1 Comparison linear system and QZSS

In this section, the behaviour of the QZSS is compared to a linear system with similar properties.

By ignoring the friction terms and substituting Eq. (2.19) into the Eq. (3.7), the equation of motion is rewritten as

$$\ddot{Y}' - \frac{2g\lambda}{l\sin\theta_0}\left(\sqrt{l^2 - Y'^2} - l\cos\theta_0\right) \times \frac{Y'}{\sqrt{l^2 - Y'^2}} + \frac{g}{l\sin\theta_0}Y' + 2\xi\sqrt{\frac{g}{l\sin\theta_0}}\dot{Y}' = -\ddot{z} \tag{3.9}$$

in which horizontal/vertical spring stiffness ratio, $\lambda = 1$ for a QZSS with initial angle $\theta_0 = 60°$ and $\lambda = 0$ for a linear system. In this section, the length of the arms $l = 0.6$ m and the damping ratio $\xi = 0.1$. As can be seen, this equation is dimensionless and independent of the payload. The objective is to find how the nonlinear properties affect the response of a SDoF system compared to a traditional linear spring isolator. The results are presented in the graphs and discussed.

Figure 3.13 shows the maximum acceleration ratio of a QZSS and a linear system. It is evident that the maximum acceleration ratio of the QZSS is less than the linear system in all the cases

and QZSS reduces the response by 27-93% for different inputs. However, there is an amplification in the response of the linear system subjected to earthquake input #19. In some cases, the difference between the response of the linear system and the QZSS is significant and clearly overall the QZSS behaves better than the linear one.

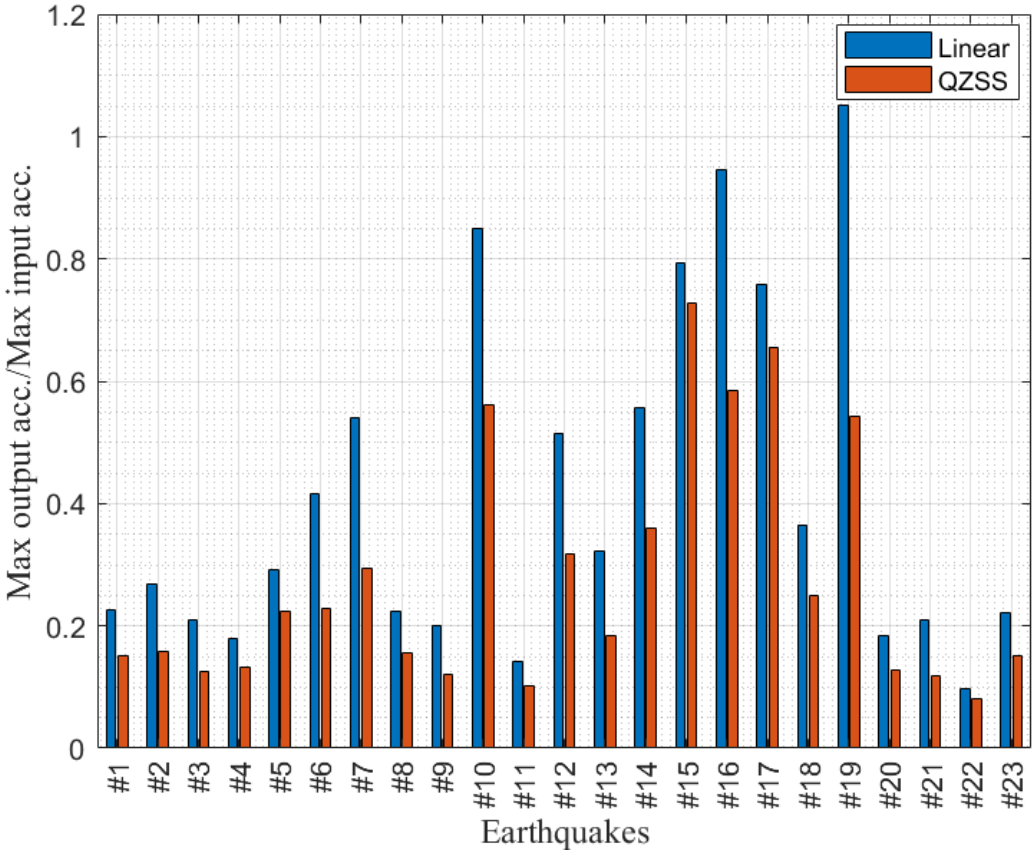

Figure 3.13. Comparison of maximum acceleration ratio of a linear system with a QZSS with 0.6 m long arms, $\theta_0 = 60^{\circ}$, 10% damping ratio without friction

Moreover, in Figure 3.14, the RMS acceleration for the linear and the nonlinear systems are compared. As shown, this ratio for the QZSS is less than the linear system except for input #15 for which the QZSS amplifies the response by about 20%. The linear system, however, amplifies the RMS acceleration of the response subjected to earthquakes #10, #15, #17, and #19.

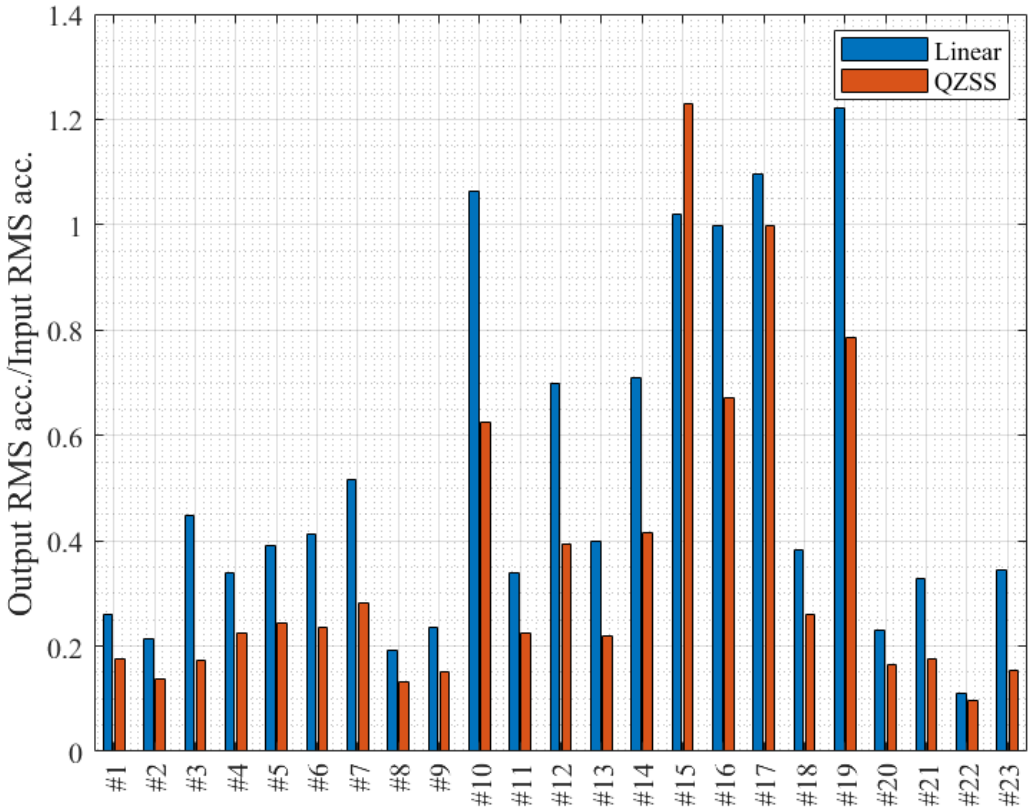

Figure 3.14. Comparison of RMS acceleration ratio of a linear system with a QZSS with 0.6 m long arms, $\theta_0 = 60^{\circ}$, 10% damping ratio without friction

The maximum displacement ratio for the QZSS is compared to that of the linear system in Figure 3.15. In most of the cases (except #15 and #17) this ratio is below 1 for QZSS and less than that of the linear system. Moreover, the linear system amplifies the maximum displacement of the system subjected to all earthquake inputs in this study.

The force amplification ratio of the QZSS is compared to that of the linear isolator system as well as a system without an isolator and the results are shown in Figure 3.16. As can be seen, both the QZSS and the linear system reduce the force amplification compared to the system without an isolator. This reduction is more in the QZSS, which shows a higher seismic performance of the QZSS compared to the linear isolator system.

Generally, the QZSS performed better than a linearly isolated system subjected to various near-fault vertical ground motions.

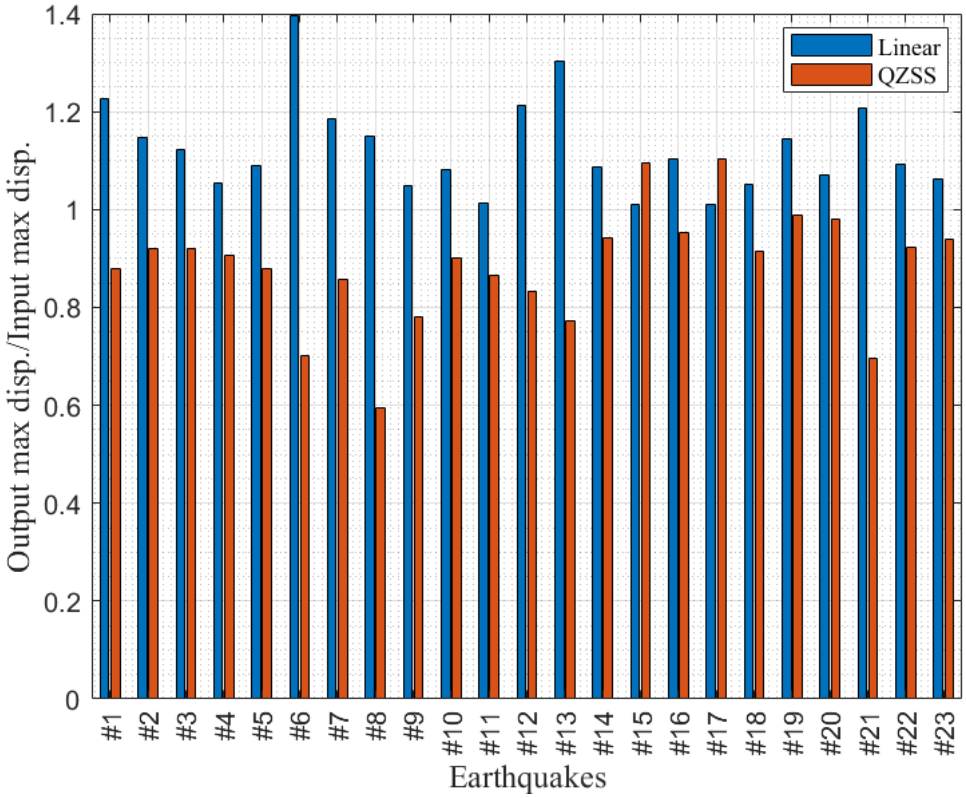

Figure 3.15. Comparison of maximum displacement ratio of a linear system with a QZSS with 0.6 m long arms, $\theta_0 = 60^{\circ}$, 10% damping ratio without friction

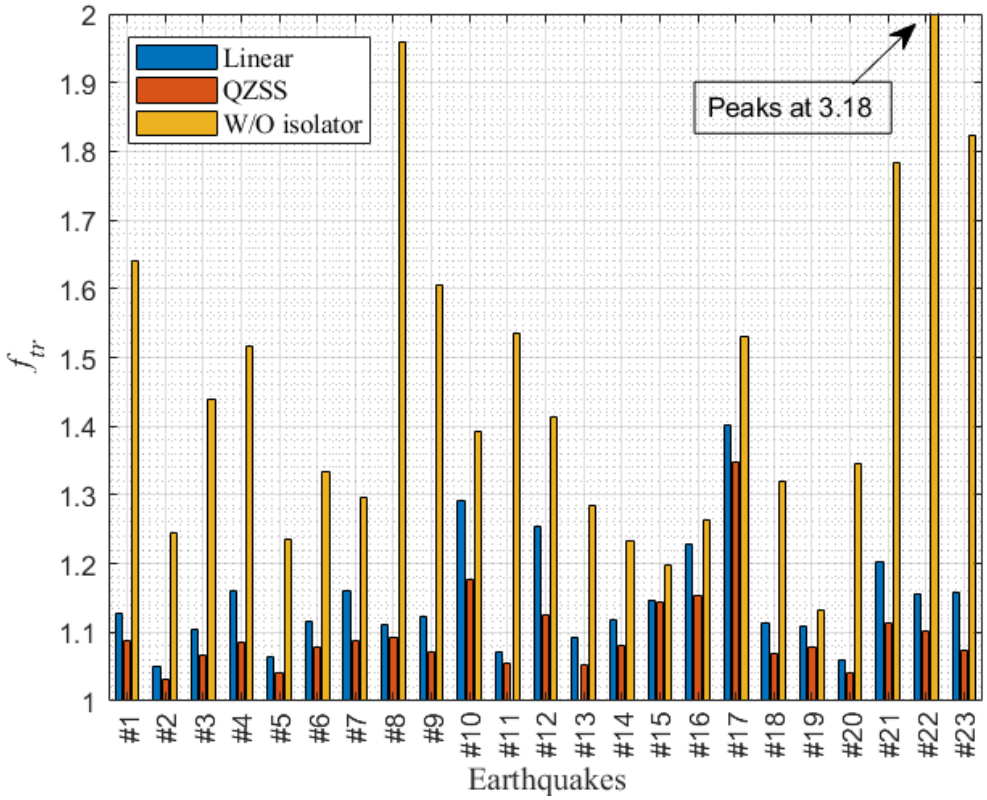

Figure 3.16. Comparison of force amplification of the linear system, QZSS with 0.6 m long arms, $\theta_0 = 60^{\circ}$, 10% damping ratio without friction and without isolator case

3.4.2 Comparison of HSLDSS and QZSS

In all studies to date, the QZSS with zero stiffness in the static equilibrium position is the device considered for isolation. It may not be a practical solution for the base of a building unless a lock-release system is used to avoid any unwanted displacements. Therefore, it is necessary to investigate the behaviour of a practical system, a HSLDSS with some positive stiffness in the equilibrium position for the design load. This system is also designed to have zero static angle in which arms are horizontal ($\theta_s = 0°$) in the static equilibrium position. As discussed in the previous chapter, the performance of a HSLDSS due to changes in the payload or mistuning is not affected as much as that of a QZSS. For this purpose, the QZSS with 0.6 m long arms and 60° initial angle is considered and compared to the HSLDSS. Using Eq. (2.19) in chapter 2, the ratio of the horizontal spring stiffness to the vertical one in QZSS with initial angle of 60°, $\lambda_{QZS_{60}} = 1$.

For a HSLDSS, the ratio of the horizontal spring stiffness in a HSLDSS to that of QZSS is defined as

$$\beta = \frac{k_h}{k_{h,QZS}} \tag{3.10}$$

in which β can take any value between 0 (linear system) and 1 (QZSS). If $\beta > 1$, the system is unstable at $\theta = 0$, which needs to be avoided.

In this section, the seismic performance of the HSLDSS with $\beta = 0.2, 0.4, 0.6,$ and 0.8 (as examples) is compared to that of the QZSS ($\beta = 1$). Figure 3.17 shows the static behaviour of the HSLDSS with different values for β compared to a QZSS. As can be seen, the nonlinearity of the system increases for a higher value of β. The equivalent stiffness of the system (slope of the curve) at the static equilibrium position, $\hat{Y} = 0$, is zero for the QZSS and takes a positive value for the HSLDSS.

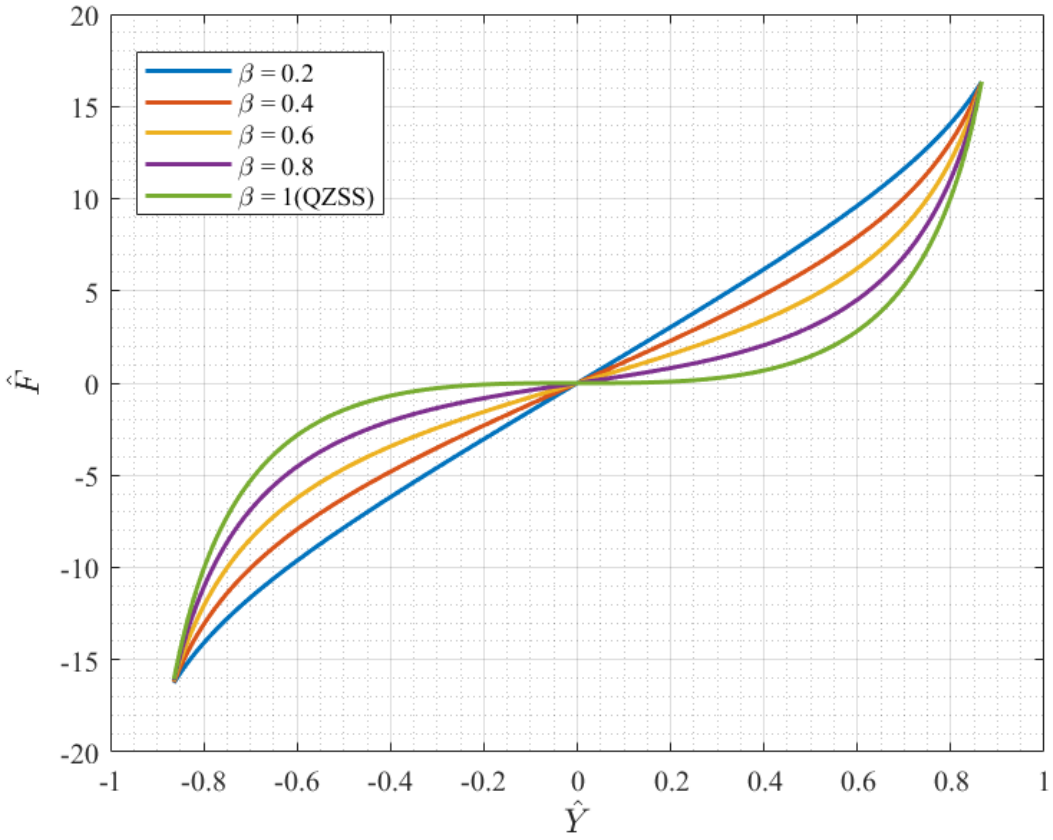

Figure 3.17. Static behaviour of the HSLDSS for various values of β in comparison with a QZSS with 0.6 m long arms and $\theta_0 = 60°$.

By replacing λ with β (since $\lambda_{QZS_{60}} = 1$) in Eq. (3.9), the equation of motion is rewritten as

$$\ddot{Y}' - \frac{2g\beta}{l\sin\theta_0}\left(\sqrt{l^2 - Y'^2} - l\cos\theta_0\right) \times \frac{Y'}{\sqrt{l^2 - Y'^2}} + \frac{g}{l\sin\theta_0}Y' + 2\xi\sqrt{\frac{g}{l\sin\theta_0}}\dot{Y}' = -\ddot{z}. \tag{3.11}$$

Figure 3.18 shows the maximum acceleration ratio of the HSLDSS for various values of β in comparison to a QZSS. As is evident, by increasing β, the maximum acceleration ratio decreases for most cases except for #15 and #17 which have fluctuations. Therefore, the closer β is to 1 (QZSS), the higher performance the isolator will have. Therefore, $\beta = 0.8$ can be suggested for a HSLDSS.

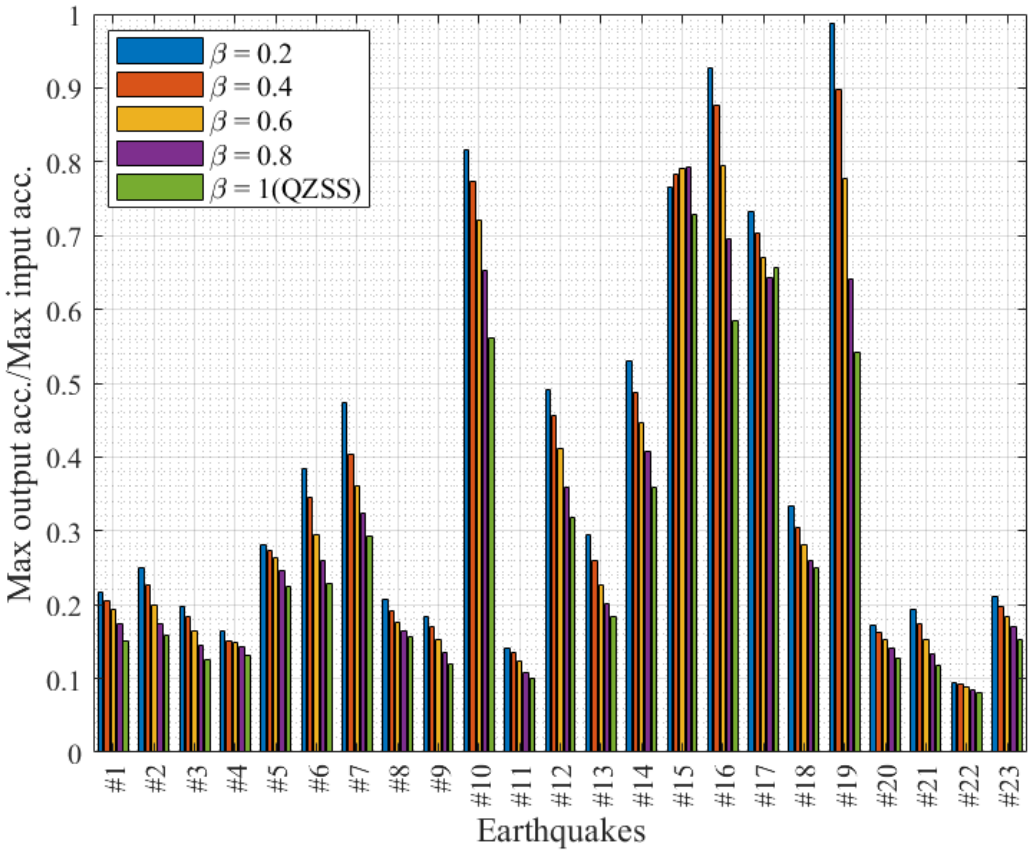

Figure 3.18. Maximum acceleration ratio for HSLDSS with various values of β in comparison to a QZSS with 0.6 m long arms, $\theta_0 = 60°$, and the damping ratio of 10%

The RMS acceleration ratio, on the other hand, decreases by increasing β in most cases except for input #15, which has an opposite trend (Figure 3.19). Considering $\beta = 0.8$ as a suggested ratio for the horizontal spring stiffness, the RMS ratio is below 1 in all cases except #15 and #17. In other words, this HSLDSS retains the performance of the isolator with a reduction in RMS acceleration ratio between 20-90% in most cases.

Figure 3.20 shows the maximum displacement ratio of the HSLDSS for various values of β in comparison to a QZSS. As can be seen, the maximum displacement ratio of the HSLDSS is generally higher than the QZSS in most cases except #15 and #17. For the suggested case $\beta = 0.8$, also, this ratio is above 1 for 18 cases but below 1.15 for all cases. Which means that the HSLDSS may not be suitable for displacement sensitive equipment and structures.

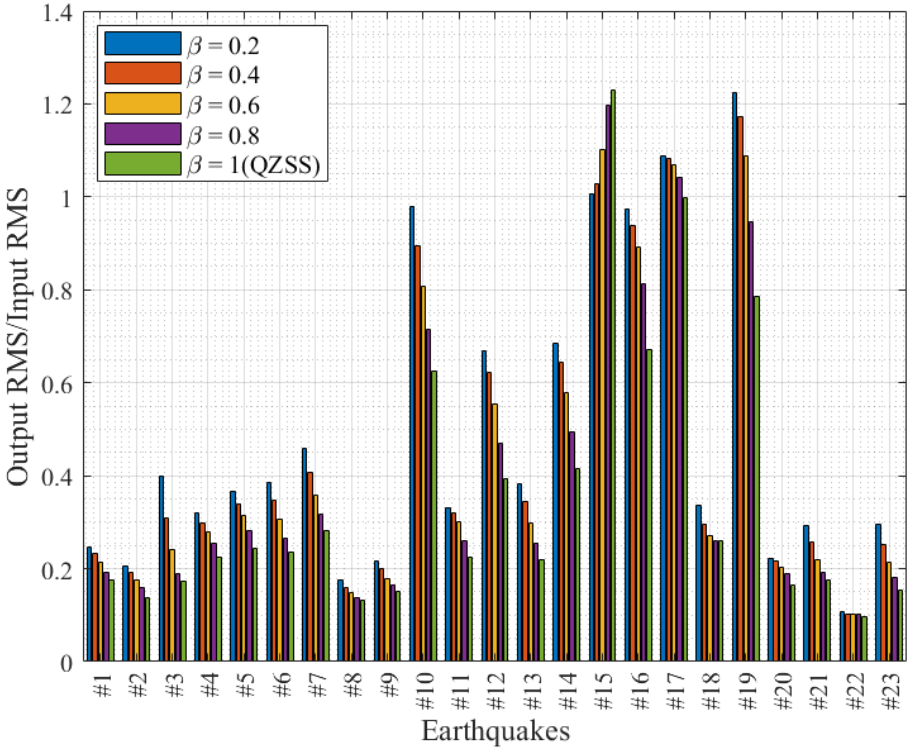

Figure 3.19. RMS acceleration ratio for HSLDSS with various values of β in comparison to a QZSS with 0.6 m long arms, $\theta_0 = 60°$, and the damping ratio of 10%

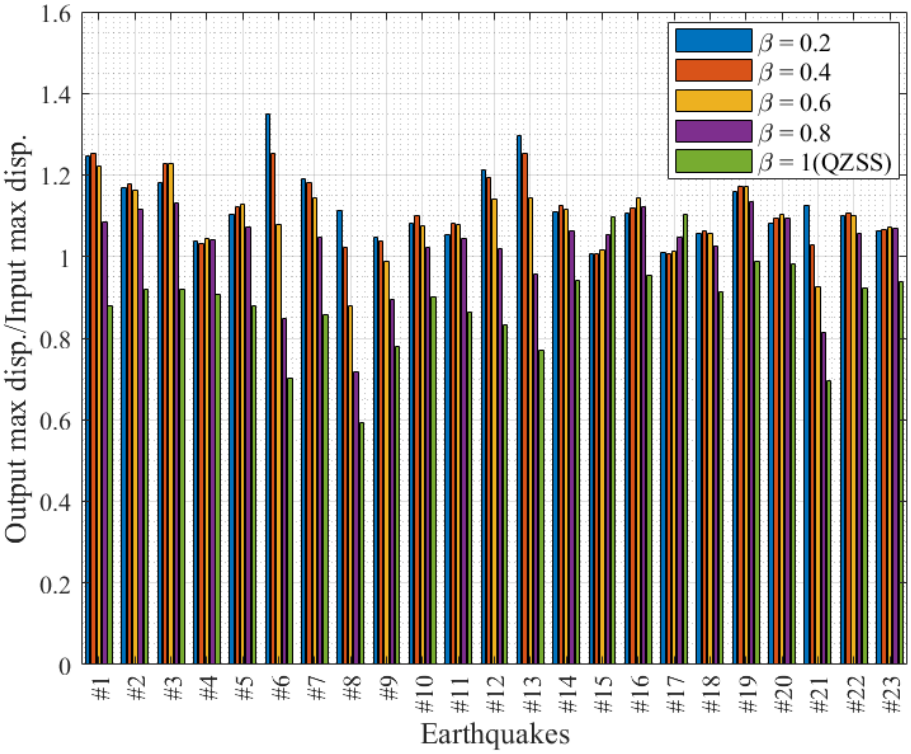

Figure 3.20. Maximum displacement ratio for HSLDSS with various values of β in comparison to a QZSS with 0.6 m long arms, $\theta_0 = 60°$, and the damping ratio of 10%

Figure 3.21 shows the force amplification for the HSLDSS and the QZSS subjected to different ground excitations. As evident, both HSLDSS and QZSS reduce the compressive force transmitted to the mass significantly in all cases. As shown, except for #10, #15 and #17, the force amplification decreases by increasing the nonlinearity in the system, which shows that the QZSS has the highest isolation performance compared to the HSLDSS, although the difference is not significant. For the system with $\beta = 0.8$, this ratio is very close to that of the QZSS and can be a reasonable alternative.

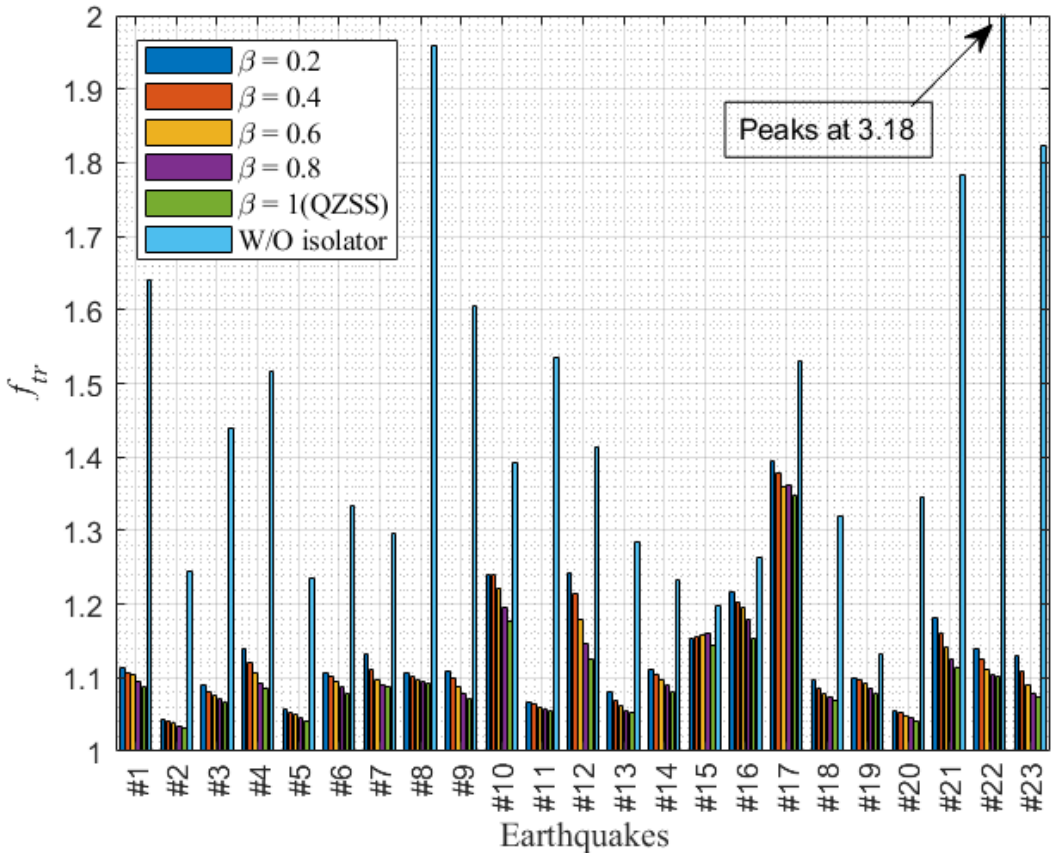

Figure 3.21. Force amplification for HSLDSS with various values of β in comparison to a QZSS with 0.6 m long arms, $\theta_0 = 60°$, and the damping ratio of 10%

3.5 Conclusion

In this chapter, the selection of 23 near-fault earthquake ground motions were used to design the parameters of a QZSS for vertical seismic isolation of a building. Based on the assumptions and analysis, 0.6 m long arms with a 60° initial angle to the horizontal and 10% damping ratio were suggested. The linear and nonlinear friction effects (in the horizontal and vertical directions) were also studied. The results showed that the nonlinear friction negatively affects the performance of the isolator more severely than the linear one. Therefore, friction in the system must be minimal to get the maximum seismic isolation.

Moreover, the dynamic response of the designed QZSS with 10% damping without friction force was compared to a linear system with similar properties. Based on the results, it was shown that the QZSS was more effective than the linear one. Besides, the QZSS with horizontal springs can be adjusted to provide a desirable configuration, while this is not an option in a linear system.

Finally, other options for the HSLDSS were studied and compared to a QZSS. Since a QZSS has ideally zero stiffness in the static equilibrium position, it may cause some unwanted static displacements. Therefore, a lock-release system could be used. Alternatively, the system should have some positive stiffness, a so-called HSLDSS, to resist changes in payload or mistuning while it retains its performance subjected to earthquakes. The horizontal spring stiffness ratio of 0.8 and $\lambda_{QZS_{60}}$ gave good acceleration reduction while it decreased the force amplification.

3.6 References

[1] *PEER-NGA ground motion database*. from https://ngawest2.berkeley.edu/.

[2] Bozorgnia, Y., & Campbell, K. W. (2016). Ground motion model for the vertical-to-horizontal (V/H) ratios of PGA, PGV, and response spectra. *Earthquake Spectra, 32*(2), 951-978.

[3] Kalkan, E., & Chopra, A. K. (2010). *Practical guidelines to select and scale earthquake records for nonlinear response history analysis of structures.* Earthquake Engineering Research Institute.

[4] Li, X., Dou, H., & Zhu, X. (2007). Engineering characteristics of near-fault vertical ground motions and their effect on the seismic response of bridges. *Earthquake Engineering and Engineering Vibration, 6*(4), 345-350.

[5] Bradley B., A ground motion selection algorithm based on the generalized conditional intensity measure approach, *Soil Dynamics and Earthquake Engineering, 40, 48-61.*

[6] Salmon, M. W., Short, S. A., & Kennedy, R. P. (1992). *Strong motion duration and earthquake magnitude relationships*.

[7] Trifunac, M. D., & Brady, A. G. (1976). *A study on the duration of strong earthquake ground motion*. Pasadena, California: Earthquake Engineering Research Laboratory, California Institute of Technology.

Chapter 4.

Experimental model

4.1 Introduction

In the previous chapters, the numerical model for the mechanism to predict the behaviour of the system subjected to both the harmonic and the earthquake excitation was developed.

In this chapter, the physical model of the experimental rig is described. The equipment used for static and dynamic testing of the rig are presented. The type of tests and the techniques of measurements and calculation of different parameters such as spring stiffness, static behaviour of the rig, and friction force are also explained.

In the next chapter, the experimental results are presented and compared to the analytical and numerical results to validate the numerical modelling and for further discussion.

4.2 Rig description

The physical model was designed and made based on various factors. First and foremost, the capacity of the shaker is considered to be the main factor to design the rig. The purpose of the experiments was to understand the behaviour of the system under earthquake excitations and excitations with as large displacement amplitudes as possible. Therefore, the size of the rig should be suitable for the shaker capacity in order to excite it in the desirable range of displacement and frequency.

Figure 4.1 illustrates the rig. The arms (A) were made in two lengths, 50 mm and 100 mm. To take account of mass of the arms which is assume to be rigid, half the mass of each arm added to the payload. The actual effect of the mass (inertia) of the arms would change depending on angle of orientation. However, knowing that the mass of the arms is within the uncertainty of the mass already considered in the analysis (section 2.6.2), it was decided not to perform the exact analysis. The holes in the horizontal (B) and the vertical (C) shafts were made to adjust the stiffness of the springs (by changing the number of the active coils). The horizontal shafts are supported by two linear ball-bearings (D), inlaid in the housing in the side frames to reduce the friction between the surfaces. The carriage (or platform E) is made of plastic slides on the vertical shaft. The top frame (F) and arms are made of aluminium (to decrease the weight), while the rest of the parts are from stainless steel. The exact measurements for each part are provided in Appendix A.

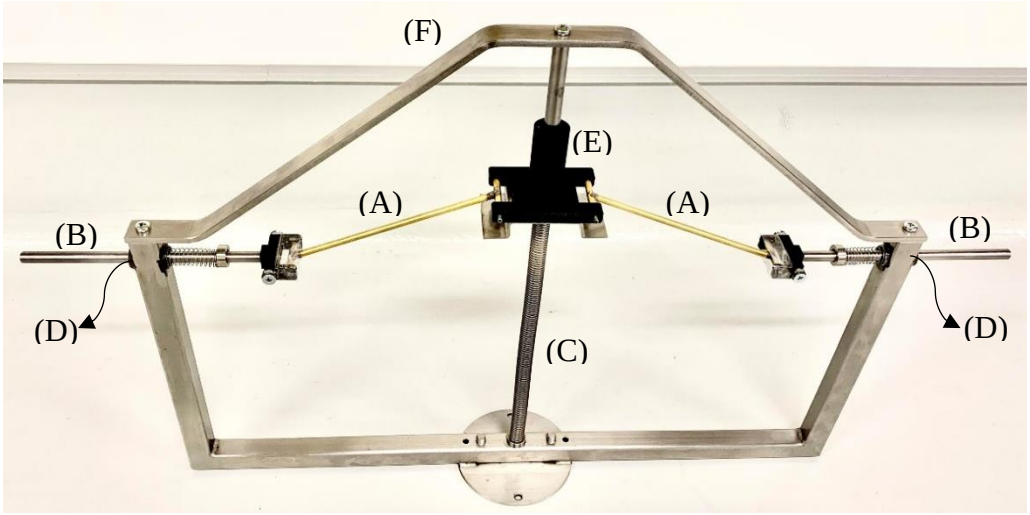

Figure 4.1. The rig

4.3 Equipment description

4.3.1 Static testing system

The static testing was intended to find an accurate static behaviour of the rig as well as measure the stiffness of the springs. For this purpose, an Instron 5900 series 100 kN machine was used, shown in Figure 4.2. The capacity of this system was 100kN. A picture of the static test on the rig is shown in Figure 4.3.

Figure 4.2. Instron 100kN tester – 5900 series

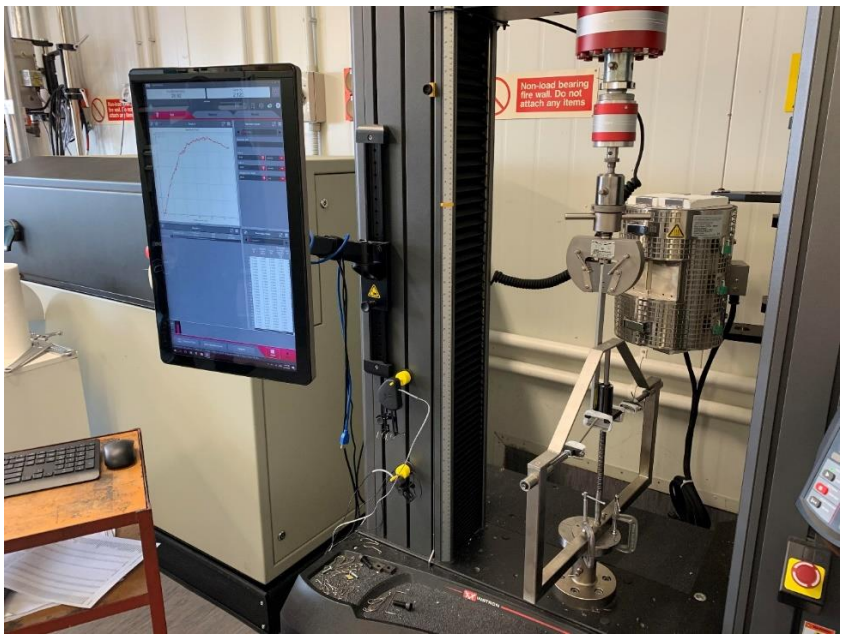

Figure 4.3. Static test on the rig

4.3.2 Dynamic tests

- Shaker

APS 113 Electro-series shaker is used to excite the rig (Figure 4.4). This shaker has a large stroke and is suitable for the large displacement excitation and is able to model most of earthquake signals without any filtering required. The general specification of this shaker can be found in Appendix B. The rig on the shaker is shown in Figure 4.5.

Figure 4.4. Vertical shaker: APS 113 with APS 0077 series

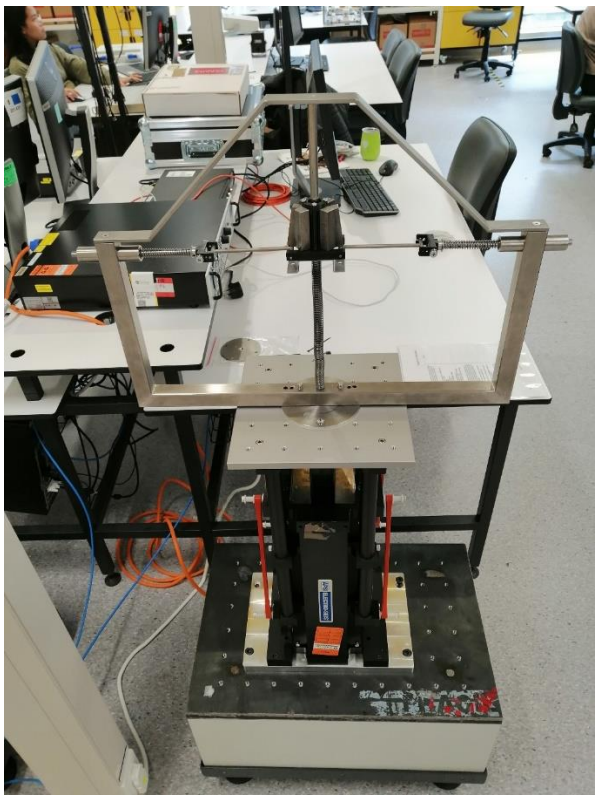

Figure 4.5. The rig on the shaker

- Controller

The “Vibration Research” controller is employed to create the sine sweep signals as well as earthquake excitations and control the vibration.

- Sensors

The results were measured by accelerometers with 200 mv/g sensitivity DYTRAN – 7500 A3 (the figure is given in Appendix B). As the accelerometers were being used for the measurements, the input and output signals were based on acceleration. For the earthquake excitation, also, the acceleration inputs were used. The tests were based on closed loop acceleration controls.

4.4 Design variables

The tests were conducted for various values of the following design variables:

- Length of the bars

Two different length were used for the tests, 100 mm and 50 mm.

- Initial angle

The initial angle of the arms was chosen in order to bring the arms to horizontal in the static equilibrium position. Based on chosen load and spring stiffness, the initial angle was calculated around 30 degrees.

- Horizontal spring

The stiffness range of the horizontal springs are: 200-300 N/m.

- Vertical spring

The changes were made in the vertical spring by putting a pin and changing the number of active coils in the spring. The spring stiffnesses were in the range 100 - 200 N/m. Mistuning was made by pushing the end of the vertical spring up or down by 10% (1 cm for the system with 10cm arms) which also changed the initial angle.

- Payload

The mas used was 0.7085 kg and slight changes (less than 10%) in the payload were also applied to observe the change in the dynamic behaviour of the system.

4.5 Description of tests

Various tests were done on the mechanism to validate the numerical results with the real case including static, pure sinusoidal, sweep sinusoidal and earthquake tests.

4.5.1 Static tests

The static tests were done with 20 mm/min displacement rate (which was found to be sufficient to get consistent readings) and the force was measured. The stiffness of the springs as well as the static behaviour of the mechanism were measured with compression loading tests. The load applied was in the range 0 – 10 N.

4.5.2 Sweep sinusoidal tests

This type of test was reasonably quick and gave the transmissibility curve for the mechanism as well as the resonance frequency and the general behaviour. The tests were carried out by increasing the frequency from 0.7 Hz to 3 Hz for sweep up and decreasing from 3 Hz to 0.7 Hz for sweep down. The computer software calculates the real-time transmissibility based on the maximum response it receives from the sensor divided by the maximum excitation amplitude.

4.5.3 Pure sinusoidal tests

To get an accurate transmissibility curve around the resonance frequency, the sine sweep was not satisfactory, because to get a reliable data, the mechanism must be excited long enough by being subjected to a specific harmonic excitation. Therefore, the pure sinusoidal tests were done for each frequency inputs to plot the transmissibility curve around the resonance. It is also interesting to note that in order to capture some data, the tests must run from low to high frequencies and for some other, the reverse was true. The reason was because there were three possible response for the same frequency. Therefore, the initial conditions affected the mechanism to pick any of those three types of response, of which two are stable. Although the tests were done a few times, the middle branch was not been captured. It is because the middle response is unstable and the mechanism cannot stay long enough in that response. As a result, it jumped up (in sweep down tests) or down (in sweep up test) to the other possible responses.

4.5.4 Earthquake tests

To evaluate the dynamic behaviour of the isolator under earthquake excitations, 7 earthquake ground motions were chosen (Table 4-1). The vertical acceleration time histories of the earthquake ground motions were used as inputs. The reason was that the controller could produce the signals as acceleration and the sensors were accelerometers. Therefore, the

controller was getting an acceleration feedback from the shake table and comparing it with demand acceleration which led to more accurate results. Using a displacement time history input could not converge to the demand. This was because the measured data from accelerometer was in terms of acceleration and it required double integration to calculate the displacement and compared to the demand. This was also true for the velocity input.

On the other hand, the capacity of the shake-table was limited, Bam, Christchurch, and LGPC earthquake signals required some scaling. For Christchurch earthquake, three different scaling were considered to study the effect of intensity on the performance of the system. For this purpose, the acceleration amplitude was scaled for the mentioned signals. Besides, the main purpose of the experiments was to prove the concept and validate the numerical model, therefore, this simple scaling satisfied the needs. The scale factor values for each earthquake signals are shown in Table 4-1.

Table 4-1. Earthquake input list series

Earthquake	**Station**	**Scale factor**
Bam	Bam	0.5
Christchurch	Heathcote Valley Primary School	0.2, 0.3, 0.4
Chi-Chi, Taiwan	TCU084	1
Imperial Valley	EC Meloland Overpass FF	1
Imperial Valley	El Centro Array #7	1
Erzincan, Turkey	Erzincan	1
Loma Prieta	LGPC	0.5
Northridge	Sylmar - Converter Sta	1

4.6 Friction force measurement and calculation

Friction force is a complicated phenomenon which is very difficult to measure but modelling shows it has a noticeable effect on the response. In this study, three types of test have been done to measure the friction force: static test, sweep sinusoidal test, and earthquake tests.

4.6.1 Static tests

In order to measure the friction force in the mechanism, the loading-unloading tests were done. The difference between the loading forces and unloading forces gave twice the friction force for each displacement. The average value was considered as the friction force in the system.

4.6.2 Sweep sinusoidal tests

The second method used to calculate the friction force was the sweep sinusoidal test. In this method, the frequency (ω_{slip}) at which the mass slipped and started to move was detected. The acceleration of the mass when it overcomes the friction force and slips is defined by

$$a_{slip} = A\omega_{slip}^2 \ , \tag{4.1}$$

in which A is the amplitude of the excitation (displacement input) and ω_{slip} is the frequency where the slip happens. Therefore, the friction force is given by Newton's second law as

$$friction\ force = m.a_{slip}\ . \tag{4.2}$$

The friction force is calculated for different displacement amplitudes.

4.6.3 Earthquake tests

The friction force was also calculated using the least square of error method based on results from earthquake responses. In this method, the numerical response for each earthquake input was generated using various friction forces. Then the difference between each numerical and experimental acceleration response time histories gave the error. The sum of squared errors gives a parameter to optimize and finds the friction force which gives the least error. This is to be done for eight earthquake inputs. As different earthquake input gives different friction force, the RMS of these friction forces was considered for the numerical model. This estimation of the friction force appears to be the best one as it gives better agreement between numerical and experimental results for both transmissibility and earthquake tests.

4.7 Conclusion

In this chapter, the equipment which was used for measuring static and dynamic behaviour of the system was presented. The techniques of measuring and calculating the parameters of the system were also described as well as the tests which were done. Three techniques were employed to calculate the friction force using static test, Sweep sinusoidal test and earthquake test. The friction force calculated from earthquake tests gave a better agreement for the numerical modelling.

Chapter 5.

Experimental results and discussion

5.1 Introduction

In the previous chapter, the equipment used for the static and dynamic tests were described. The techniques and process of measuring were also explained.

In this chapter, the experimental results are presented and compared to numerical results to validate the model and discuss the behaviour, performance, and sensitivity of the system to mistuning (changes in the location of the arms) and changes in the payload. These results include static tests, time harmonic tests and earthquake tests.

In the next chapter, the conclusion of the whole thesis will be provided.

5.2 Static tests

As mentioned in the previous chapter, the static tests were performed using an Instron machine, which is an accurate measuring equipment. In this section, the results from static tests to determine the stiffnesses of the vertical and horizontal springs, the static force-displacement relationship for the mechanism, and the friction force are provided.

5.2.1 Spring stiffness measurements

The compression tests were carried out to measure the stiffness of the springs. Figure 5.1 illustrates the force-displacement graph for the horizontal and vertical springs for one of the specimens with 10 cm long arms. By fitting a straight line to the data, the slope gives the stiffness of the springs as 280.3 N/m for the horizontal and 139.8 N/m for the vertical springs.

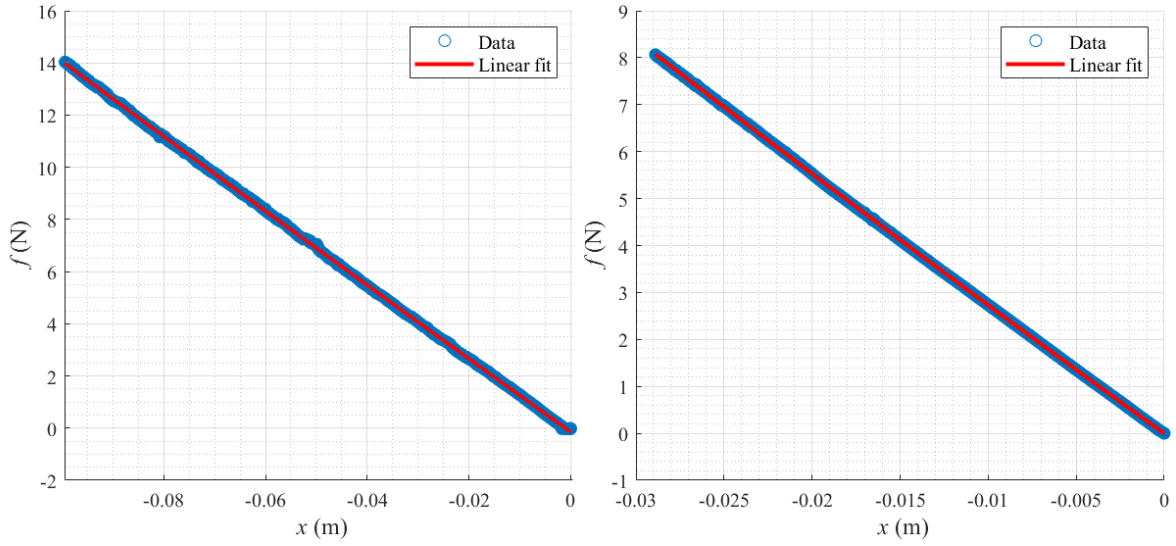

(a) (b)

Figure 5.1. Force displacement graphs for (a) horizontal, and (b) vertical springs for one specimen

5.2.2 Measuring the static behaviour of the mechanism

Once again, using the Instron machine pre-set, displacements were applied to the carriage and the induced force in the mechanism was measured. Therefore, the static behaviour of the mechanism was captured and is shown in Figure 5.2. A mechanism with 10 cm long arms, 0.7085 kg payload, 30 degrees initial unloaded angle, vertical and horizontal spring stiffness of 140 N/m and 280 N/m, respectively, was considered to calculate the analytical results. As shown in Figure 5.2, the analytical results are in reasonably good agreement with the experimental results. The reason that the fitting curve has an even powered term can be because of the friction which was not considered in the analytical model.

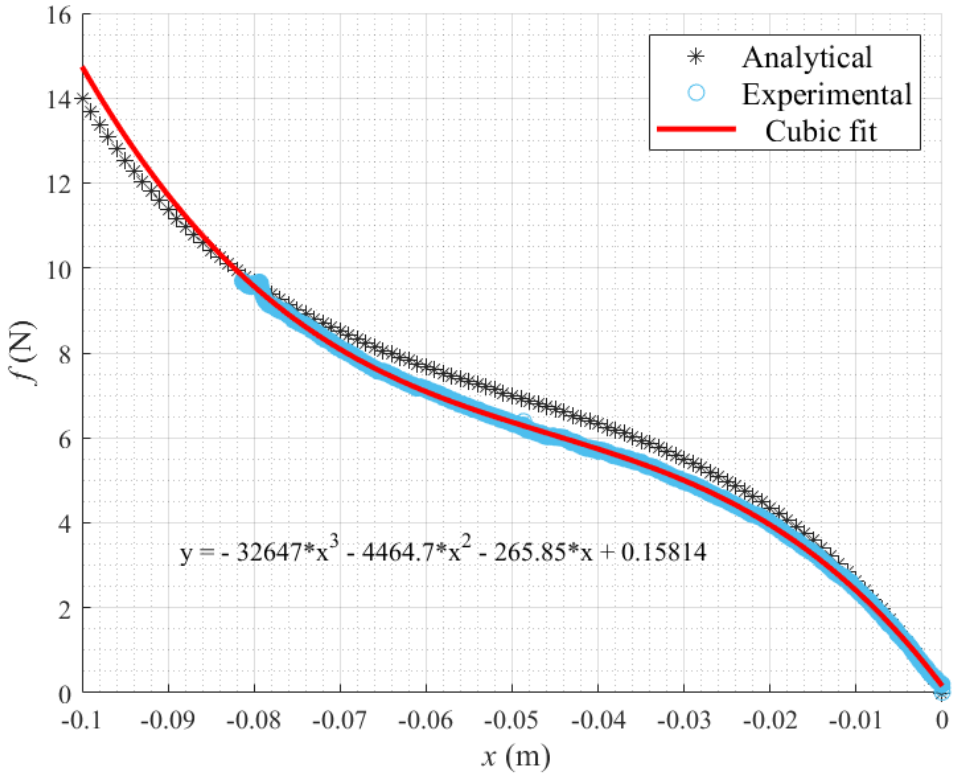

Figure 5.2. Force-displacement relation for the mechanism with $l = 0.1$ m, $k_h = 280$ N/m, $k_v = 140$ N/m, and $\theta_0 = 30°$.

5.2.3 Friction measurement from static tests

For measuring the friction in the system, the loading/unloading tests were conducted and the difference between those two equals twice the friction force. Therefore,

$$f_{dv} = \frac{F_{loading} - F_{unloading}}{2} \tag{5.1}$$

in which $F_{loading}$ and $F_{unloading}$ are the loading and unloading forces measured for each displacement respectively.

The tests were repeated several times and the average value of the friction force at $\theta = 0$ (y = 0.025 m) was measured as 0.47 N. Figure 5.3 (a) and (b) illustrate the force-displacement and

force-theta graph for loading/unloading of the rig with 5 cm long arms. Figure 5.4 (a) and (b) show the change in friction force with respect to displacement and angle of the arms (θ), respectively. As shown, the friction force increases initially when the applied force/displacement increases, then decreases to reach a minimum in the vicinity of $\theta = 0$ (y = 0.025 m), about 0.47 N. After this, the friction force increases.

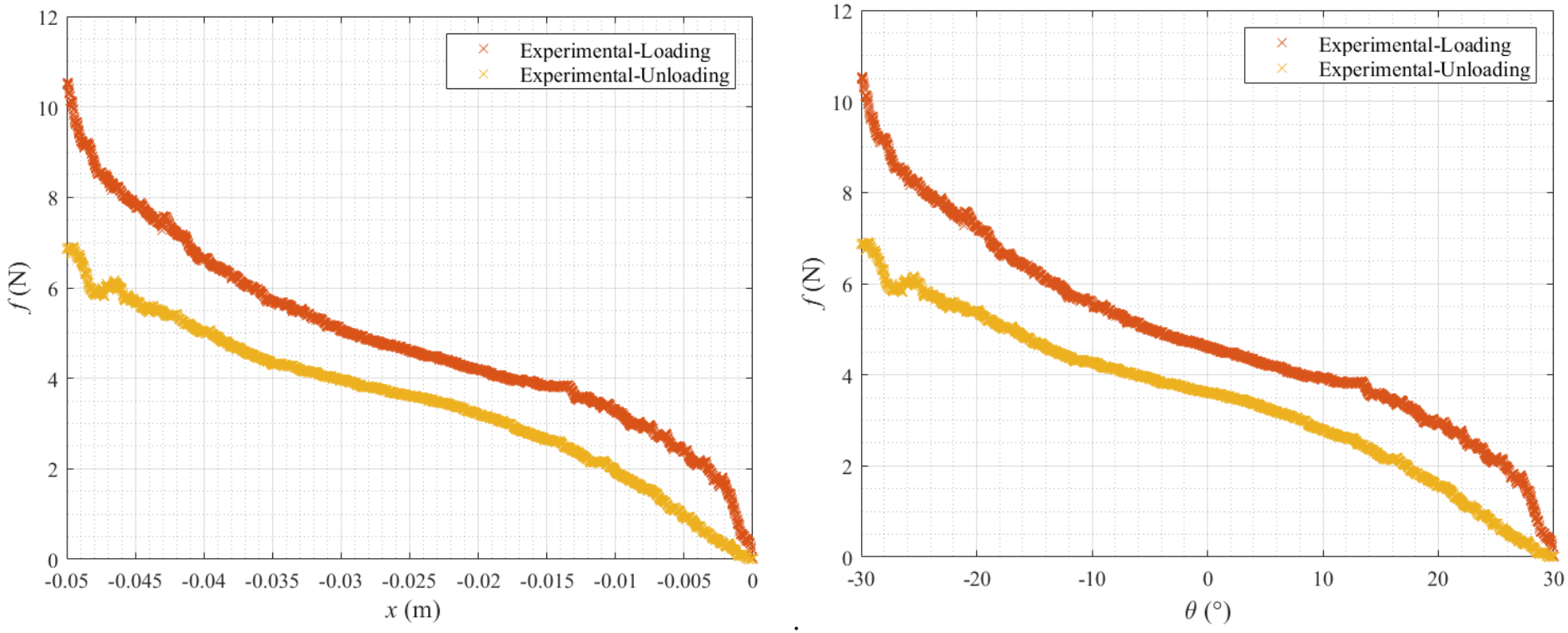

(a) (b)

Figure 5.3. (a) Force-displacement graph for the loading and unloading tests, (b) Force-theta graph for the loading and unloading tests for the mechanism with $l = 0.05$ m, $k_h = 280$ N/m, $k_v = 167$ N/m, and $\theta_0 = 30°$.

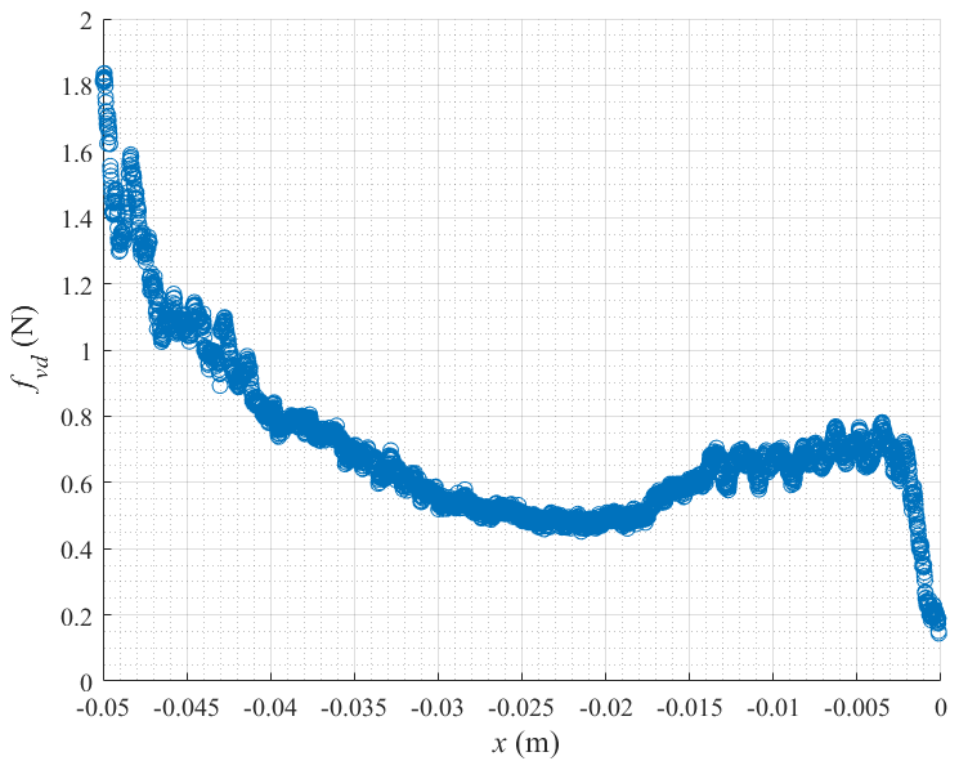

(a)

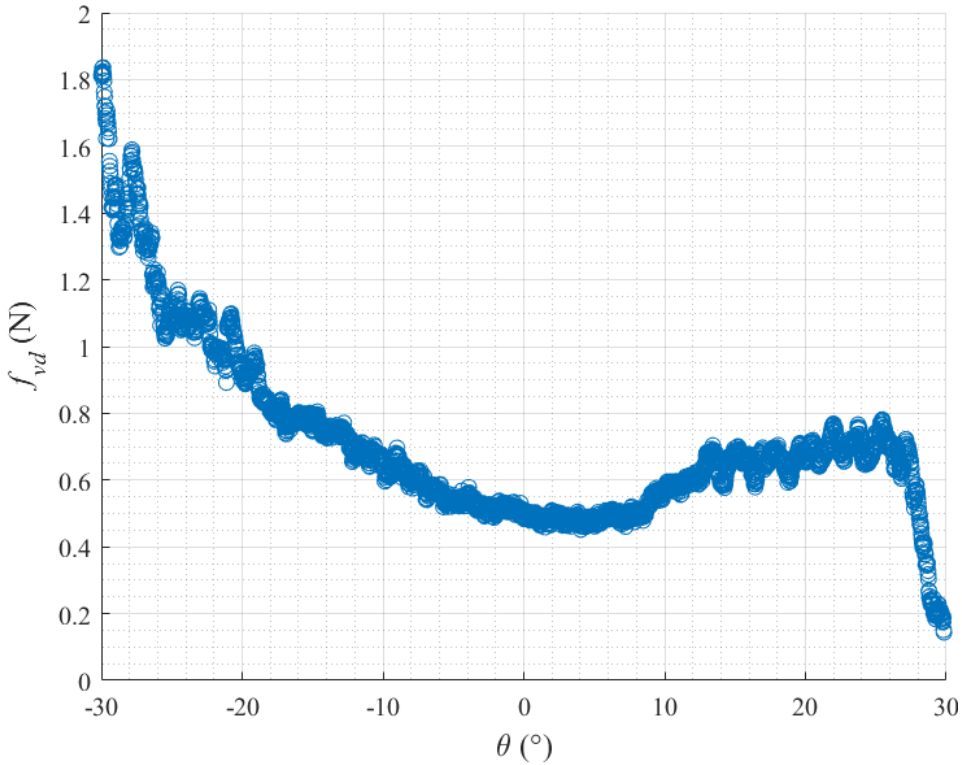

(b)

Figure 5.4. (a) Friction force-displacement graph, (b) friction force - θ graph for the mechanism with $l = 0.05$ m, $k_h = 280$ N/m, $k_v = 167$ N/m, and $\theta_0 = 30°$.

This is because of increasing force in the inclined bars which induces more compression on the platform resulting in more friction between the platform and the vertical bars. This also increases the friction in the horizontal bars because of the same reason. However, it is very difficult to differentiate between the vertical and the horizontal friction forces in the system. In this model, the friction force varies between 0.2 N and 1.85 N depending on the payload and the equilibrium position.

5.3 Time harmonic tests

5.3.1 Transmissibility measurement

The transmissibility of sinusoidal inputs was measured using displacement-controlled and acceleration-controlled tests. Figure 5.5 shows the transmissibility for various input amplitudes with displacement-controlled tests. As can be seen, the amplitudes less than 30 mm cannot excite the system to capture the resonance. This is because of friction in the system. For 30 mm amplitude, however, the resonance happened around 1.5 Hz. For this case, as there are multiple solutions available around resonance, the tests were done once slowly sweeping from low to high frequencies and again from high to low frequencies (SD). At the resonance, there is a flat part which occurred because the mass was overexcited and dispatched from the vertical spring. As can be seen, using displacement control tests, the mass was either under-excited (for the input amplitudes of less than 30 mm) or overexcited (for input amplitude of 30 mm). Therefore, the acceleration-controlled tests were used. In order to get more accurate results, a series of pure sinusoidal tests were conducted to find the transmissibility of the excitation for discrete frequency. This helped to capture more data around the jump frequencies at resonance.

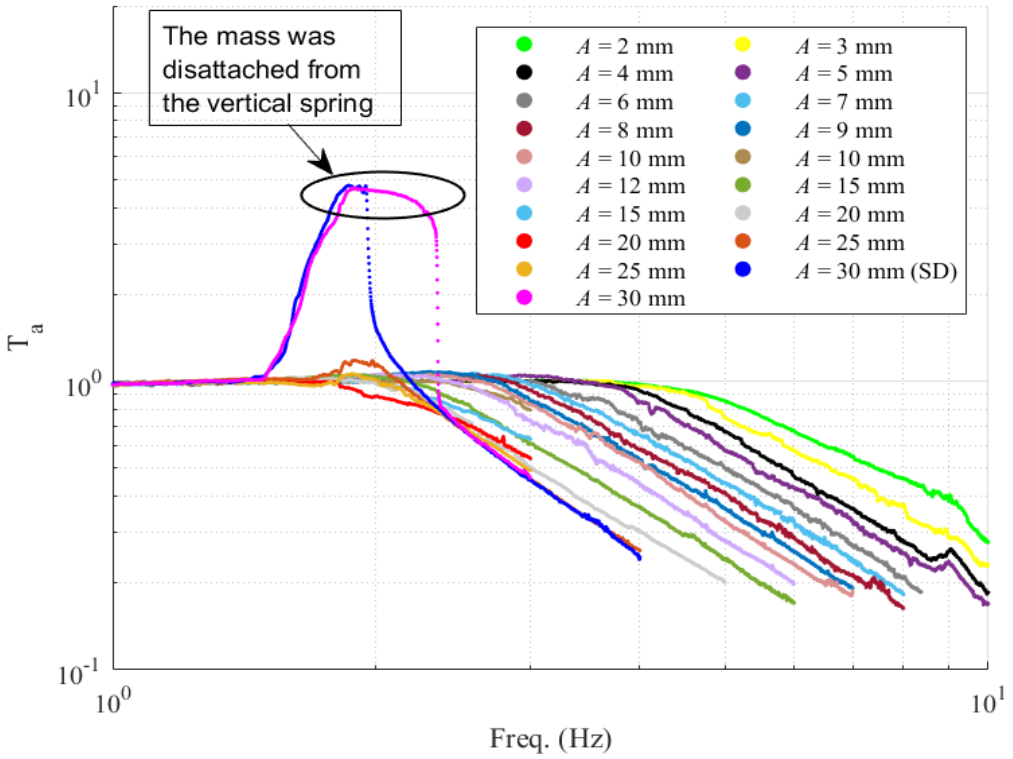

Figure 5.5. Transmissibility of the rig with m = 0.708 kg, $l = 0.1$ m, $k_h = 280$ N/m, $k_v = 140$ N/m, and $\theta_0 = 30°$ subjected to displacement-controlled time harmonic excitation with various amplitude.

It can be seen that the transmissibility is lower for high amplitudes (e.g. 30 mm) in higher frequency range, despite the higher stiffness. This may be because of the effect of dry friction. Considering the applied force as F ($F = m.A.\omega^2$) *as* a function of mass (m), frequency of the excitation (ω), and the excitation amplitude (A), for lower amplitude, the force is less than dry friction and the mass sticks and transmissibility is 1. When the applied force reaches dry friction force, the mass starts to slip. After that, force transmission can be decreased by the isolation system. The difference between the applied force and the friction force is an *isolatable force*. Therefore, by increasing the amplitude of the excitation, the isolatable force increases and as a result, transmissibility decreases at the high frequencies. However, around resonance frequency, by increasing the amplitude and isolatable force, transmissibility increases. Therefore, for high amplitude excitations the effect of dry friction is less than low amplitude excitations and does not significantly affect the performance of the mechanism.

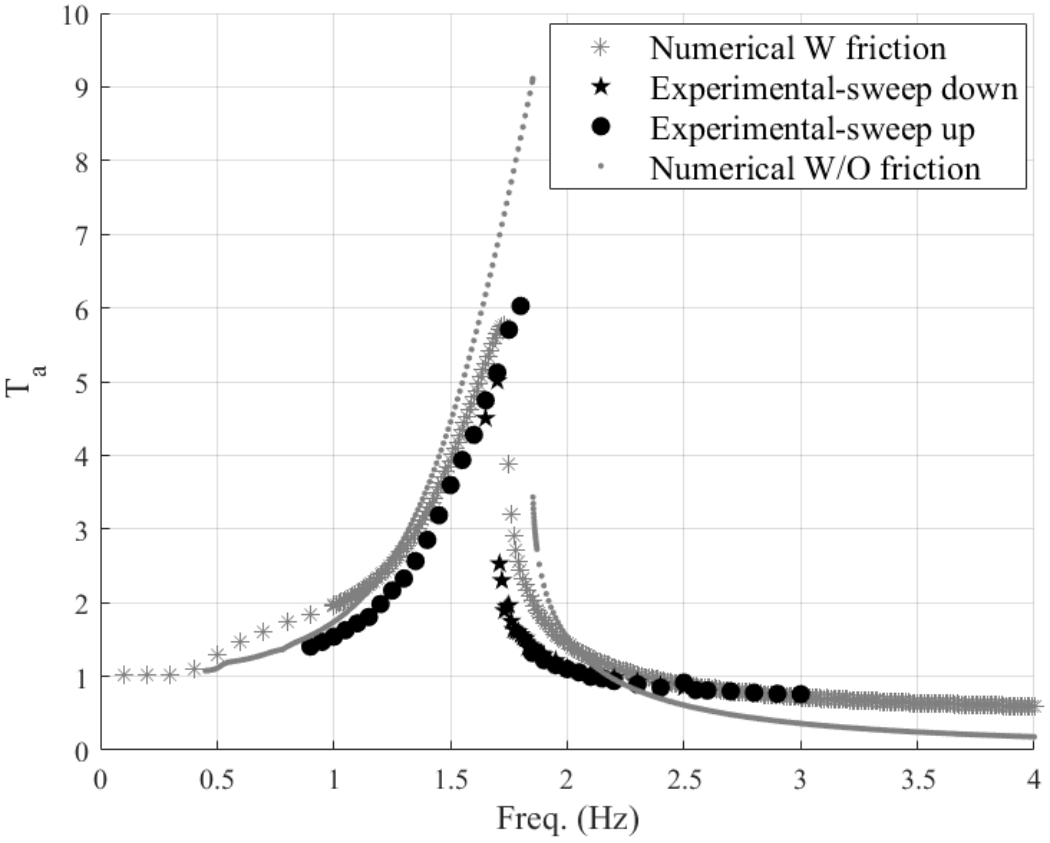

Figure 5.6. Analytical transmissibility in comparison to the experimental transmissibility of the rig with m = 0.708 kg, $l = 0.1$ m, $k_h = 280$ N/m, $k_v = 140$ N/m, and $\theta_0 = 30°$ subjected to acceleration-controlled time harmonic excitation with amplitude of 0.08g.

Figure 5.6 shows the experimental transmissibility compared to the numerical results for a case with and without friction subjected to constant acceleration inputs with amplitude of 0.08g. Damping ratio ξ, and velocity tolerance v_d in the numerical modelling are considered as 5% and 0.002 respectively. The friction force f_{dv} is considered as 0.27 N using a least squared error method explained in section 5.4.3. As can be seen in this figure, the transmissibility for the model with friction element has good agreement with the experimental results compared to that of the model without friction element. As evident, the agreement between experimental and numerical with 0.27 N friction is good. However, the transmissibility without friction has a much higher resonance amplitude. It means that considering friction element in the numerical

model is necessary. From the payload and the stiffness values given in the caption of Figure 5.6, the natural frequency of a linear system (without the arms and the horizontal springs) is calculated as 2.24 Hz, which means that the isolator reduces the resonance frequency of the system to 1.8 Hz and widens the isolation range. This is because of the negative stiffness coming from the horizontal springs making the system less stiff.

5.3.2 Friction measurement from time harmonic test

There was another technique which was used to measure the friction force in the system subjected to time harmonic test. For this purpose, the transmissibility shown in Figure 5.5 was used. In this case, the maximum friction force f_{dv} is given by

$$f_{dv} = m.A.\omega_{slip}^2 \tag{5.2}$$

in which ω_{slip} is the frequency at which the mass begins to slip to move, and A is the amplitude of the excitation and m is the mass of the payload. Figure 5.7 shows the measured friction force as a function of the excitation amplitude. As can be seen, the friction force in the system changed randomly between 0.5 N and 1.85 N. The mean value for these numbers gives 1.07 N for the maximum friction force.

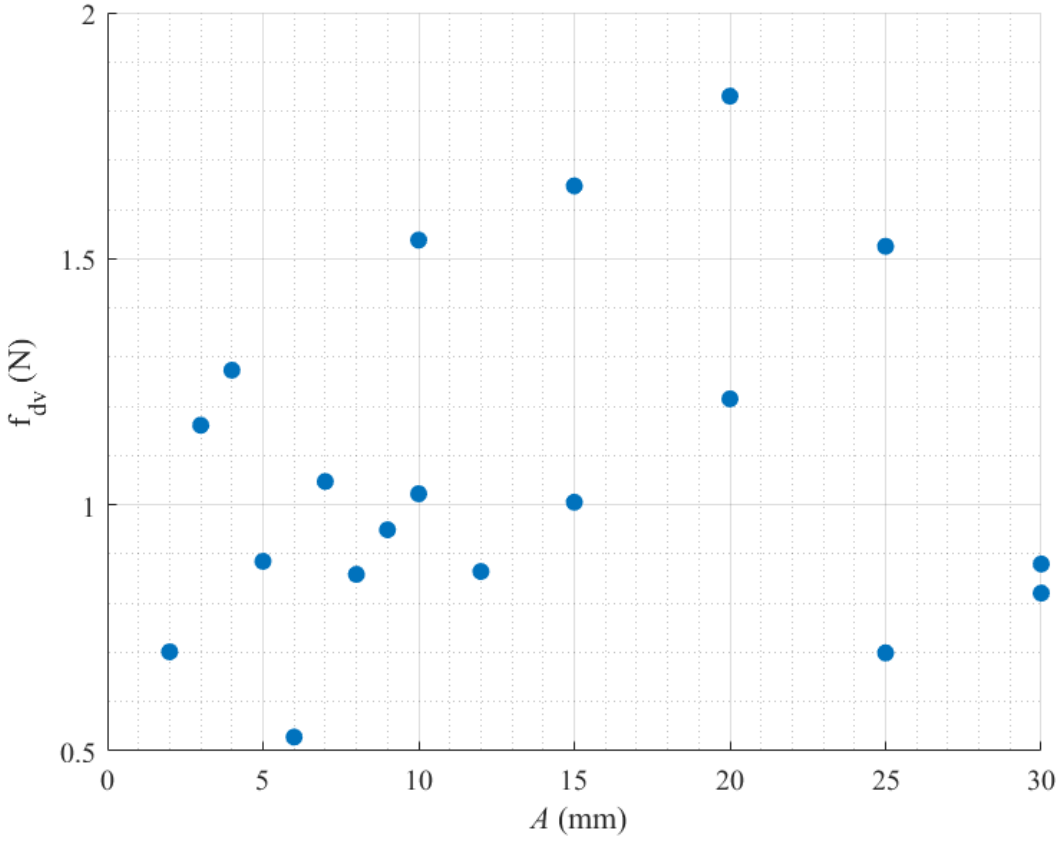

Figure 5.7. Maximum friction force vs. excitation amplitude for the mechanism with m = 0.708 kg, l = 0.1 m, k_h = 280 N/m, k_v = 140 N/m, and θ_0 = 30°.

5.4 Earthquake excitation inputs

Since the capacity of the shake-table was limited, the Bam, Christchurch, and LGPC earthquake signals were scaled. For this purpose, the acceleration amplitude was multiplied by 0.5, 0.4, and 0.7 for the mentioned signals respectively (the number before the name of an earthquake shows this multiplier). Since the main purpose of the experiments was to prove the concept and validate the numerical model, this scaling is unlikely to have any effect on the findings.

Figure 5.9 to Figure 5.16 show the calculated and measured response acceleration time histories in comparison to the base excitation for the rig. The strong part of the graphs is also presented to see the difference more clearly. As can be seen the numerical results with friction elements has good qualitative agreement with the experimental results. However, the responses without friction element have significant difference with the experimental responses. This can also be seen clearly when the peak and RMS values are compared numerically in Table 5-1 and Table 5-2. The differences between the results may be attributed to different factors, the most obvious being the approximation in modelling and estimating the friction. Other sources of deviation include but are not limited to, the inaccuracy in the determination of damping and stiffness values and simplifying assumptions regarding the distribution of inertia.

Table 5-1. Maximum measured and predicted input and response accelerations

Earthquake	Input signal peak	Response signal peak	Experimental	Predicted
0.5Bam	0.4841	0.1318	0.27	0.32
0.3Christchurch	0.7707	0.1404	0.18	0.15
ChiChi	0.3327	0.7395	2.22	2.63
El Centro-170	0.8976	0.2419	0.27	0.35
El Centro-182	0.2412	0.0799	0.33	0.44
EZ Turkey	0.248	0.1138	0.46	0.48
0.5 LGP	0.4414	0.1245	0.28	0.33
Northridge	0.6187	0.2689	0.43	0.48

Table 5-1 shows the calculated and measured peak acceleration for the input and output and their ratio to the base input. As is evident, both experimental and numerical results show more than 50% reduction in the maximum acceleration. Table 5-2 shows the corresponding results for the RMS values. The RMS acceleration is calculated for the stronger part of the signal with CE between 5% and 95%.

In all cases, reduction in both peak and RMS values is substantial except for Chichi earthquake which amplified the input excitation. An analysis of the frequency contents of the earthquake signals revealed that the ChiChi earthquake had a much a higher energy content in lower frequency range compared to other signals.

Table 5-2. RMS measured and predicted input and response accelerations in g

Earthquake	Input signal RMS	Response signal RMS	Experimental	Predicted
0.5Bam	0.1187	0.0366	0.31	0.31
0.3Christchurch	0.158	0.0268	0.17	0.21
ChiChi	0.0873	0.1535	1.76	2.19
El Centro-170	0.1174	0.059	0.50	0.36
El Centro-182	0.0695	0.0259	0.37	0.59
EZ Turkey	0.0538	0.0324	0.60	0.81
0.5 LGP	0.0753	0.0415	0.55	0.53
Northridge	0.1187	0.0366	0.31	0.31

Figure 5.8 (a), and (b) show the FFT of the input and response accelerations, respectively. As evident, the mechanism isolated the input excitation effectively for higher frequencies (more than 3 Hz). However, frequencies less than 3 Hz were magnified because of the resonance. The Chichi earthquake is relatively rich in low frequencies close to the natural frequency of the system and as a result, the response of the system to this signal was magnified to twice the input acceleration. Therefore, the mechanism works well for inputs with high frequency contents as is expected in the near fault earthquakes.

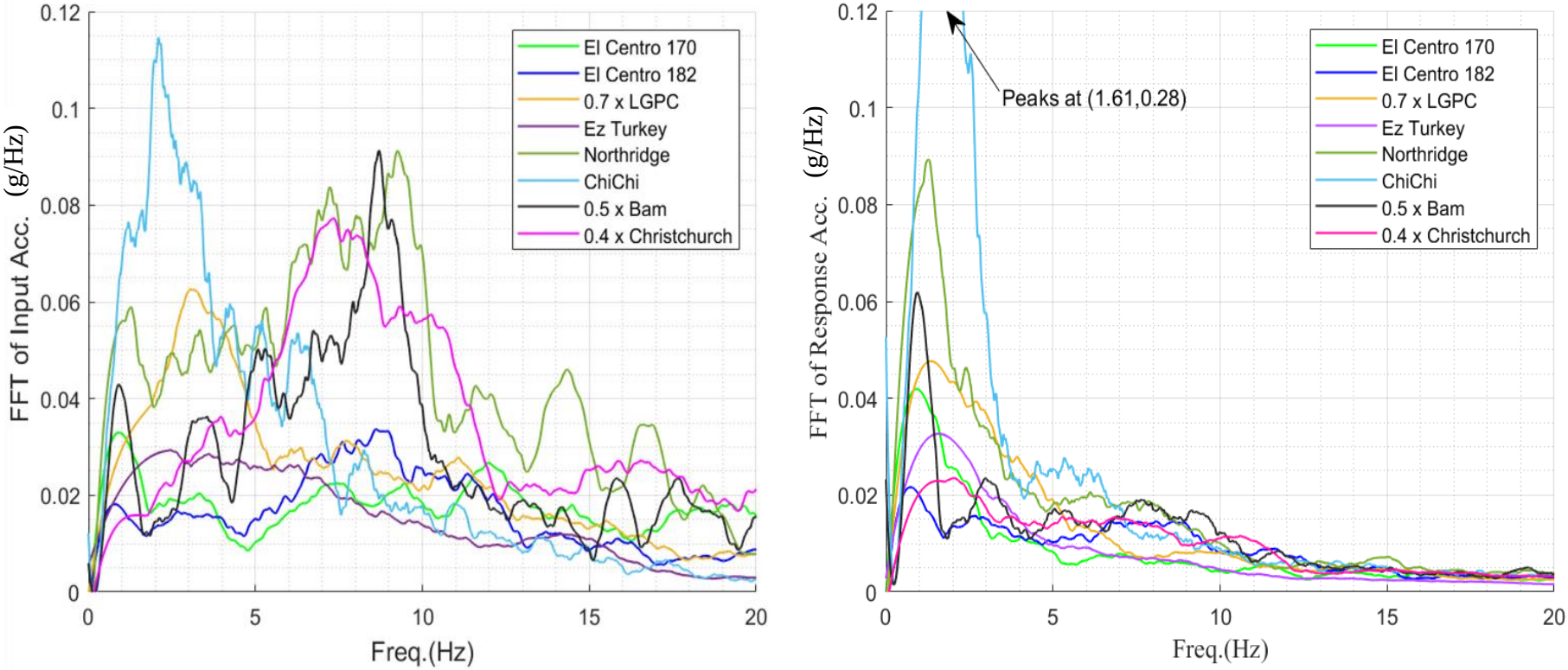

Figure 5.8. FFT of (a) the input acceleration time histories, and (b) the response acceleration time histories for the mechanism with m = 0.708 kg, $l = 0.1$ m, $k_h = 280$ N/m, $k_v = 140$ N/m, and $\theta_0 = 30°$.

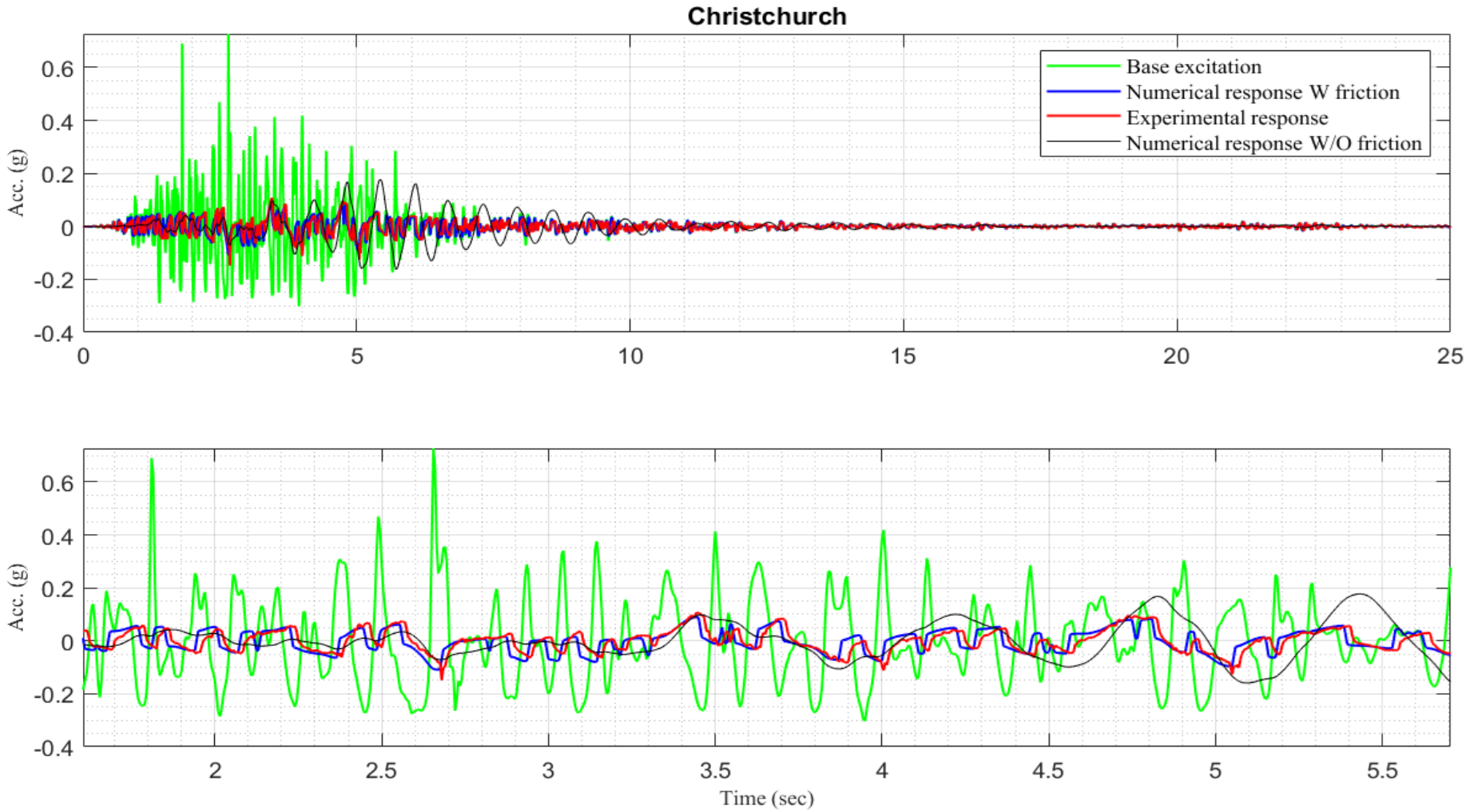

Figure 5.9. Christchurch base excitation, experimental and numerical response acceleration time histories for the mechanism with m = 0.708 kg, $l = 0.1$ m, $k_h = 280$ N/m, $k_v = 140$ N/m and $\theta_0 = 30°$.

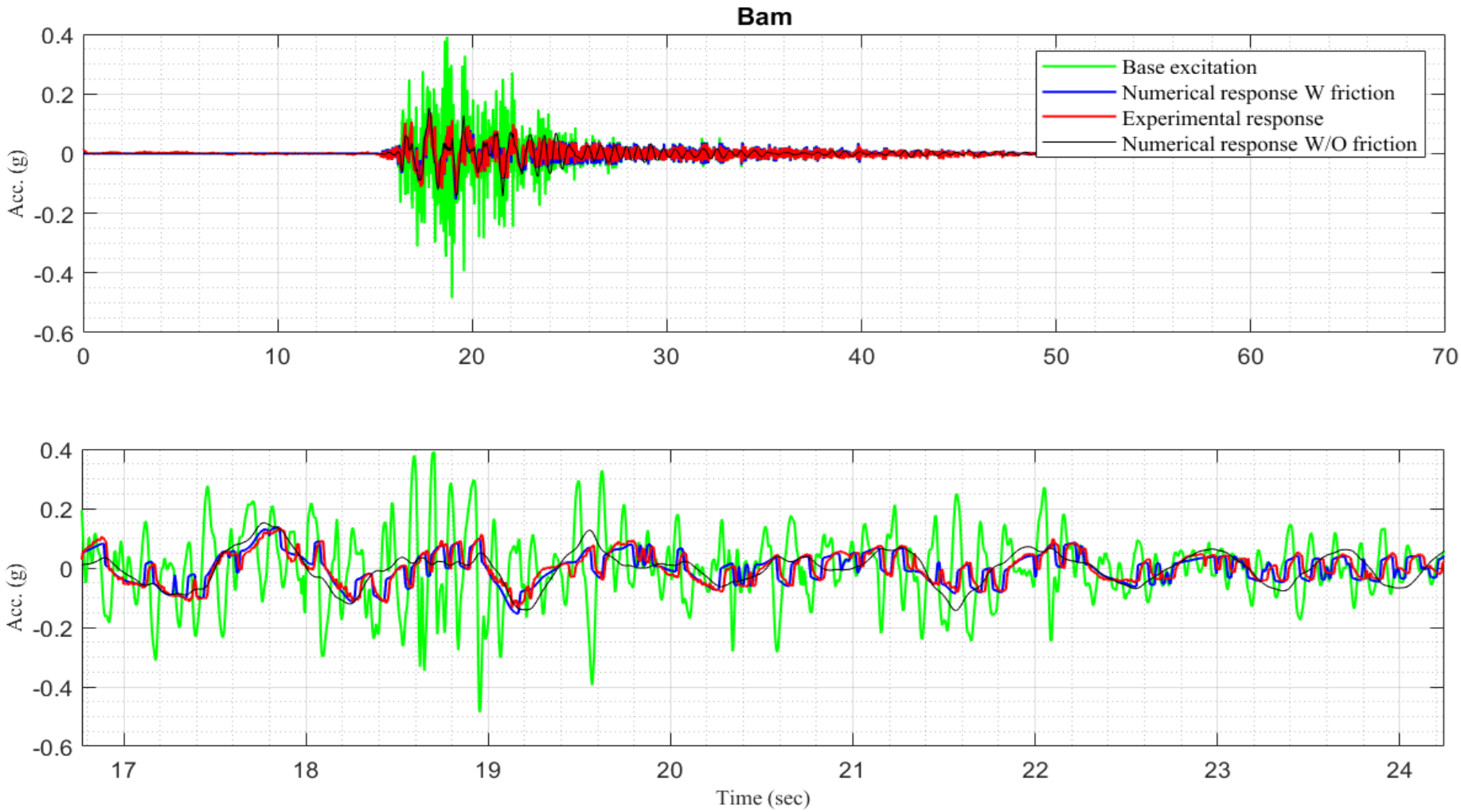

Figure 5.10. Bam base excitation, experimental and numerical response acceleration time histories for the mechanism with m = 0.708 kg, $l = 0.1$ m, $k_h = 280$ N/m, $k_v = 140$ N/m and $\theta_0 = 30°$.

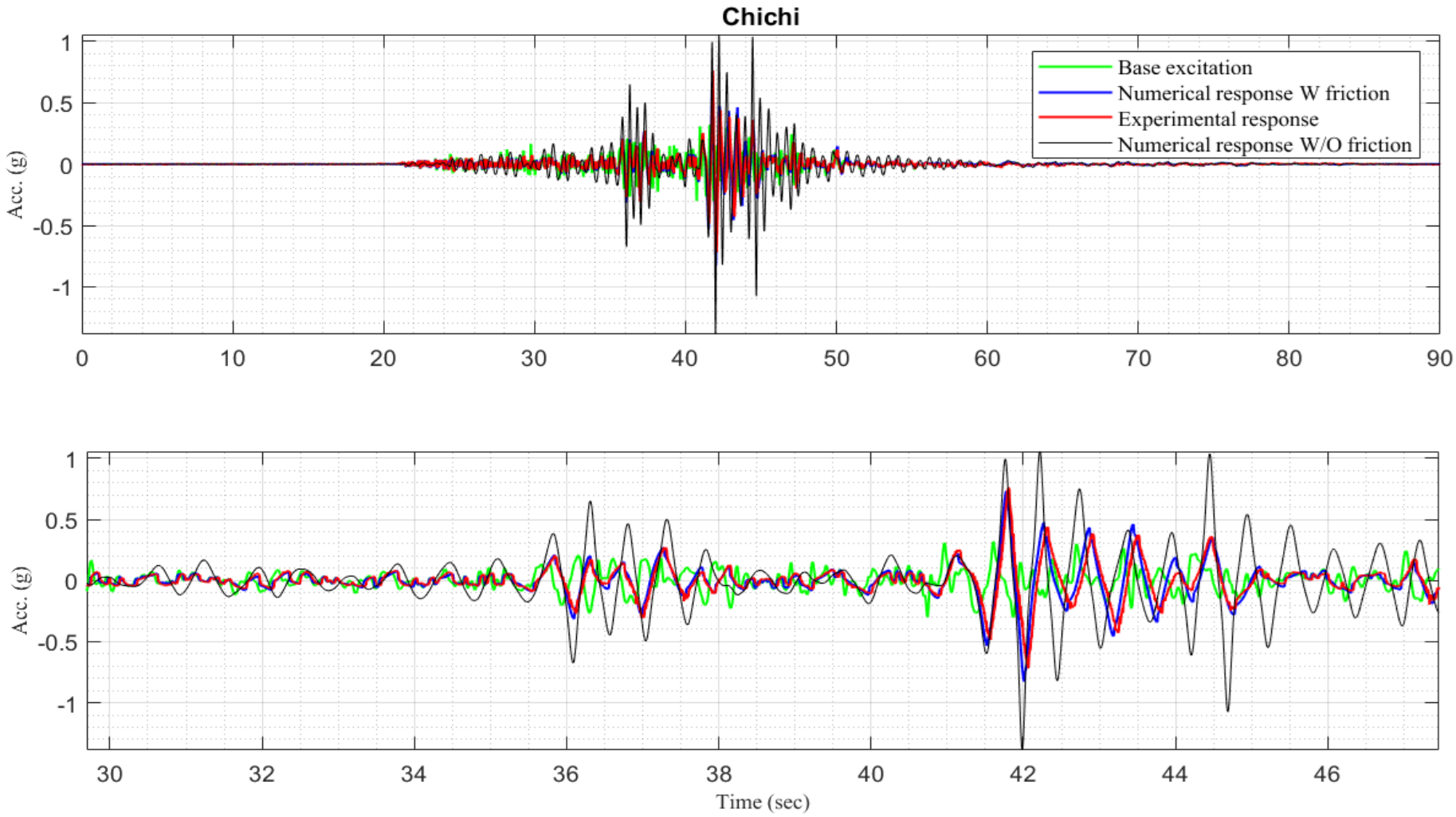

Figure 5.11. Chichi base excitation, experimental and numerical response acceleration time histories for the mechanism with m = 0.708 kg, $l = 0.1$ m, $k_h = 280$ N/m, $k_v = 140$ N/m and $\theta_0 = 30°$.

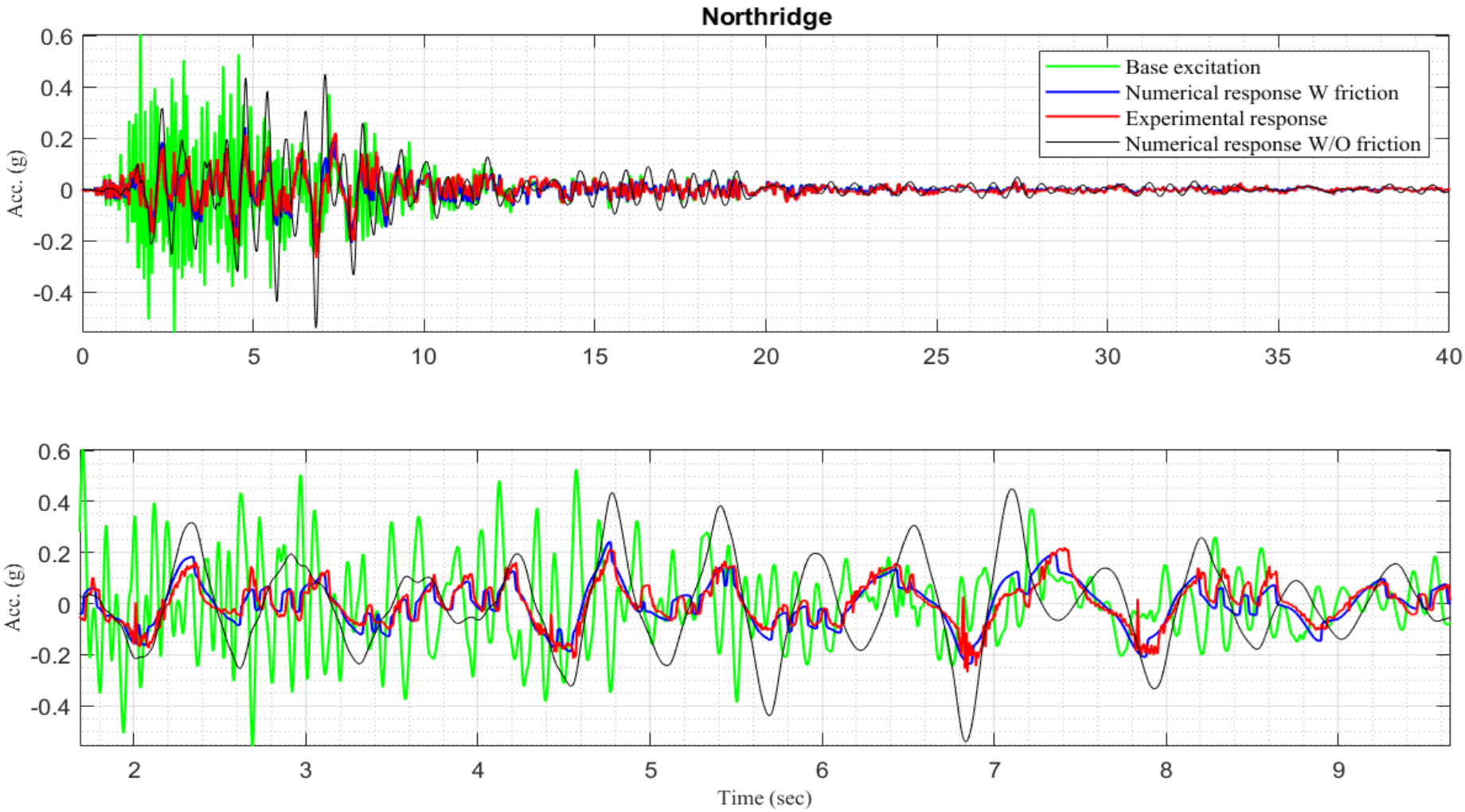

Figure 5.12. Northridge base excitation, experimental and numerical response acceleration time histories for the mechanism with m = 0.708 kg, $l = 0.1$ m, $k_h = 280$ N/m, $k_v = 140$ N/m and $\theta_0 = 30°$.

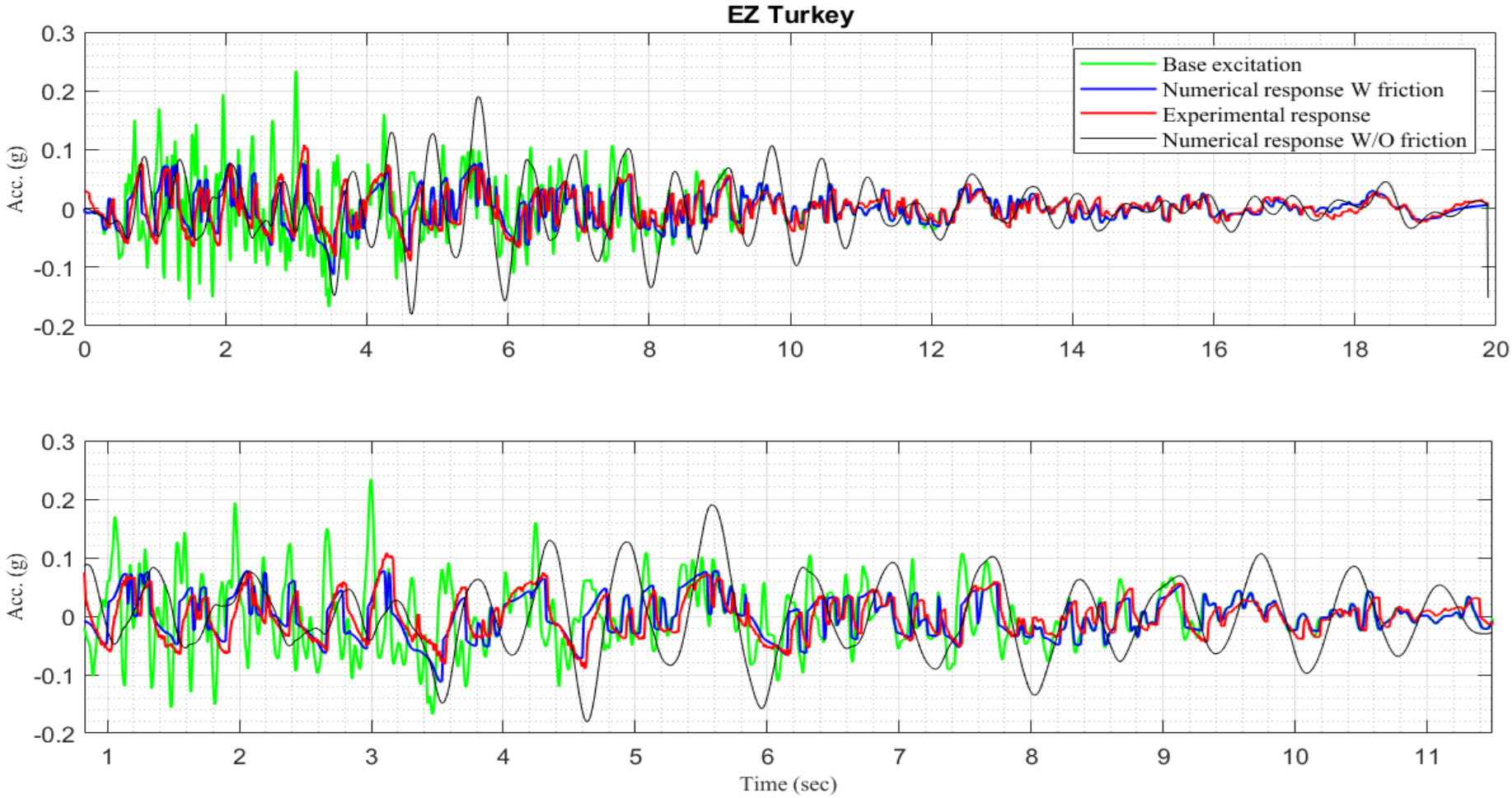

Figure 5.13. EZ Turkey base excitation, experimental and numerical response acceleration time histories for the mechanism with m = 0.708 kg, $l = 0.1$ m, $k_h = 280$ N/m, $k_v = 140$ N/m and $\theta_0 = 30°$.

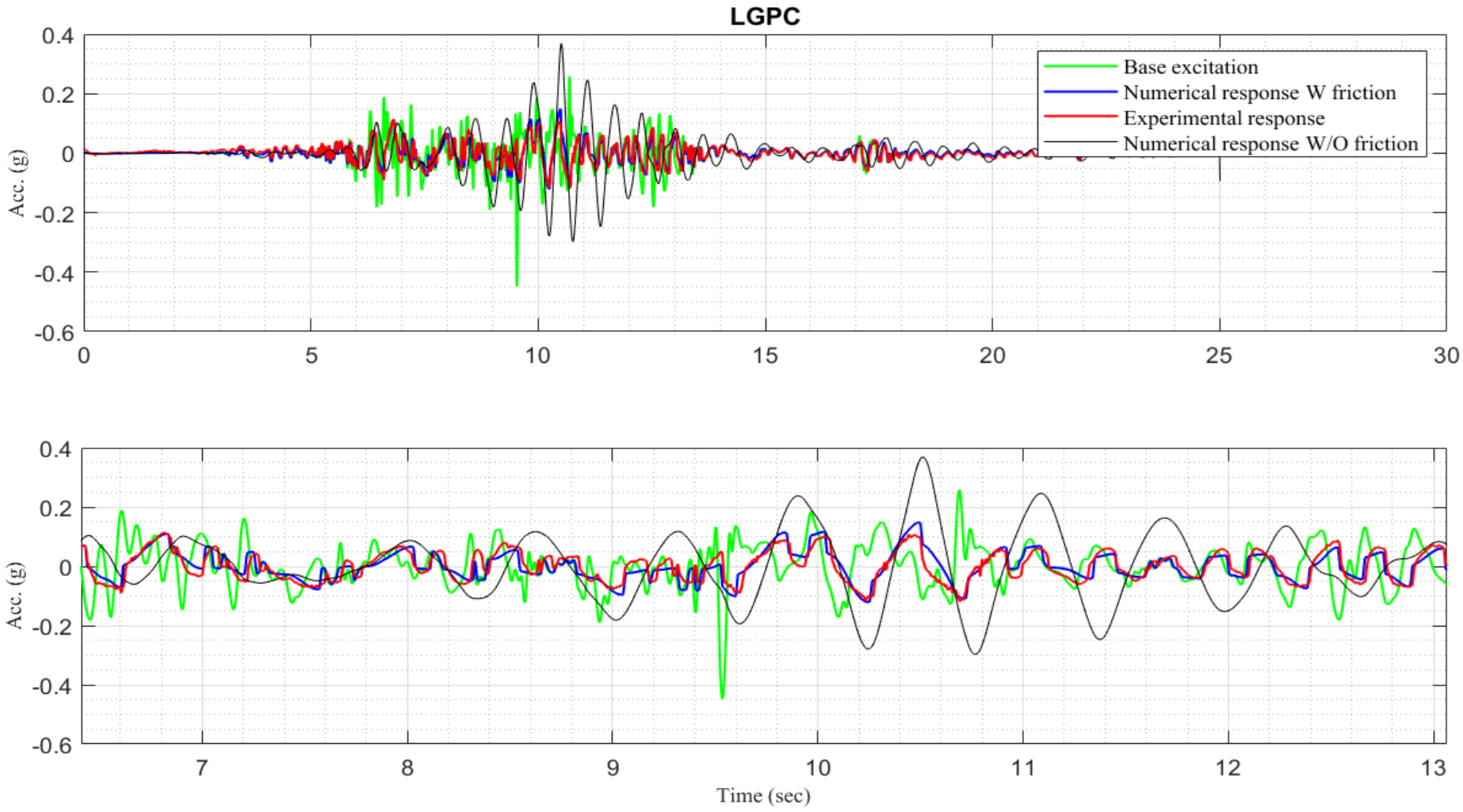

Figure 5.14. LGPC base excitation, experimental and numerical response acceleration time histories for the mechanism with m = 0.708 kg, $l = 0.1$ m, $k_h = 280$ N/m, $k_v = 140$ N/m and $\theta_0 = 30°$.

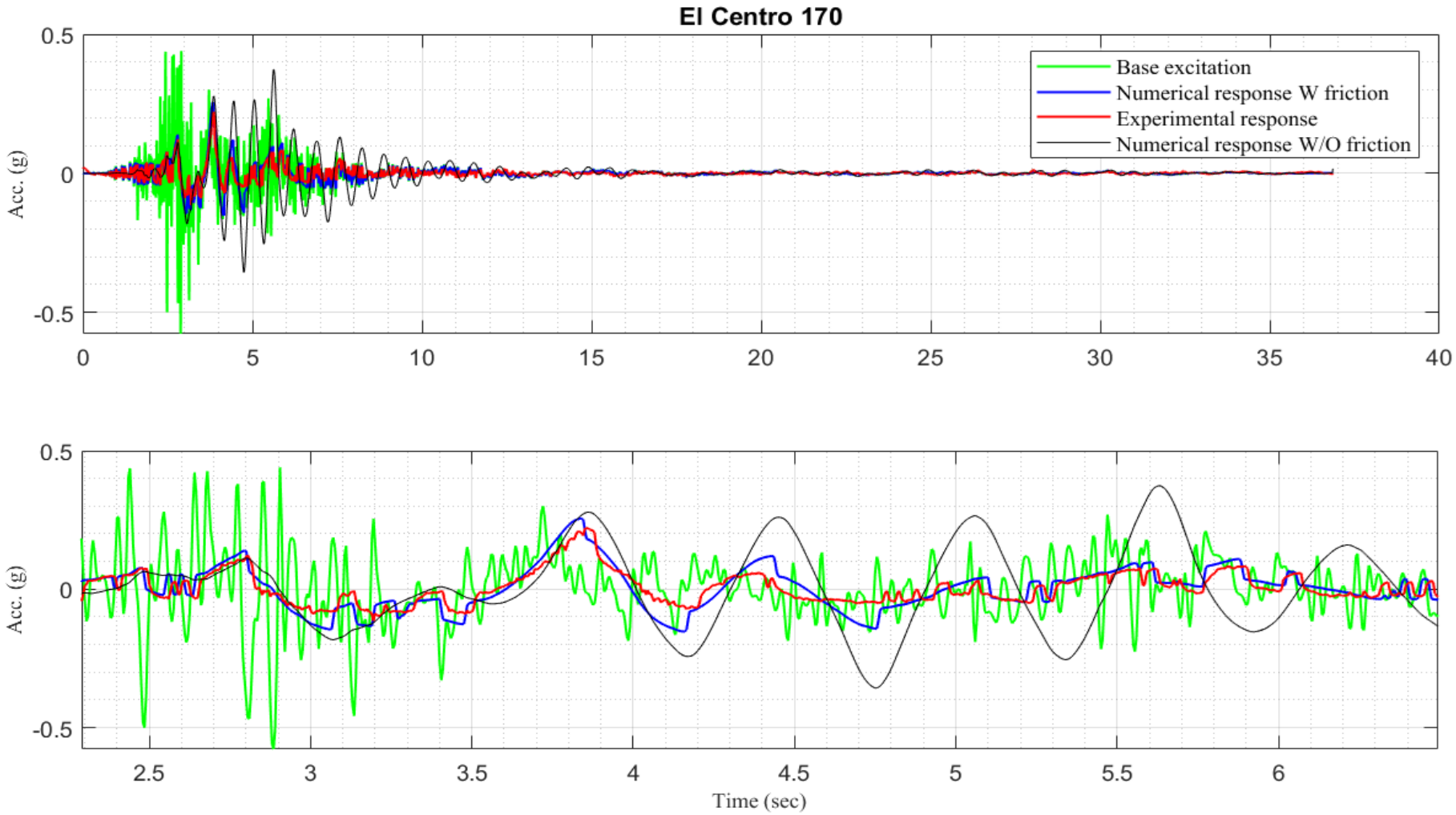

Figure 5.15. EL Centro170 base excitation, experimental and numerical response acceleration time histories for the mechanism with m = 0.708 kg, l = 0.1 m, $k_h = 280$ N/m, $k_v = 140$ N/m and $\theta_0 = 30°$.

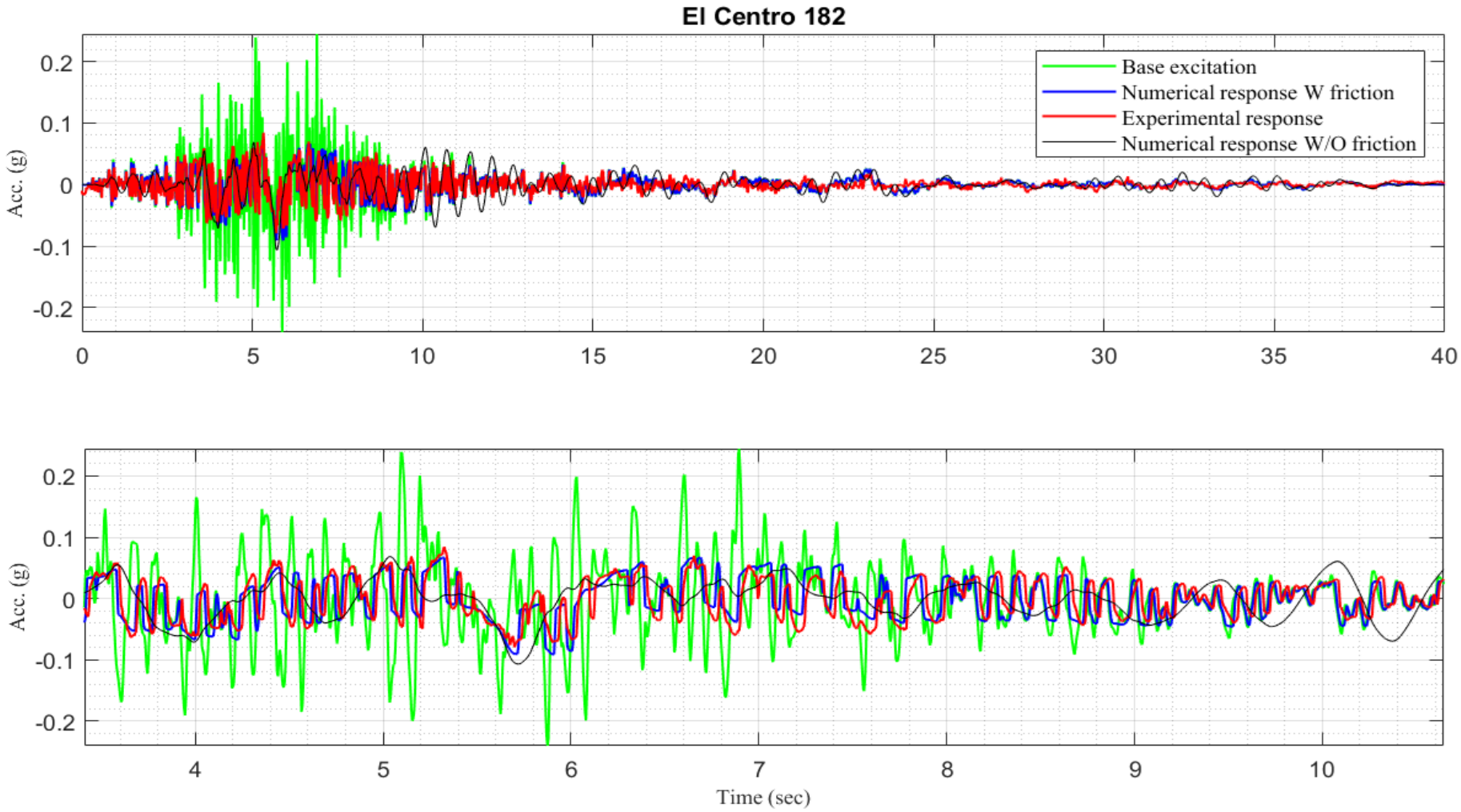

Figure 5.16. EL Centro182 base excitation, experimental and numerical response acceleration time histories for the mechanism with m = 0.708 kg, l = 0.1 m, $k_h = 280$ N/m, $k_v = 140$ N/m and $\theta_0 = 30°$.

5.4.1 Mistuning and change in the payload

So far, it was seen that a non-QZSS can significantly reduce the maximum as well as the RMS level of the response acceleration. The isolation was effective for frequencies higher than 3 Hz. As discussed in chapter 2 section 2.6, there might be some mistuning in the location of the mass or change in the payload applied on the system. Therefore, it is important to evaluate the performance of the system with mistuning or change in the load subjected to earthquake. In this section, mistuning and change in the payload are observed and the results are presented.

Figure 5.17 shows the experimental results comparing the response of the mechanism with horizontal arms in the static equilibrium position as well as for the cases with $\pm 0.1l$ mistuning. In order to make the mistuning, the vertical spring was pushed up or pushed down, without making any other changes to the rig. As can be seen in the figure, although there are some fluctuations in the response, there is no noticeable changes in the general response of the system. In other words, the system shows resilience in that its performance is not noticeably affected by a small shift in the location of the vertical spring.

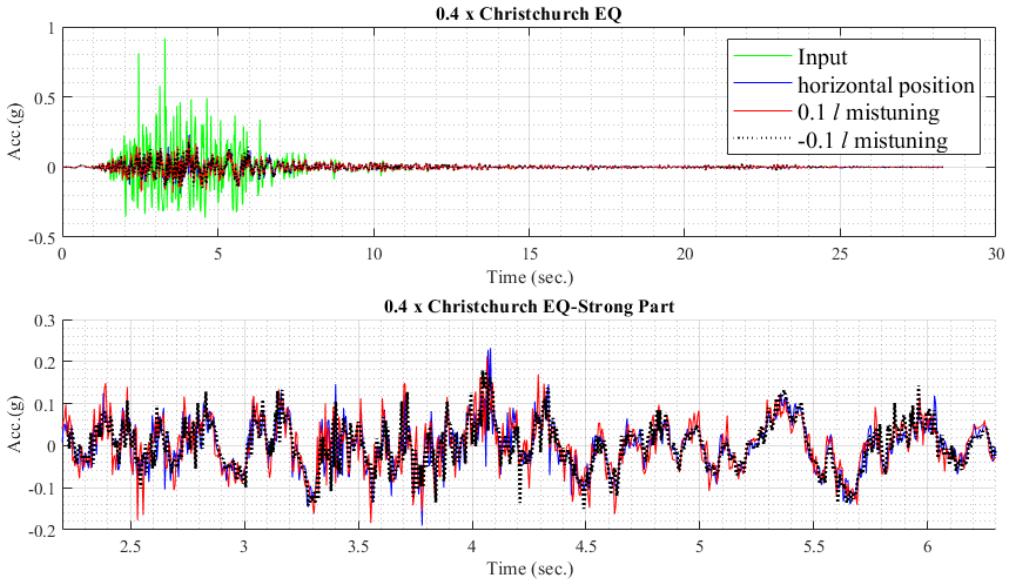

Figure 5.17. Acceleration time history for the mechanism with mistuning for the mechanism with m = 0.708 kg, $l = 0.1$ m, $k_h = 280$ N/m, $k_v = 140$ N/m and $\theta_0 = 30°$.

Similar results are recorded for slight changes in the payload of the platform. Three payloads have been tested in experiments: 679.78g, 720.08g, and 740.62g. Figure 5.18 shows the response of the system for three different values of payload. As is evident, there is only a very small difference between the results which shows that the system is not sensitive to a slight change in the payload and exhibits similar isolation performance.

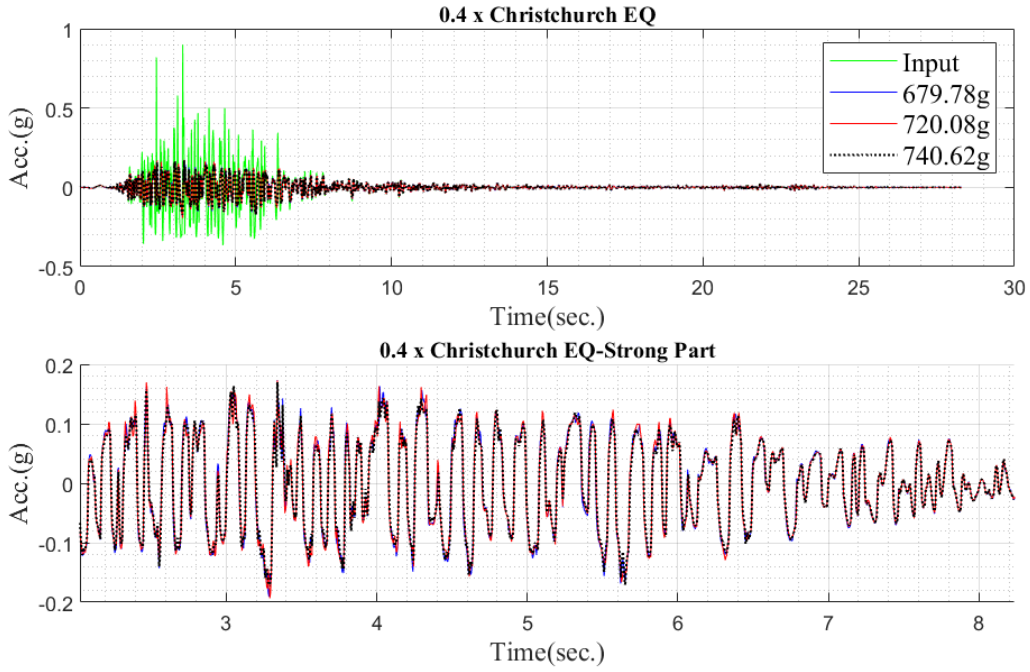

Figure 5.18. Acceleration time history for the mechanism with change in the weight for the mechanism with $l = 0.1$ m, $k_h = 280$ N/m, $k_v = 140$ N/m, and $\theta_0 = 30°$.

5.4.2 Different intensities

In this section, the effect of intensity of the input excitation (amplitude input acceleration) on the performance of the HSLDSS and the system with mistuning and different loadings is investigated. The maximum response of these system is compared as well as the RMS of the strong part of the response to see how the response changes with different intensities.

Figure 5.19 shows the response of the system to the Christchurch earthquake input with four intensities: 0.1, 0.2, 0.3, and 0.4 time the actual acceleration. In other words, the scale factor of 0.1, 0.2, 0.3, and 0.4 are considered to scale the amplitude of the input acceleration. Figure 5.20 also shows the strong part of the input and output signals with a higher resolution. As can be seen, by increasing the intensity of the input (larger amplitude) the response amplitude of the system decreases with respect to the input. This is because of the friction force. While the friction force is larger than the applied force, the mechanism sticks and does not work. In this case the payload and the base move together. However, by increasing the amplitude of the input acceleration, the applied force increases. If this force is large than the friction force, the difference between the applied force and the friction force can be isolated by the mechanism. Therefore, a larger intensity, which causes higher applied force, increases the performance of the isolator.

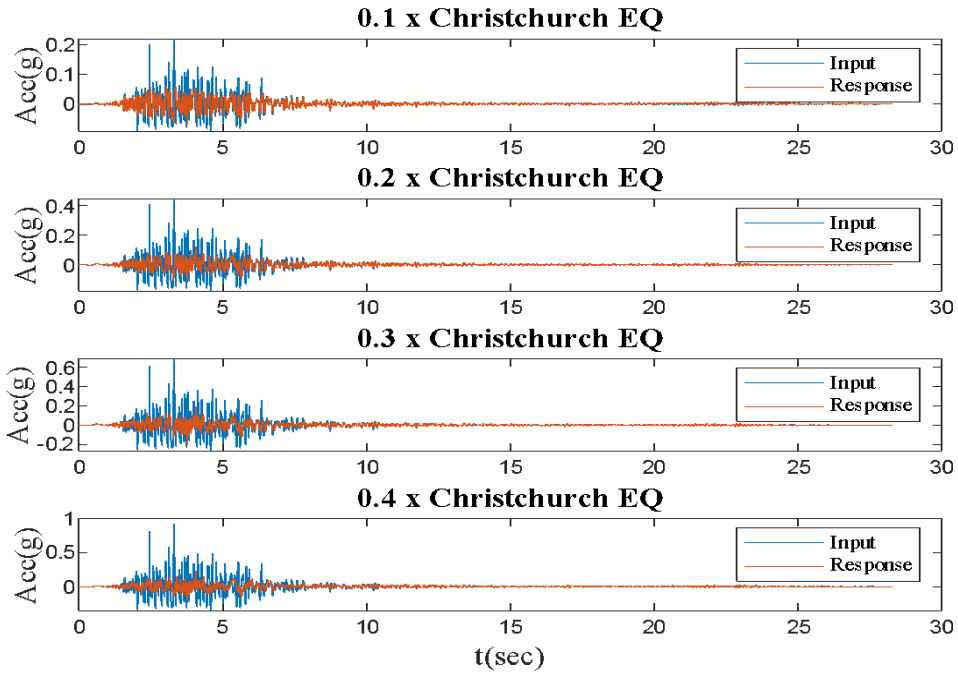

Figure 5.19. Acceleration time histories for Christchurch earthquake with various intensity for the mechanism with m = 0.708 kg, $l = 0.1$ m, $k_h = 280$ N/m, $k_v = 140$ N/m, and $\theta_0 = 30°$.

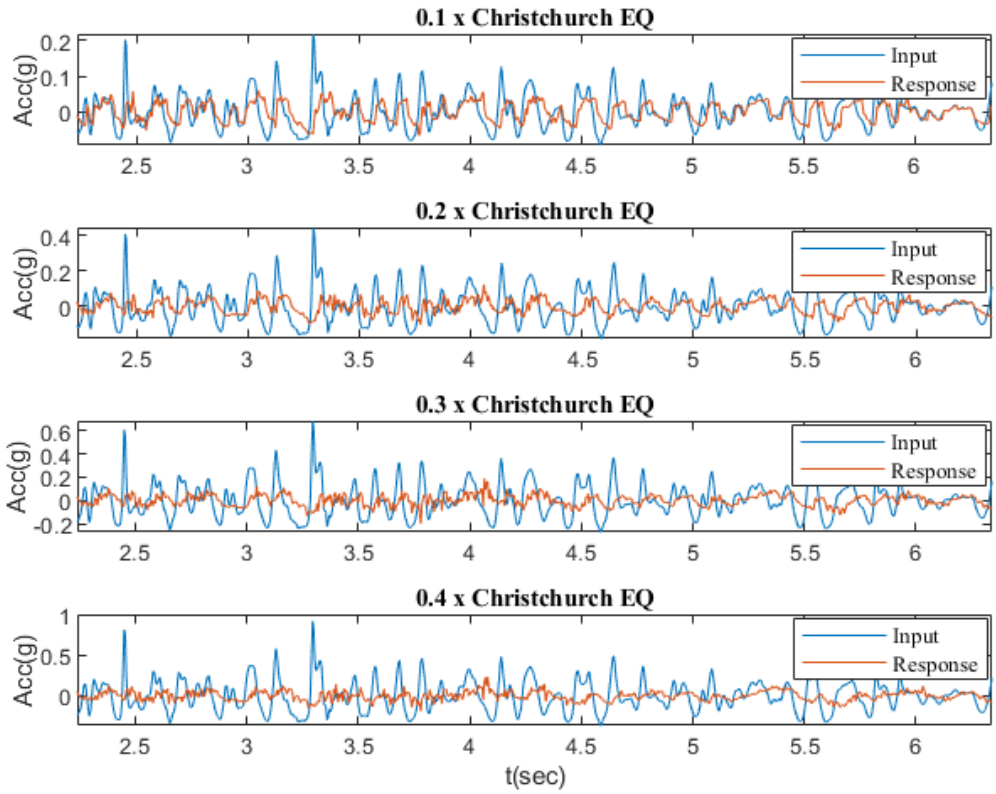

Figure 5.20. Strong part of acceleration time histories for Christchurch earthquake with various intensity for the mechanism with m = 0.708 kg, $l = 0.1$ m, $k_h = 280$ N/m, $k_v = 140$ N/m, and $\theta_0 = 30°$.

To study the performance of the mechanism with mistuning under earthquakes with various intensities, the results are compared in Figure 5.21 and Figure 5.22 (the strong parts). As evident, the responses of the system without and with $0.1l$ mistuning subjected to various intensity of inputs are similar. This shows that the isolation performance of the system is not significantly affected by mistuning and demonstrates its resilience.

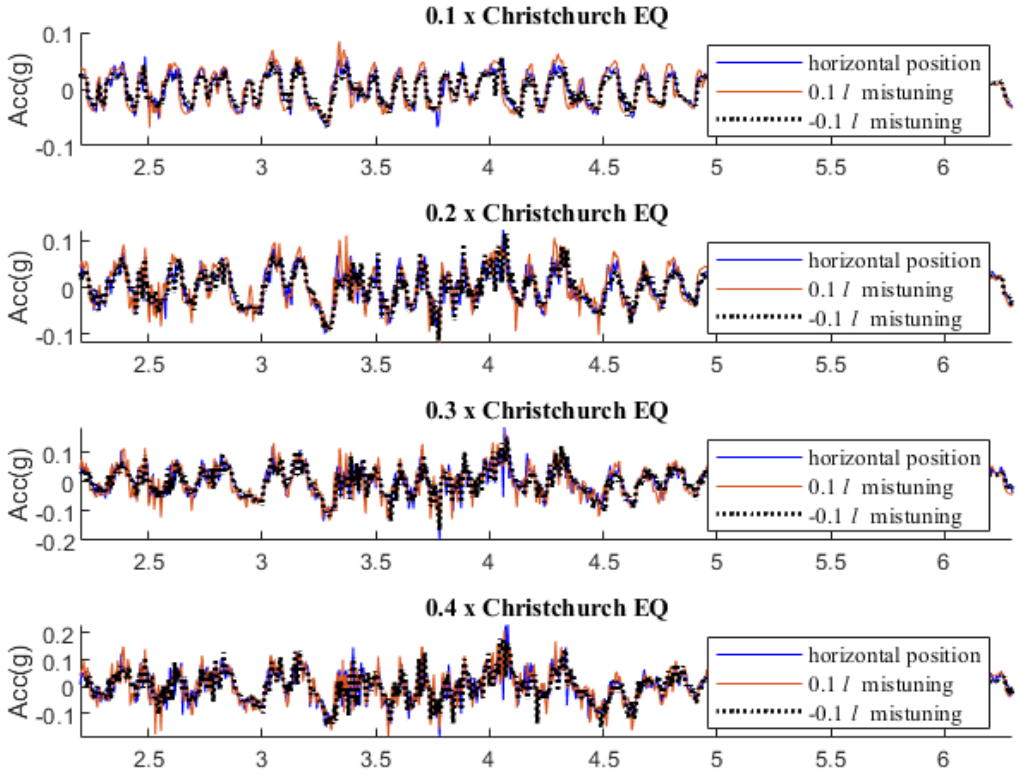

Figure 5.21. Acceleration time history for the mechanism with mistuning subjected to the Christchurch earthquake input for the mechanism with m = 0.708 kg, $l = 0.1$ m, $k_h = 280$ N/m, $k_v = 140$ N/m, and $\theta_0 = 30°$.

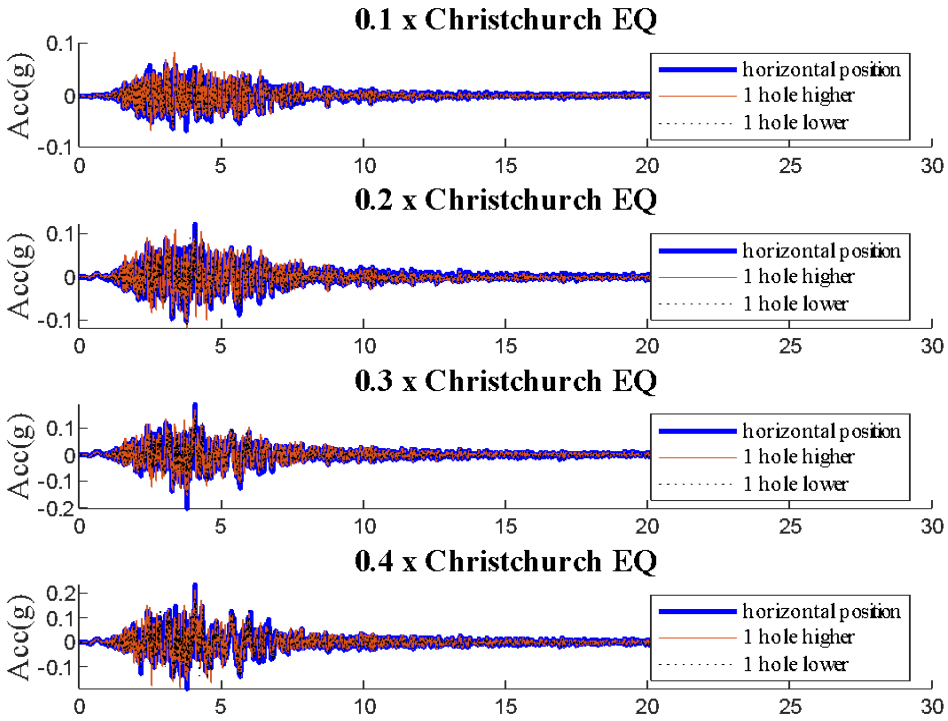

Figure 5.22. Acceleration time history for the mechanism with mistuning subjected to the Christchurch earthquake input

Figure 5.23 indicates the maximum acceleration and RMS level of the response of systems with mistuning subjected to the Christchurch signal with intensities of 0.1, 0.2, 0.3, and 0.4 times the original acceleration. Figure 5.23 (a) shows the RMS response versus RMS input. As can be seen, by increasing the amplitude of the input acceleration, the RMS value of the response drops initially in all cases. Then it increases. Figure 5.23 (b) shows the ratio of output/input RMS versus RMS of the input acceleration. As can be seen, this ratio decreases rapidly at first and then continues decreasing. It is also evident that the RMS response for the mechanism with $0.1l$ mistuning subjected to low intensity (0.1 Christchurch excitation) is higher than the one without mistuning and the one with $-0.1l$ mistuning. However, with increasing intensity, the mistuning effect on the RMS diminishes and tends to merge at high levels of excitation.

Figure 5.23 (c) shows the maximum response acceleration versus maximum input acceleration. For the case without mistuning, the maximum acceleration gradually increases by increasing the input acceleration. The response of the system with $0.1l$ mistuning drops suddenly by increasing the acceleration of the input. After that, it remains nearly constant. For the system with $-0.1l$ mistuning, however, the response decreases initially and then increases. By looking at the ratio of maximum output/input acceleration to maximum input acceleration presented in Figure 5.23 (d), it is evident that the response of the system with $\pm 0.1l$ mistuning decreases by increasing input acceleration at first and then remains almost constant. The system without mistuning, however, has near constant response ratios for various input acceleration intensities.

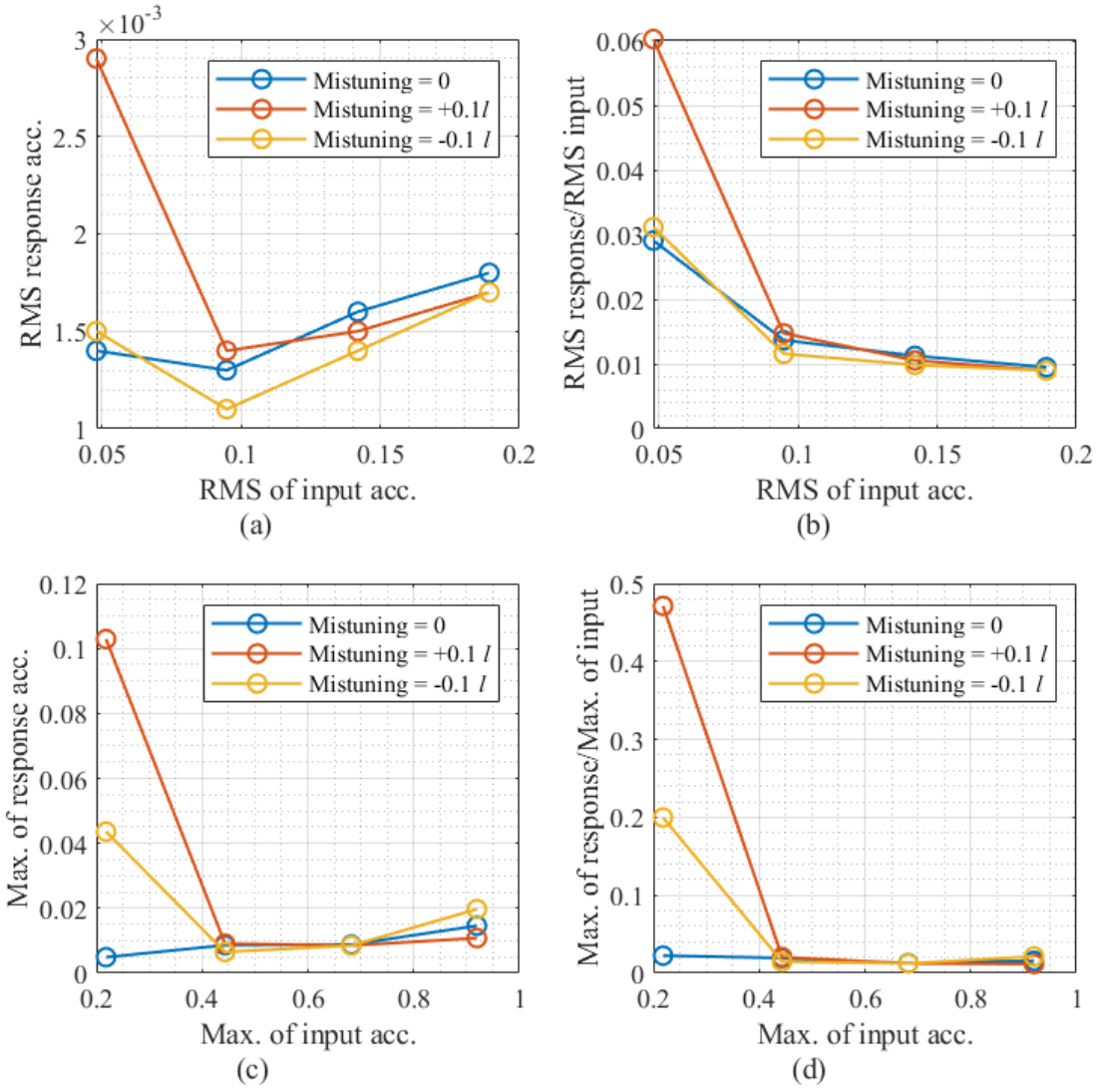

Figure 5.23. Maximum and RMS of acceleration for Christchurch earthquake with various intensity for mechanism with mistuning

5.4.3 Friction measurement from earthquake excitations

Although the friction force was measured using two different methods, the numerical results for earthquake simulation using those values do not agree with the experimental results.

Therefore, the least squared error method was used to calculate the friction force to model the earthquake response. In this method, the numerical acceleration response for various values of maximum friction forces (f_{dv}) was calculated for those eight earthquake inputs. The squared error is given as

$$e^2 = \sum \left(a_{exp}(t) - a_{num}(t, f_{dv}) \right)^2 \tag{5.3}$$

in which t is time, a_{exp} is the experimental response acceleration time history and a_{num} is the numerical response acceleration time history.

Figure 5.24 illustrates Eq. (5.3) for various friction forces and earthquake inputs. As can be seen, the maximum friction force which makes this squared error minimum is different for each earthquake inputs. These values are shown in Table 5-3 for three different sets of data. The

mean of these values is 0.27 N which shows good agreement between experimental and numerical results for both harmonic and earthquake tests.

Table 5-3. Friction force for each earthquake

Earthquake name	Friction force-set 1	Friction force-set 2	Friction force-set 3
El Centro-170	0.11	0.07	0.11
El Centro-182	0.36	0.38	0.31
0.5 LGPC	0.26	0.22	0.36
EZ Turkey	0.18	0.19	0.22
Northridge	0.25	0.38	0.32
ChiChi	0.29	0.73	0.82
0.5 Bam	0.18	0.15	0.13
0.3 Christchurch	0.16	0.15	0.14

The maximum friction force calculated in this section is different from the values estimated in the static tests (0.47 N) and the time harmonic test (1.07 N). This friction force is lower than the other estimations. This is because the dynamic friction force was measured in this case which is normally less than friction force measured using static tests. The reason for the difference between this value and the friction force measure using transmissibility curve can be because of an inaccurate reading of the data from the graphs.

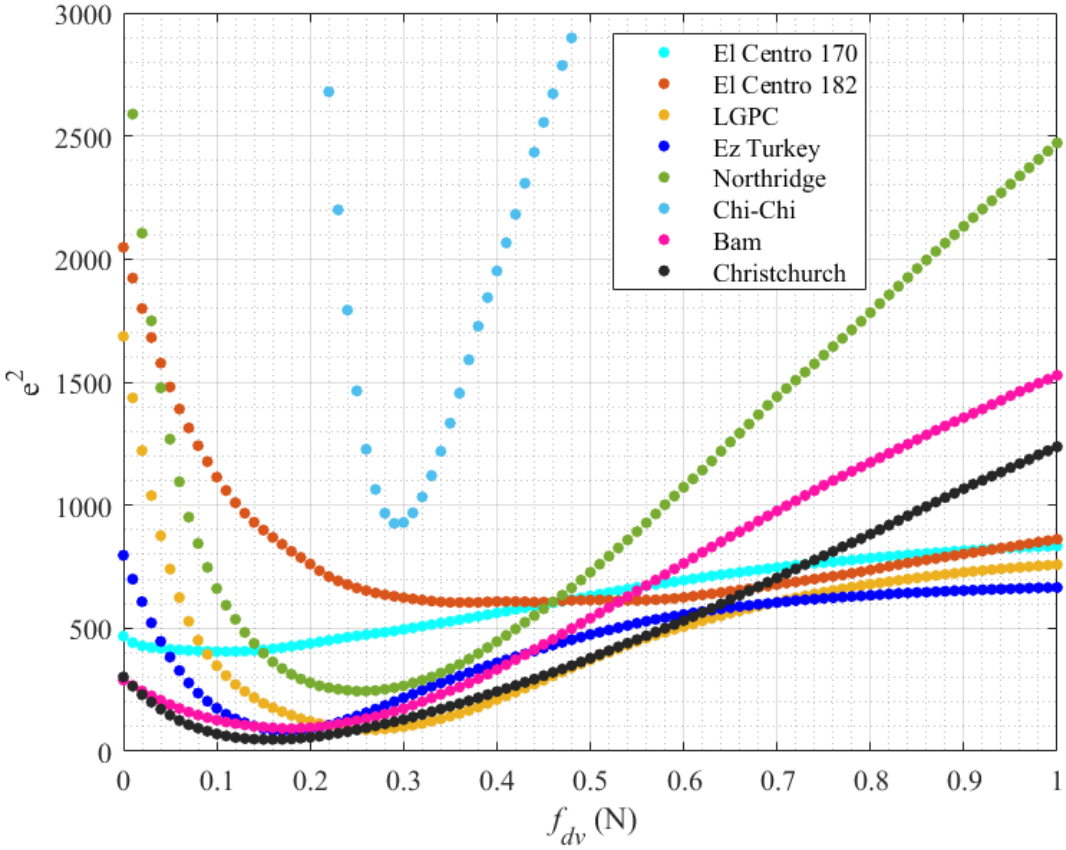

Figure 5.24. Squared error vs. friction force for set 2 of various earthquake inputs

5.5 Conclusions

In this chapter, the experimental results were presented and compared with the numerical results. The numerical model was developed based on parameters which were measured in the lab including the stiffness of the springs as well as the initial angle and the loading for two specimens with 0.05m and 0.1 m long arms. The maximum friction force was also calculated using three methods, based on static tests, time harmonic tests, and earthquake tests. In the static loading/unloading tests, the average friction force around the horizontal equilibrium position was calculated as 0.47 N. Using transmissibly of harmonic excitations, the friction force was calculated for various amplitudes of motion. This method gave different values for different amplitudes of excitation. The minimum and maximum friction force given by this method were around 0.5 N and 1.85 N, respectively. The numerical modelling with those friction forces did not show good agreement for the earthquake experimental results. Therefore, the least squared error method was used to calculate the friction force. In this method, the friction force was calculated for 8 different earthquake inputs and repeated three times. Then the mean of these values, 0.27 N, was taken as the maximum friction force for the numerical modelling. The friction force calculated from the last approach appeared to give a good agreement for both transmissibility and earthquake tests.

The experimental results show that the system reduces the maximum acceleration and RMS acceleration by at least 50 and 40 percent respectively for 7 out of 8 cases compared to the rigid base without isolator. For the Chichi earthquake, however, there is a magnification which increases the maximum and RMS acceleration ratio to 2.22 and 1.76. This is thought to be due to the frequency content of this earthquake which seems to have higher energy levels of excitation at frequencies in the vicinity of the resonance frequency of the isolator.

By comparing the acceleration spectrum of input and response, it has been shown that the mechanism can efficiently isolate frequencies higher than 3 Hz, which in this case is twice the resonance frequency.

The sensitivity of the system to mistuning and change in the payload was also considered. It was shown that mistuning due to shifting the vertical location of the arms by 10% of the length of the arms does not affect the performance of the system substantially. The change in the load around 5% also does not affect the response of the system noticeably.

The effect of the intensity of base excitation was also considered. It was shown that the system with or without mistuning has similar output/input ratios for maximum and RMS of acceleration for higher input amplitude around 0.87g (for Christchurch earthquake input). While for low input amplitude around 0.22g these ratios were higher for the systems with mistuning than the one without.

The comparison between the measured and predicted values of the acceleration of the mass shows that the mathematical model of the isolator is good. However, the model can be improved considering other sources of deviation including but not limited to, the inaccuracy in the friction force, the determination of damping and stiffness values and the distribution of inertia.

Chapter 6.

Conclusion

The general objectives of this research were to investigate the applicability of a quasi-zero-stiffness system (QZSS), which has zero stiffness at the static equilibrium position, as well as a high-static-low-dynamic-stiffness system (HSLDSS), which retains some stiffness at the static equilibrium position, for earthquake isolation of structures. The overall question was how to minimise transfer of damaging forces to the structure. Considering the variation in loads on civil engineering structures, and the uncertainties associated with construction, the performance of an isolator needs to be clearly understood when parameters associated with geometry and load change.

This led to the following research questions which have been addressed in this study:

- How to minimize vertical force transmission? How do the dynamic properties of the system components (stiffness, damping and friction) affect the force transmission?
- How does the mechanism behave subjected to vertical excitations considering uncertainties?
- How to optimize the design parameters of the isolator taking into account the answers to the first two questions?

To answer these questions, in chapter 2, the static equation for the proposed mechanism was developed and the design parameters were identified. These parameters are the length of the arms, the initial angle (unloaded position) of the arms with the horizontal axis and the stiffness of the horizontal and vertical springs. The equation was limited to the case where all springs were unstressed before applying the payload and the effect of prestress was omitted. The results showed that by increasing the initial angle of the arms, the geometric nonlinearity increases. This is also true for the horizontal/vertical spring stiffness ratio. By analysing the static behaviour of the system, a formula was obtained to calculate the stiffness of the horizontal and vertical springs as a function of the payload and their ratio for a QZSS, which has zero stiffness when the arms are horizontal at the static equilibrium position. The values for the length and initial angle of the arms were chosen to fulfil the requirement of having the resonance frequency below 1 Hz. The dynamic equation of motion for the mechanism was developed which included the damping ratio and the linear and nonlinear friction in the system.

The dynamic behaviour of the mechanism was seen to depend strongly on the amplitude of the excitation. The greater amplitude causes more nonlinear behaviour and an increase in the resonance value. In addition, the effects of the tolerance in the initial configuration of the system, and the uncertainty in the weight on the dynamic behaviour of a QZSS and a HSLDSS (with horizontal arms at the static equilibrium position) were investigated. The results for transmissibility (output/input acceleration ratio for sinusoidal inputs) showed that although the perfectly tuned QZSS had a low resonance frequency (which results in a high isolation performance), it is highly sensitive to any changes in the payload or initial configuration, and is susceptible to becoming unstable, and hence it may not be a practical solution. However, it has been shown that an HSLDSS system can be designed to significantly reduce force transmission. In addition to being less sensitive to changes, it does not become unstable, which appears to offer an advantage over the QZSS. In addition, dry friction in both vertical and

horizontal directions were modelled, and the results were compared. The effect of friction forces in both directions was found to decrease the transmissibility at resonance but increased it at high frequencies. Since the friction force was studied as a ratio of the payload, for a full-scale model with higher payload, it is expected that the friction force/payload ratio becomes small, and the friction may not affect the seismic isolation performance of the system significantly.

After studying the behaviour of the HSLDSS and the QZSS subjected to harmonic excitation, in chapter 3, the dynamic behaviour of these two mechanisms (QZSS and HSLDSS) was investigated subjected to vertical components of a selection of 23 near-fault earthquake ground motions. Seventeen earthquake signals had a high power in the frequency range above 1 Hz while six earthquake signals (from different stations for 3 earthquakes Northridge, Kobe and Chichi) had a higher power in the frequency range below 1 Hz. Based on the literature, the vertical component of earthquake excitations in near-fault areas is expected to have high power in high frequency range. However, there are a few cases where this does not happen. For analysing the seismic performance of the mechanism for these 23 cases, an equation was developed in order to keep the resonance frequency below 1 Hz. In this equation, the variables were defined based on the payload. The stiffnesses of the springs for any given payload were determined by using the criteria that at static equilibrium the arms will be horizontal, and the system will have zero stiffness. The results based on these 23 earthquake excitations suggested that for an ideal QZSS, the length of the arms should be equal to or greater than 0.6 m long in order to provide enough stroke for the amplitude of the earthquakes. The initial angle to the horizontal axis was also suggested to be 60° to get good reduction in the maximum and RMS acceleration for any given payload. The damping ratio of 10% was found to be suitable to improve the isolation performance for those six inputs with high energy in high frequency range (higher than 1 Hz). The linear and nonlinear friction effects (in the vertical and horizontal directions) on the seismic performance of the mechanism were also studied. The results showed that the friction forces (especially the nonlinear friction of 5% *mg* or more) decrease the performance of the isolator substantially and must be minimised to get the maximum seismic isolation. The results showed that the designed QZSS with 10% damping and without friction reduced the maximum and RMS acceleration by 27-93% for most cases. This mechanism also decreases the force transmitted to the mass significantly, which suggests that for 22 cases this force is less than 20% of the payload, while without an isolator, this force can be 3 times the payload. For the Chichi earthquake, also, the mechanism reduces the transmitted force by around 34% compared to the rigid base. By comparing the QZSS with a linear system with the same vertical spring stiffness and 10% damping, it was shown that the QZSS was more effective and reduces the maximum and RMS acceleration, the absolute displacement and the force transmission up to 50% more than the linear system. Besides, the QZSS with horizontal springs can be adjusted to provide the required stiffness, while this is not an option in a linear system. The analysis was based on the response of the system to 23 historical earthquakes and will apply to any other.

To address sensitivity of the QZSS, a control system could be used to tune the mechanism in case of any changes to the payload or the initial configuration. Alternatively, by decreasing the stiffness of the horizontal spring, the system will become a HSLDSS which still retains the seismic performance while it is less sensitive to those changes. The results showed that the HSLDSS with 0.8 horizontal spring stiffness of the designed QZSS gives a good acceleration reduction and can be an alternative for a QZSS.

In chapter 4, the rig and equipment used for the experiments were introduced and in chapter 5 the results (including static, sinusoidal harmonic and earthquake tests) for the HSLDSS rig were compared to numerical results. The results for these three types of tests showed good agreement between experiment and Theory. The system was able to reduce the maximum acceleration and RMS acceleration by at least 50 and 40 percent, respectively for 7 out of the 8 earthquake inputs. For the Chichi earthquake, however, there was a magnification which increased the maximum and RMS acceleration ratio to 2.22 and 1.76, respectively. This is thought to be due to the low frequency content of this earthquake which was mentioned previously. By comparing the acceleration spectrum of input and response, it was shown that the mechanism can efficiently isolate frequencies higher than 3 Hz, which in this case was around twice the resonance frequency. The sensitivity of the system to mistuning and change in the payload was also tested. It was shown that mistuning due to shifting the vertical location of the arms by 10% of the length of the arms does not affect the performance of the system substantially. In addition, the change in the load around 5% does not affect the response of the system noticeably either. In other sets of tests, the effect of intensity of input excitation was investigated, and it was found that the system with or without mistuning has similar output/input ratios for maximum and RMS of acceleration for a higher input amplitude around 0.87g (for Christchurch earthquake input), while for low input amplitude around 0.22g these ratios were higher for the systems with mistuning than without.

Overall, the developed mechanism is shown to be efficient in isolating structures with one support subjected to earthquake inputs. It reduces the force transmission from the base to structures during earthquakes.

Future work

Based on the results of this study, the proposed mechanism shows potential to be developed as an effective seismic isolator for structural purposes. In order to verify the potential practical implementation of the concept, further research need to be done including but not limited to the following suggestions:

In this study, the performance of a single support subjected to the vertical component of earthquakes was investigated. However, there are other aspects which require further investigation. For instance, in practice, a structure/building needs more than one support and isolator. Considering multiple supports for a building/structure, the interactions between these supports need further research especially when the horizontal, rocking and rotational ground motions are combined with the vertical ground motion. Applying those motions changes the distribution of the payload on each support. Since the stiffness of the isolator depends on the geometry and changes for different values of payload, the response of each support to the vertical excitation can be different for each support. In addition, for long structures such as bridges, the vertical ground excitation can also vary for different supports which needs further investigation.

Moreover, the dry friction model for this mechanism can be developed to include other effects such as the angle of the arms with horizontal axis, frequency of input signals and other unknown factors.

Combining this mechanism with another control system can increase the performance for the system subjected to earthquakes. As mentioned earlier, the QZSS has the highest performance among other choice of HSLDSS. A weakness is the sensitivity to changes in payload or initial configuration. Another problem can arise if the relative displacement of the system is higher

than the length of the arms, therefore, the stiffness of mechanism becomes infinity and system behaves like a system with rigid support. By having another control system, the stiffness of the springs and the angle of the arms can be tuned in the real time basis to retain the system in QZS status. This control system should monitor the payload and send feedback to adjust the stiffness of the springs.

A lock and release system could also be investigated in order to decrease unwanted displacement of the structures under daily changes in payload. Since the mechanism has ideally low stiffness at the static equilibrium position, a small change in payload might cause noticeable static or dynamic displacements which may make residents feel unsafe. Therefore, the mechanism could be locked under normal operating conditions and automatically released when an earthquake strikes.

Further experimental work to verify the potential use of this concept for practical implementation will need to address the above.

Appendix A

Rig detailed design

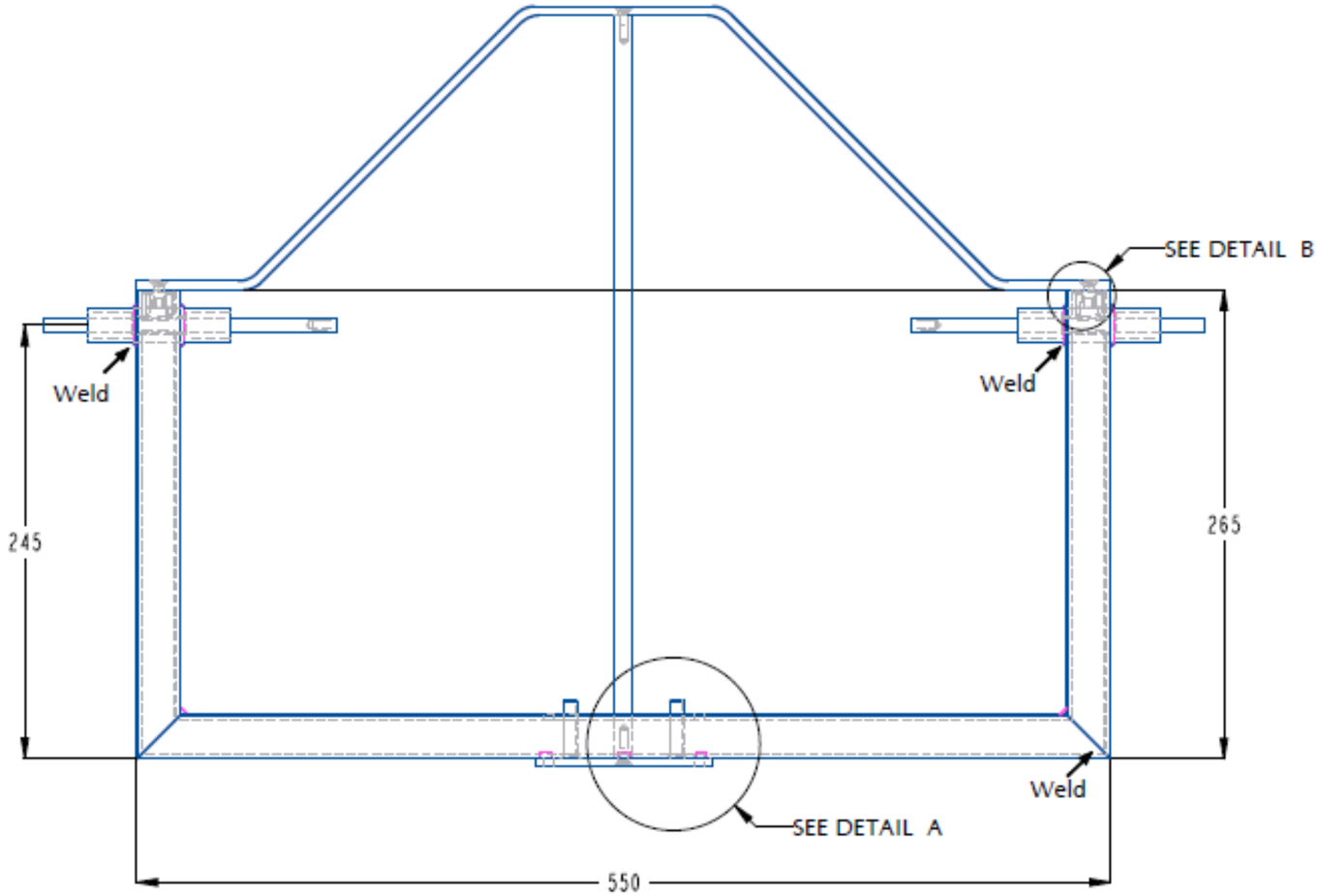

SCALE 0.300

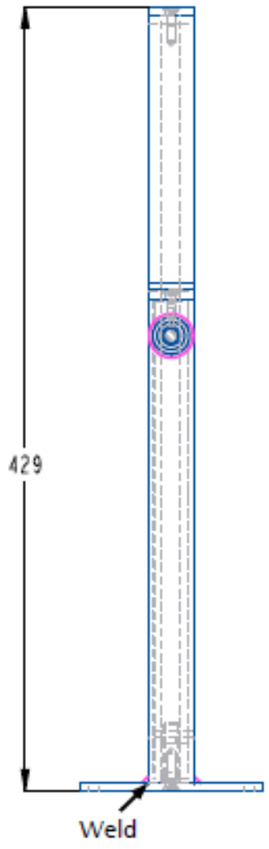

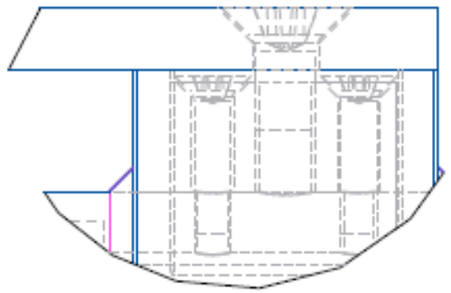

DETAIL B
SCALE 2.000

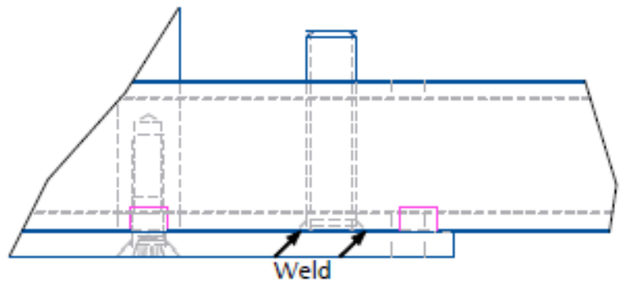

DETAIL A
SCALE 1.000

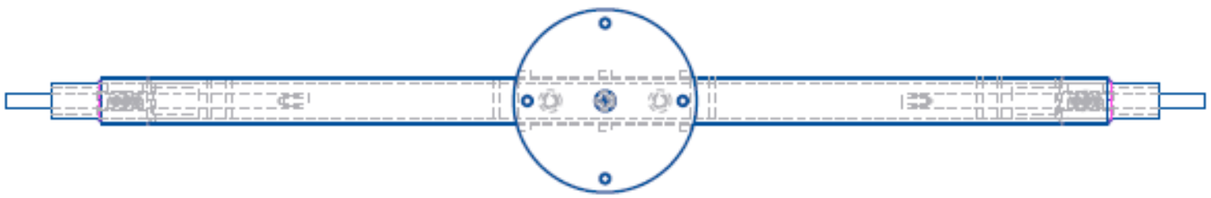

Part No.	Name of Part	Qty.	Material
LM8UU	Minature Bearing 8x15x24	04	
LM10UU	Minature Bearing 10x19x29	02	
	M3x.5-13mm-Countersunk Screw	04	
	M5x.8-10mm-Countersunk Screw	04	
	M8X33 - Threaded rod	02	

Change No.	Name of Item	Changes Made	OK	DATE

ALL TOLERANCES ARE ±0.1mm UNLESS OTHERWISE SPECIFIED | ALL DIMENSIONS IN MILLIMETRES

THE UNIVERSITY OF AUCKLAND
NEW ZEALAND

DRAWN BY: Sarath Pathirana
DATE: 09th October 2020
FILENAME: ProposedModified_Rig
TUTOR:
GROUP No.:

TITLE: **Modified Earthquake Isolation Rig Assembly**
DEPARTMENT: **Mechanical Engineering**
FILE LOCATION: E:\PRO_E\Elena_Project
QUANTITY: 01
SCALE: 0.3
SHEET:
A3

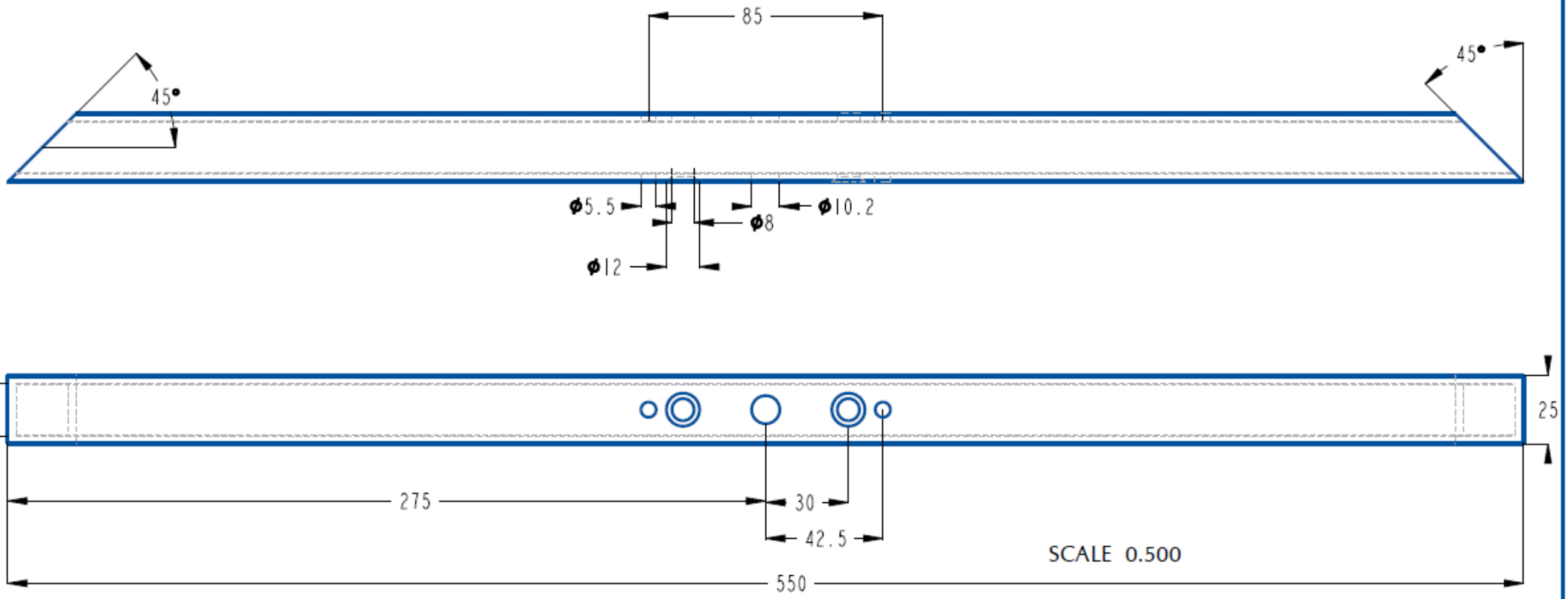

SCALE 0.100

Change No.	Name of Item	Changes Made	OK	Date

THE UNIVERSITY OF AUCKLAND
NEW ZEALAND

DRAWN BY	Sarath Pathirana
TUTOR	
GROUP No.	
FILENAME	BaseSHS_M_Frame
DATE	7th October 2020

TITLE **Base SHS Main Frame - EqIP**

DEPARTMENT **Mechanical Engineering**

FILE LOCATION E:\PRO_E\Elena_Project

MATERIAL SS | Qty. 01 | SCALE 0.5 | SHEET | A4

ALL TOLERANCES ARE ±0.1mm UNLESS OTHERWISE SPECIFIED

ALL DIMENSIONS IN MILLIMETRES

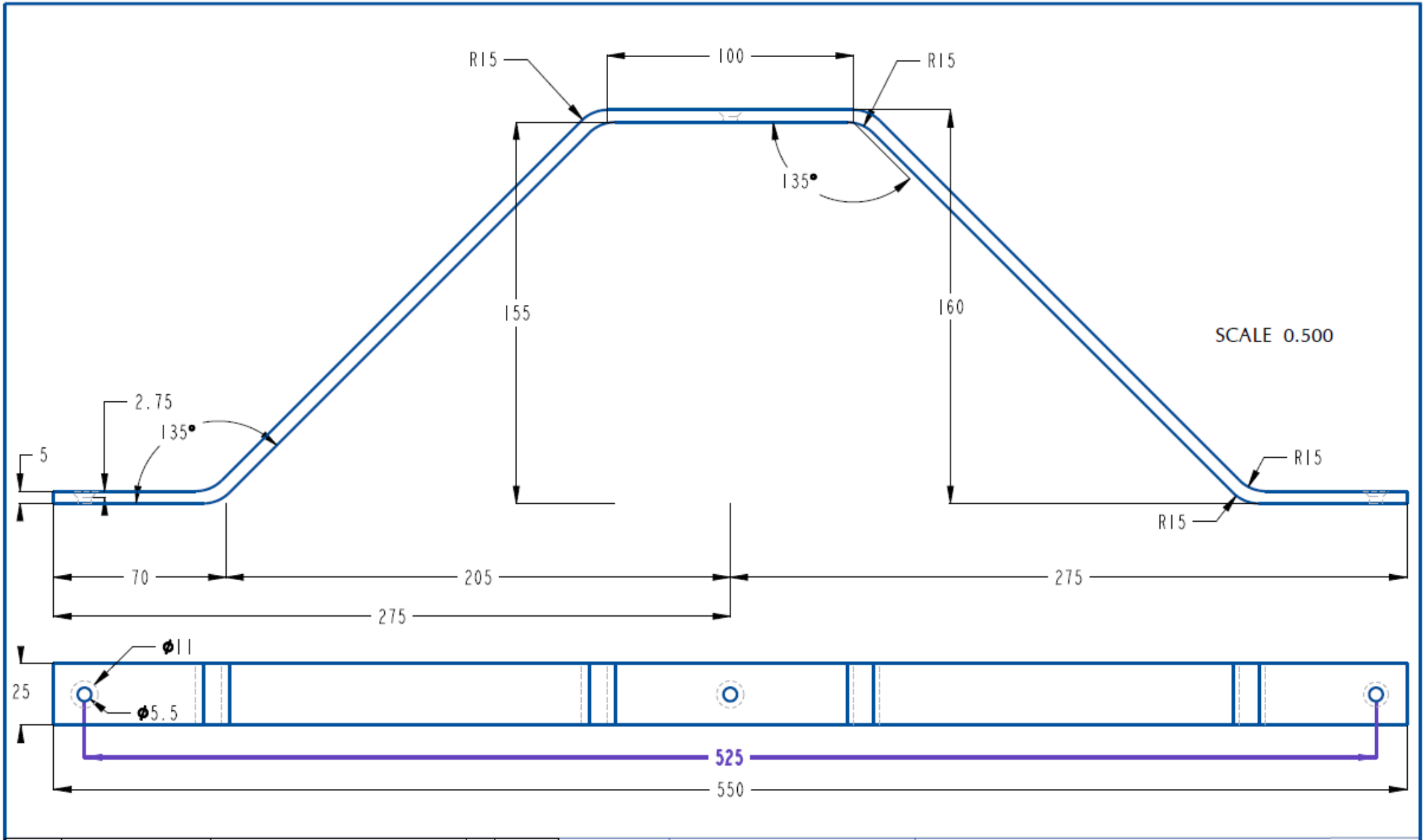

Change No.	Name of Item	Changes Made	OK	Date

THE UNIVERSITY OF AUCKLAND

DRAWN BY	Sarath Pathirana
TUTOR	
GROUP No.	
FILENAME	25_5_Flatbar
DATE	07th October2020
TITLE	25x5_Flatbar_EqIP
DEPARTMENT	Mechanical Engineering
FILE LOCATION	E:\PRO_E\Elena_Project
MATERIAL	SS
Qty.	01
SCALE	0.5
SHEET	A4

ALL TOLERANCES ARE ±0.1mm UNLESS OTHERWISE SPECIFIED

ALL DIMENSIONS IN MILLIMETRES

Material: SHS 25x25x3

SCALE 0.250

Change No.	Name of Item	Changes Made	OK	Date

THE UNIVERSITY OF AUCKLAND NEW ZEALAND

DRAWN BY Sarath Pathirana	TITLE **Side Members Mainframe - EqIP**		
TUTOR	DEPARTMENT **Mechanical Engineering**		
GROUP No.			
FILENAME SideM_MFrame	FILE LOCATION E:\PRO_E\Elena_Project		
DATE 07th October 2020	MATERIAL SS	Qty. 02	SCALE 1.0

ALL TOLERANCES ARE ±0.1mm UNLESS OTHERWISE SPECIFIED

ALL DIMENSIONS IN MILLIMETRES

SHEET A4

V

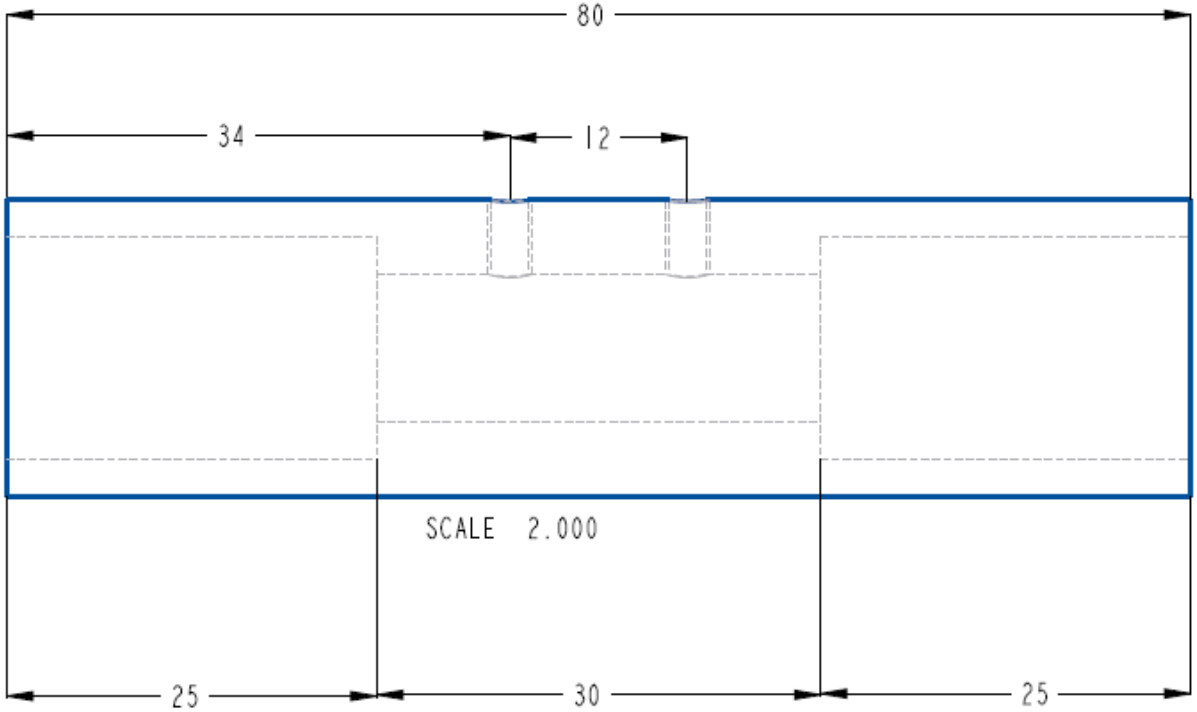

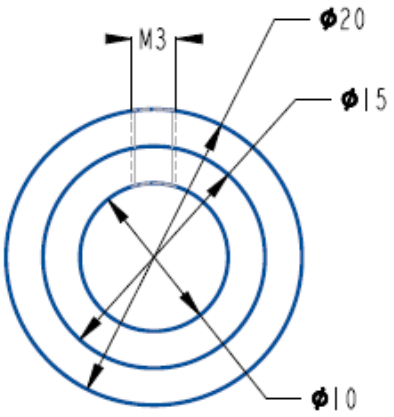

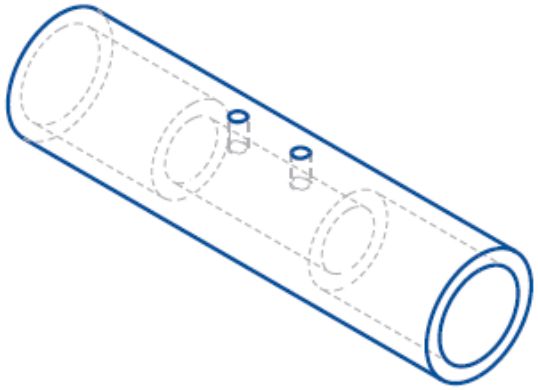

Change No.	Name of Item	Changes Made	OK	Date

ALL TOLERANCES ARE ±0.1mm UNLESS OTHERWISE SPECIFIED

ALL DIMENSIONS IN MILLIMETRES

THE UNIVERSITY OF AUCKLAND
NEW ZEALAND

DRAWN BY Sarath Pathirana

TUTOR

GROUP No.

FILENAME BearingHousing_8mm

DATE 7th October 2020

TITLE **Bearing Housing 8mm -EqIP**

DEPARTMENT **Mechanical Engineering**

FILE LOCATION E:\PRO_E\Elena_Project

MATERIAL SS

Qty. 02

SCALE 2.0

SHEET

A4

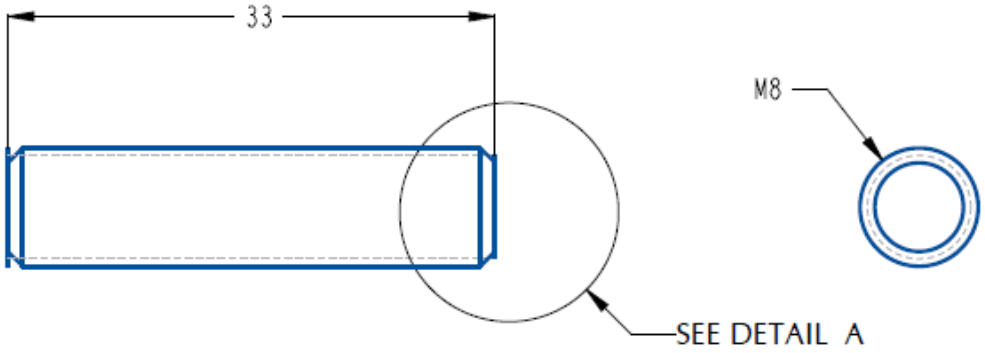

SCALE 2.000

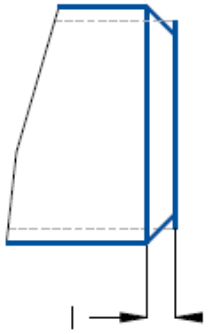

DETAIL A
SCALE 4.000

Change No.	Name of Item	Changes Made	OK	Date

THE UNIVERSITY OF AUCKLAND

DRAWN BY	Sarath Pathirana
TUTOR	
GROUP No.	
FILENAME	ThreadedRod_8MM
DATE	12th October 2020
TITLE	Threaded Rod - EqIP
DEPARTMENT	Mechanical Engineering
FILE LOCATION	E:\PRO_E\Elena_Project
MATERIAL	SS
Qty.	02
SCALE	2.0
SHEET	A4

ALL TOLERANCES ARE ±0.1mm UNLESS OTHERWISE SPECIFIED

ALL DIMENSIONS IN MILLIMETRES

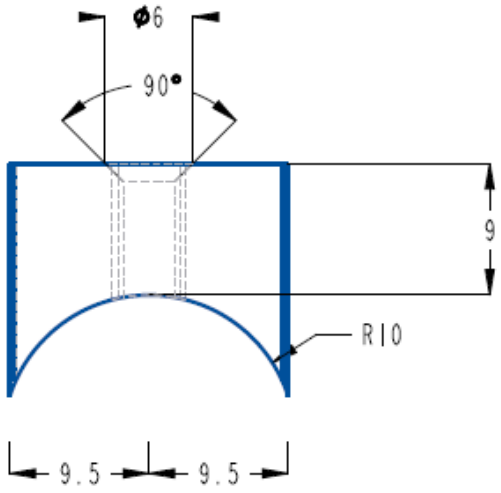

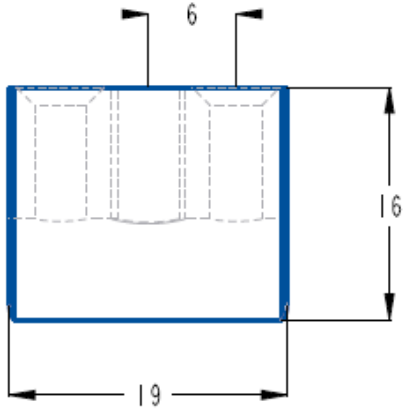

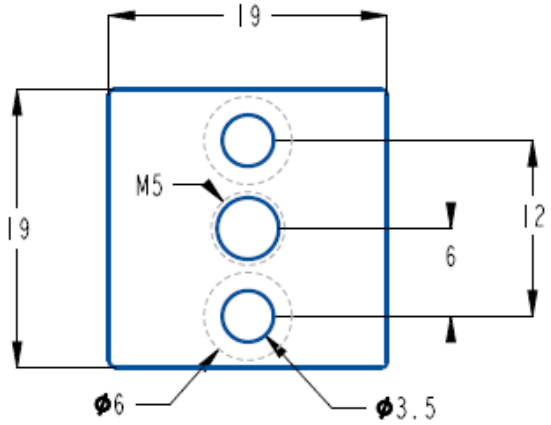

SCALE 2.000

Material: Aluminium

Change No.	Name of Item	Changes Made	OK	Date

ALL TOLERANCES ARE ±0.1mm UNLESS OTHERWISE SPECIFIED

ALL DIMENSIONS IN MILLIMETRES

THE UNIVERSITY OF AUCKLAND NEW ZEALAND

DRAWN BY Sarath Pathirana

TUTOR

GROUP No.

FILENAME ThreadInsert New

DATE 09th October 2020

TITLE **Thread Insert side Column - EqIP**

DEPARTMENT **Mechanical Engineering**

FILE LOCATION

MATERIAL Aluminium | Qty. 02 | SCALE 2.0 | SHEET | A4

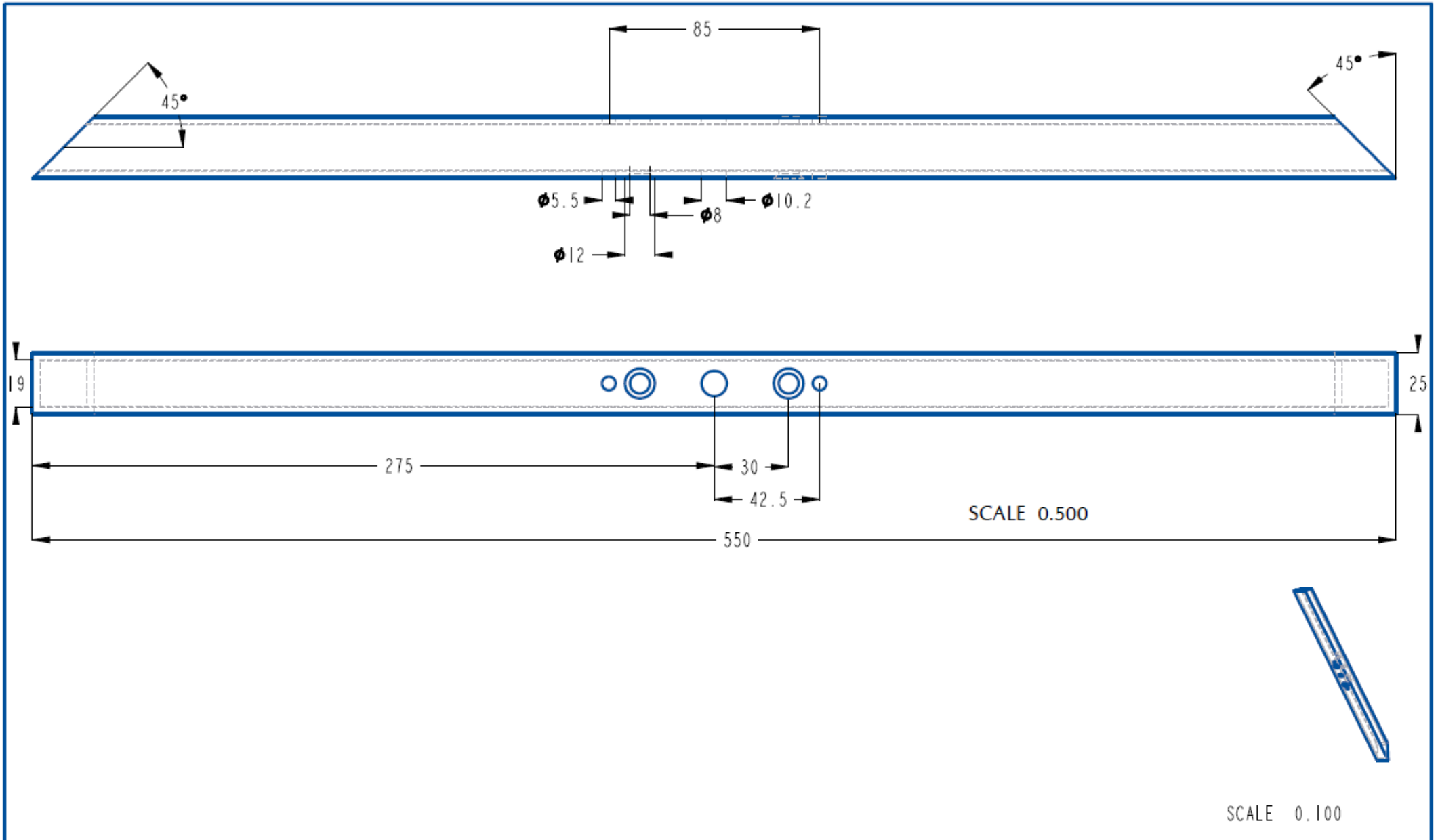

Change No.	Name of Item	Changes Made	OK	Date

ALL TOLERANCES ARE ±0.1mm UNLESS OTHERWISE SPECIFIED

ALL DIMENSIONS IN MILLIMETRES

THE UNIVERSITY OF AUCKLAND NEW ZEALAND

DRAWN BY	Sarath Pathirana
TUTOR	
GROUP No.	
FILENAME	BaseSHS_M_Frame
DATE	7th October 2020
TITLE	**Base SHS Main Frame - EqIP**
DEPARTMENT	**Mechanical Engineering**
FILE LOCATION	E:\PRO E\Elena Project
MATERIAL	SS
Qty.	01
SCALE	0.5
SHEET	A4

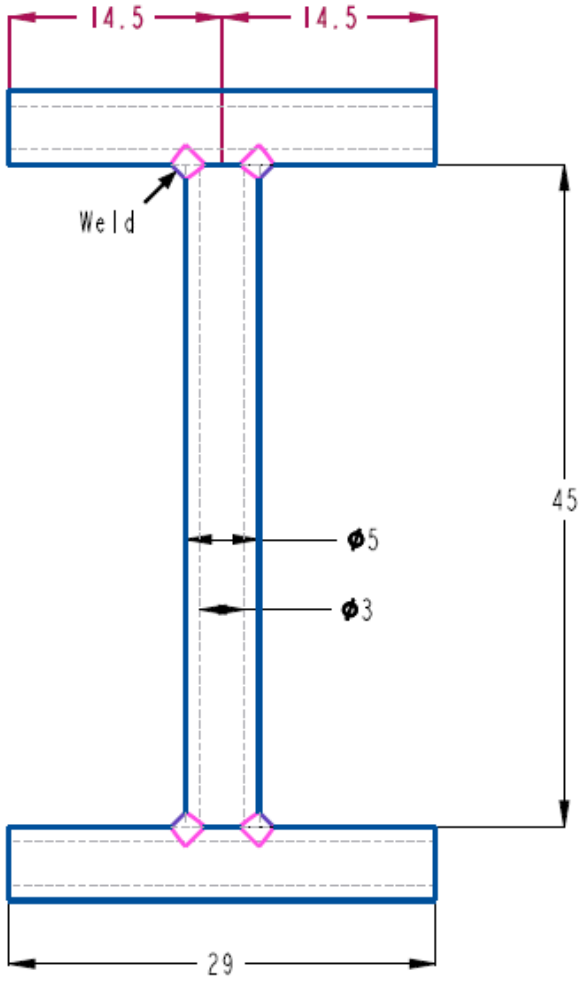

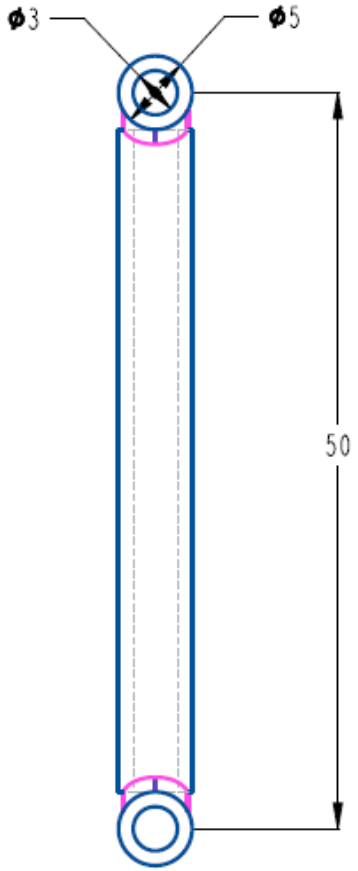

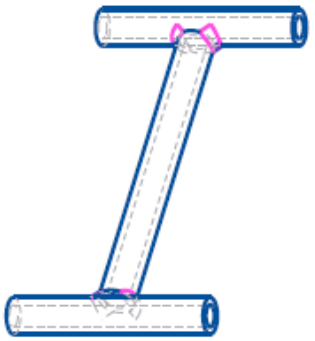

SCALE 2.000

Material: Brass 5mm ø Hollow shaft

Part No.	Name of Part	Qty.	Material

Change No.	Name of Item	Changes Made	OK	Date

THE UNIVERSITY OF AUCKLAND

DRAWN BY Sarath Pathirana

TUTOR

GROUP No.

FILENAME

TITLE **Modified Arm Assy 5 CM**

DEPARTMENT **Mechanical Engineering**

FILE LOCATION E:\PRO_E\Elena_Project

DATE 16 April 2021

QUANTITY 2

SCALE 2.0

SHEET A4

ALL TOLERANCES ARE ±0.1mm UNLESS OTHERWISE SPECIFIED

ALL DIMENSIONS IN MILLIMETRES

X

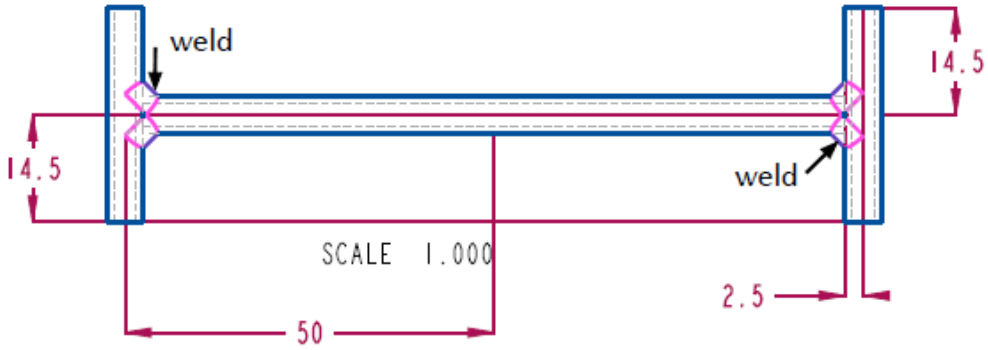

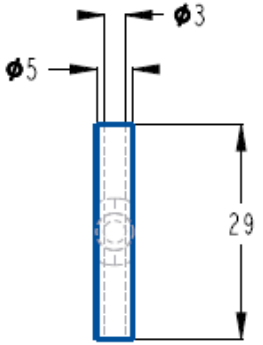

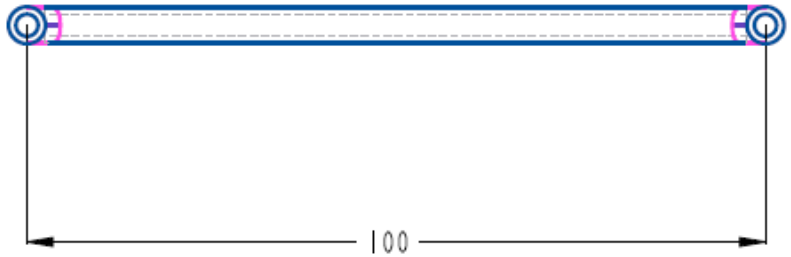

SCALE 0.500

Part No.	Name of Part	Qty.	Material
29mm	10CM_ARM_PINHEAD	04	Brass Tube OD-5ø,ID-3ø
95mm	10CM_ARM_SHARFT	02	Brass Tube OD-5ø,ID-3ø

Change No.	Name of Item	Changes Made	OK	Date

THE UNIVERSITY OF AUCKLAND NEW ZEALAND

DRAWN BY Sarath Pathirana

TUTOR

GROUP No.

FILENAME ARM_ASSEMBLY_10CM

DATE 24 November 2020

TITLE **ARM Assembly 10 CM**

DEPARTMENT **Mechanical Engineering**

FILE LOCATION E:\PRO_E\Elena_Project

QUANTITY 02 | SCALE 1.0 | SHEET A4

ALL TOLERANCES ARE ±0.1mm UNLESS OTHERWISE SPECIFIED | ALL DIMENSIONS IN MILLIMETRES

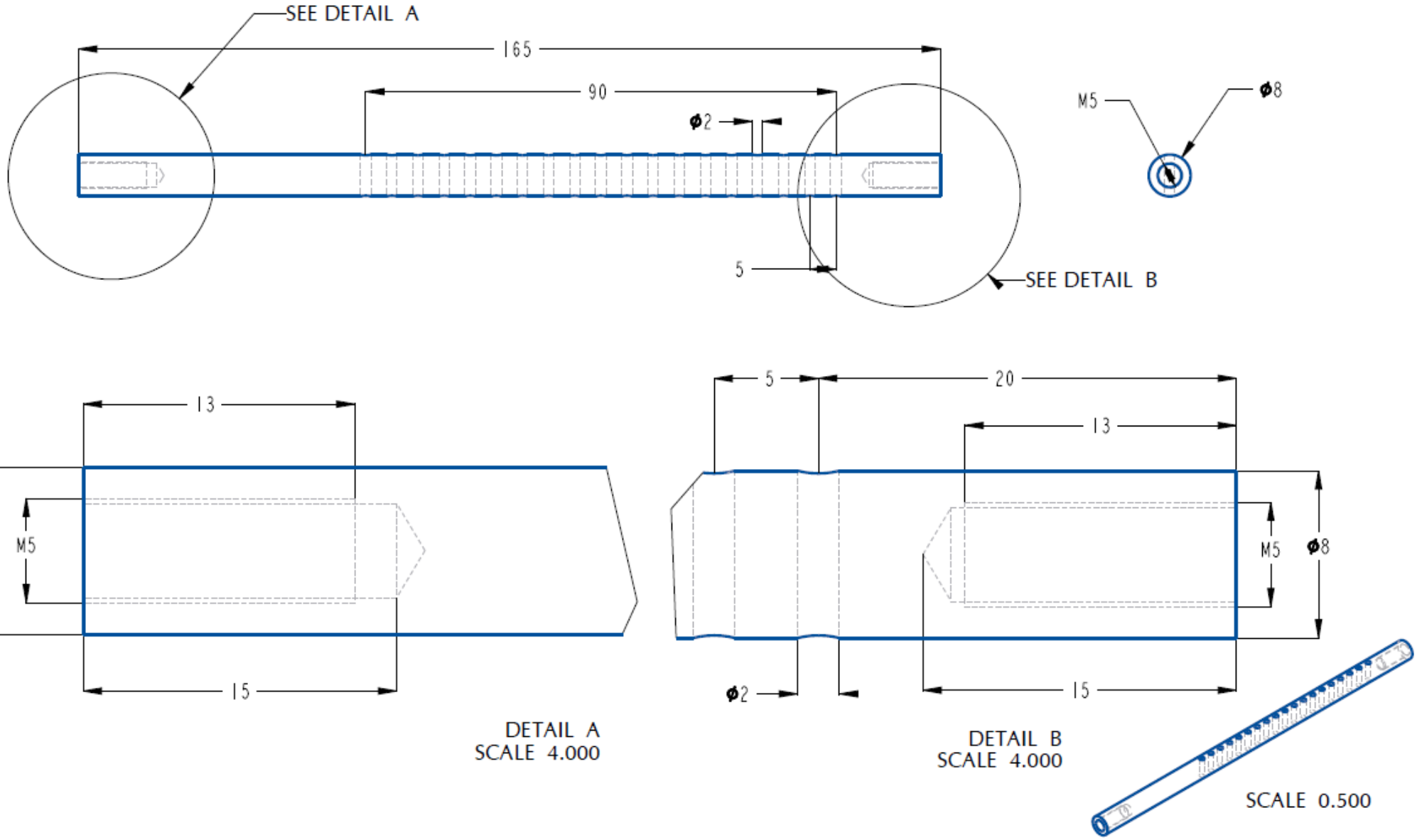

Change No.	Name of Item	Changes Made	OK	Date

THE UNIVERSITY OF AUCKLAND NEW ZEALAND

DRAWN BY	Sarath Pathirana
TUTOR	
GROUP No.	
FILENAME	Shafts_Horizontal
DATE	25th November 2020
TITLE	Modified Auxillary Shafts - EqIP
DEPARTMENT	Mechanical Engineering
FILE LOCATION	E:\PRO_E\Elena_Project
MATERIAL	Silver S
Qty.	02
SCALE	1.0
SHEET	A4

ALL TOLERANCES ARE ±0.1mm UNLESS OTHERWISE SPECIFIED

ALL DIMENSIONS IN MILLIMETRES

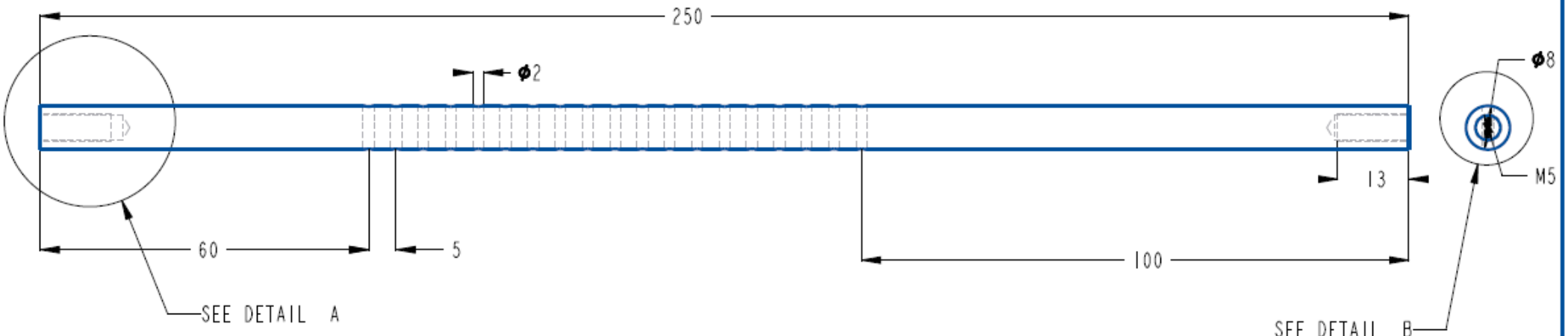

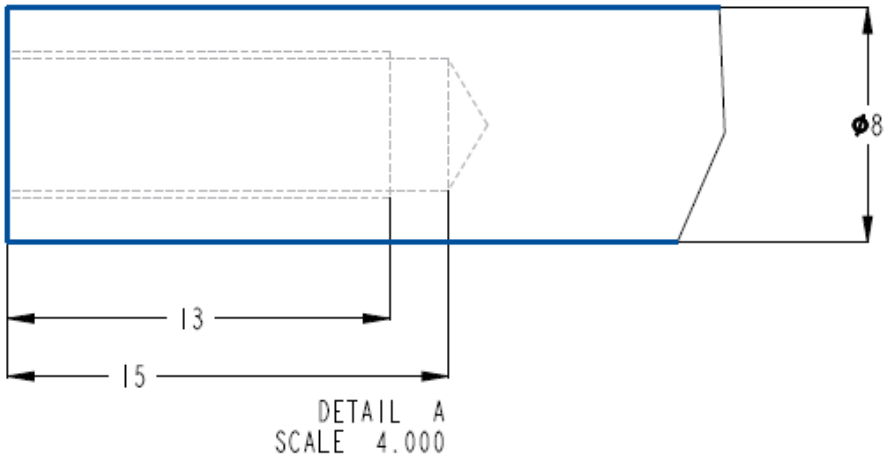

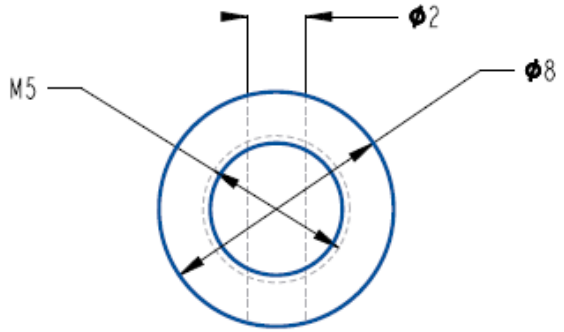

Change No.	Name of Item	Changes Made	OK	Date

THE UNIVERSITY OF AUCKLAND NEW ZEALAND

DRAWN BY Sarath Pathirana

TUTOR

GROUP No.

FILENAME Shafts_Horizontal

DATE 28 April 2021

TITLE **Modified Auxillary Shafts - EqIP**

DEPARTMENT **Mechanical Engineering**

FILE LOCATION E:\PRO_E\Elena_Project

MATERIAL Silver S | Qty. 02 | SCALE 1.0 | SHEET | A4

ALL TOLERANCES ARE ±0.1mm UNLESS OTHERWISE SPECIFIED

ALL DIMENSIONS IN MILLIMETRES

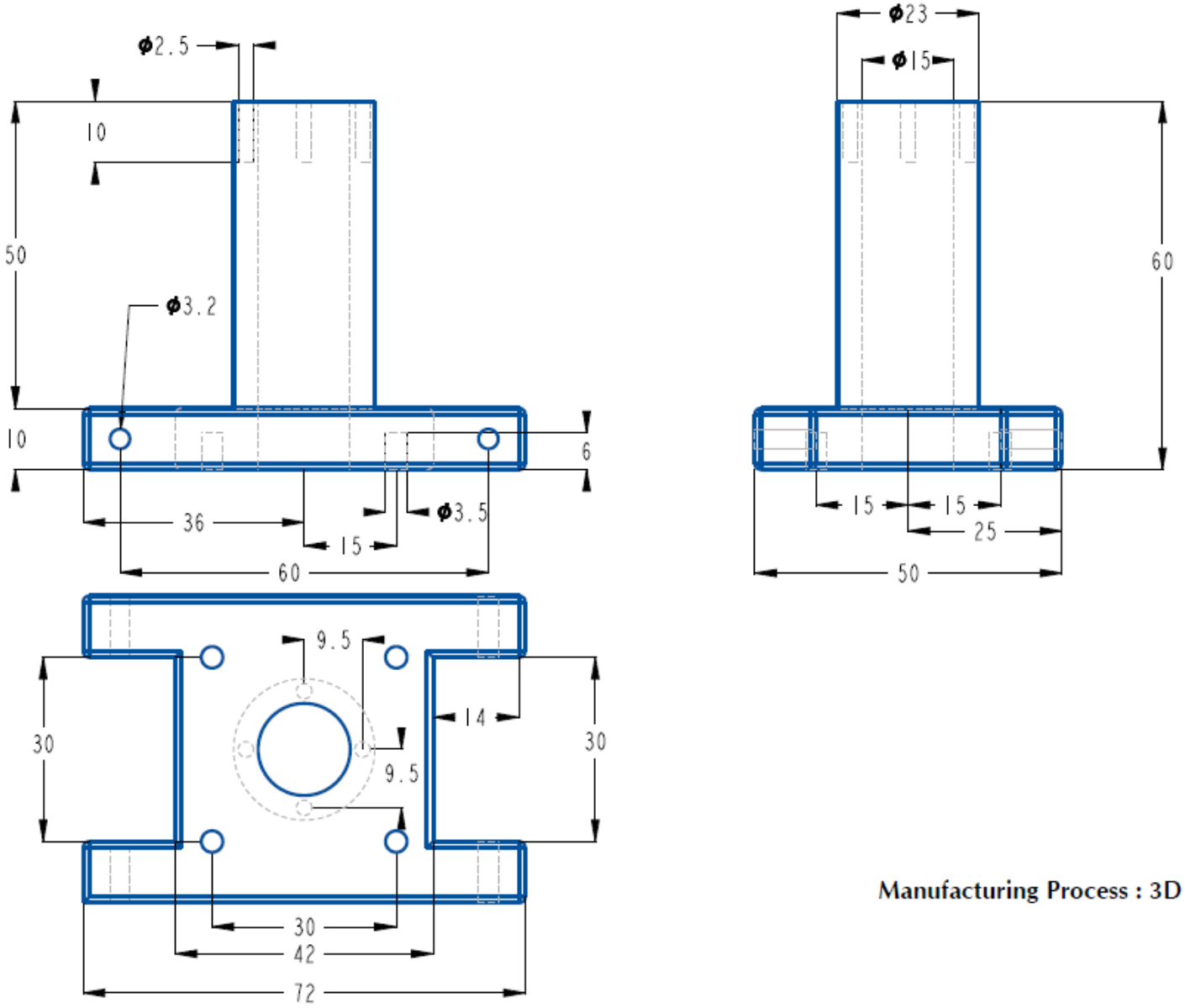

Manufacturing Process : 3D Print

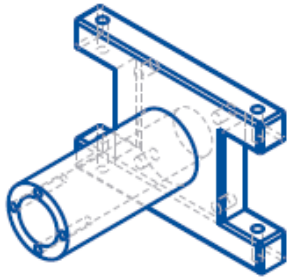

SCALE 0.500

Change No.	Name of Item	Changes Made	OK	Date

THE UNIVERSITY OF AUCKLAND

DRAWN BY	Sarath Pathirana
TUTOR	
GROUP No.	
FILENAME	Flatform_Bearing_Support
DATE	08th October 2020
TITLE	**Bearing Support Main Shaft - EqIP**
DEPARTMENT	**Mechanical Engineering**
FILE LOCATION	E:\PRO_E\Elena_Project
MATERIAL	PLA
Qty.	01
SCALE	1.0
SHEET	A4

ALL TOLERANCES ARE ±0.1mm UNLESS OTHERWISE SPECIFIED

ALL DIMENSIONS IN MILLIMETRES

Appendix B

Shaker and sensors

Shaker

APS 113 Electro-series shaker is used to excite the rig. This shaker with a large stroke is suitable for the large displacement excitation and is able to model most of earthquake signals without any filtrations required. The general specification of this shaker can be found in Table B.1. Based on the information on the catalogue, the armature weight including vertical table is 5.8 kg and the weight of the rig is around 2kg. Therefore, the limitation can be seen in Figure for different frequencies. Figure shows the acceleration, velocity and displacement capacities of the shaker for various payloads in different frequencies.

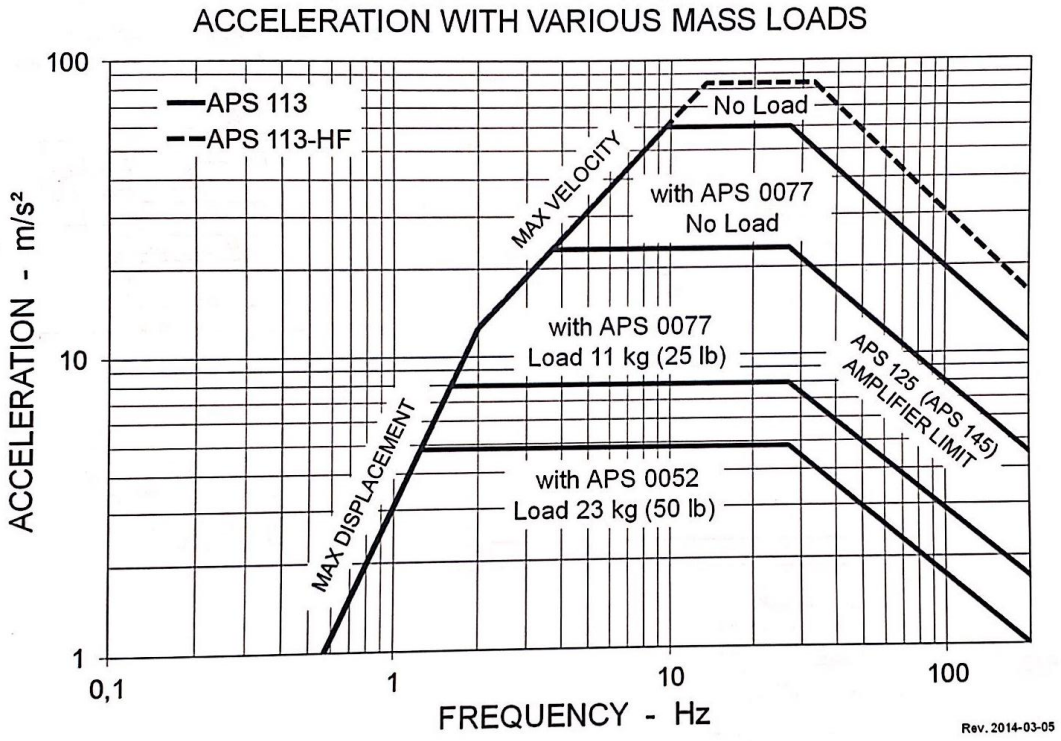

Figure B.1. Acceleration-frequency graph for the shaker

Table B.1. General specification of the shaker APS 113

Specifications

Shaker	**APS 113**	**APS 113-HF High Force**
Force (Sine Peak)	133 N (30 lbf)	186 N (42 lbf)
Velocity (Sine Peak)	1,000 mm/s (39 inch/s)	
Stroke (Peak - Peak)	158 mm (6.25 inch)	
Frequency Range	DC ... 200 Hz	
Operation	horizontal or vertical	
Armature Weight	2.3 kg (5.1 lb)	
Max. Overhung Load at Armature Attachment Point	9.0 kg (20 lb)	
DC Coil Resistance	4.4 or 1.1 Ω	1.4 Ω
Total Shaker Weight	36.0 kg (80 lb)	
Shipping Weight	41.0 kg (90 lb)	
Overall Dimension L x W x H	526 x 213 x 168 mm (20.7 x 8.4 x 6.6 inch)	
Operating Temperature	5 ... 40 degrees C	
Storage Temperature	-25 ... 55 degrees C	

Controller

The “Vibration Research” controller is employed to create the sine sweep signals as well as earthquake excitations and control the vibration (Figure B).

Figure B.2. Controller: VR9500

Sensors

The results were measured by accelerometers with around 200 mv/g sensitivity DYTRAN – 7500 A3 (Figure B. and Table B.2). As the accelerometers were being used for the measurements, the input and output signals were based on acceleration. For the earthquake excitation, also, the acceleration inputs were used. In other words, using displacement inputs will not give enough accuracy and in some cases the demand and control signals do not converge.

Figure B.3. Sensor: DYTRAN – 7500 AX

Table B.2. General specification of accelerometer 7500 AX

This family also includes:					
Model	Input Range (g)	Frequency Response, ±3dB (Hz)	Sensitivity Differential, ±10% (mV/g)	Max.Shock (gpk)	Noise Differential (µg rms/√Hz)
7500A2	± 5	0-500	400	2000	12
7500A3	± 10	0-1000	200	5000	18
7500A4	± 25	0-1400	80	5000	25
7500A5	± 50	0-2000	40	5000	50
7500A6	± 100	0-2500	20	5000	100
7500A7	± 200	0-3000	10	5000	200
7500A8	± 400	0-4000	5	5000	400